UNIVERSITÀ DEGLI STUDI DI PADOVA

Dipartimento di Scienze Chimiche - DISC

Dipartimento di Fisica e Astronomia "G. Galilei" - DFA

Corso di dottorato in Scienza e Ingegneria dei Materiali e delle Nanostrutture
XXXI CICLO

TESI DI DOTTORATO

Control and manipulation of ferrofluid drops on functionalized surfaces

Coordinatore: Ch.mo Prof. Giovanni Mattei
Supervisore: Ch.mo Prof. Giampaolo Mistura

Dottorando: Carlo Rigoni

A tutti coloro con cui ho fatto nascere un'idea.

...e volta nostra poppa nel mattino, dei remi facemmo ali al folle volo...

Dante Alighieri - *La Divina Commedia - Inferno - Canto XXVI*

Guernica - Pablo Picasso

Abstract

Controlling and predicting the mobility of drops in contact with a solid surface is attracting a lot of attention thanks to its fundamental implications and technological applications. The interaction between ferrouids and magnetic fields allow to obtain controlled deformation of the ferrouid-air interface and control of motion. In this thesis we will show how ferrouid droplets represent an ideal playground for fundamental studies on drop dynamics and provide useful strategies for passive and active control of drop motion. In particular, after a brief introduction about microuidics and ferrouids, we will report results about the possibility to control the shape of droplets thanks to the interaction with magnetic fields of different strenght and gradient produced by permanent magnets. After that we will show how magnetic fields can be used to passively control the motion of ferrouid drops sliding down inclined planes and, in the end, we will describe how it is possible to obtain the division of a single drop in two daughter droplets taking advantage of a strong interaction with the magnetic field.

Contents

List of Figures

Introduction

Droplets are confined, small volumes of liquid surrounded by an immiscible fluid [1]. Controlling and predicting the motion of drops in contact with a solid surface is a major scientific challenge [2] that is relevant to fundamental research [3] and crucial for an ample variety of applications including microfluidics [4], self-cleaning coatings [5], fog collection [6] and dropwise condensation [7]. Many of these applications are inspired by solutions already present in nature as shown in figure 1.

The mobility of drops is deeply affected by substrate inhomogeneities [1]. For instance, water drops can roll very easily, keeping a nearly perfect spherical shape on a surface that remains essentially dry, on various natural materials that include many plant leaves (see figure 1 center), bird feathers and fish skins [9], and artificial biomimetic surfaces [10]. Strong water repellence occurs because the roughness increases the liquid-solid free energy [11]. A different approach to achieve non-wetting properties involves liquid functionalized surfaces [12–14]. These novel functional surfaces, are textured materials usually imbibed by a lyophilic oil. The premise for such a design is that a liquid surface is intrinsically smooth and defect-free down to the molecular scale.

Different methods have been explored to achieve the passive motion control of droplets, from tailoring surfaces with chemical patterns or gradients [15–18] to altering the surface morphology [19, 20]. On the other hand, active control of drop motion can be achieved with different approaches [2]. Fluid manipulations at the microscale are powerfully enabled through the use of ultrasonic surface acoustic waves [21]. A more exotic drop actuation relies on the so-called Leidenfrost phenomenon, that is the levitation of drops on a cushion of vapor produced when they are brought in contact with a hot solid [22]. Oscillations of the substrate are also used as an active way to control drop motion of any liquid because they couple to the liquid inertia. If the plate vibrates parallel to gravity, the contact line oscillations are rectified by hysteresis, thus inducing a ratcheting motion to the water drop vertically downward [23]. Interestingly, Brunet et al [24] found that, on an inclined plane, drops subject to sufficiently strong vertical vibrations can

Figure 1 : (Left) Droplets attached to a leaf of *Stipagrostis sabulicola* as an example of drowise consensation [8]. (Center) A drop on a lotus leaf: the lotus take advantage of its surface structure to repel water and exploit drops for the cleaning of the surface. (Right) a *Stenocara gracilipes* beetle, Stenocara beeles can harvest water from the humidity in the air.

Figure 2 : (Left) Normal-field instability induced by a permanent magnet on a pool of ferrofluid. (Center) Self-assembly induced by a magnetic field taking advantage of the normal-field instability. The liquid has been deposited on a superhydrophobic surface [31]. (Right) a. Nanoparticles dispersed in the bulk of the ferrofluid in absence of the magnetic field. b. Chain-like aggregates in the bulk of the ferrofluid generated by the application of an external magnetic field [32].

climb against gravity. With a similar technique drops can be moved on a flat surface by simultaneous vertical and horizontal vibrations that are phase-shifted [25] and can be merged on an inclined plane [26]. Another example is the case of electrowetting: electric fields generated by arrays of electrodes integrated into the surface and covered with an insulating layer are widely used as a tool to control the shape, motion, and generation of conductive drops [27, 28]. A possible alternative to electrowetting [27] to achieve active control of the drop motion relies on the use ferrofluids in the presence of external magnetic fields [29, 30].

Ferrofluids are colloidal suspensions of nanometer-sized magnetic particles dispersed in a liquid matrix. These magnetic particles are so small that they behave exactly like

molecules of the liquid in which they are suspended. However, each particle acts like a small permanent magnet [33]. The consequence of this is that the magnetic field can exert strong forces on the fluid, radically changing its shape as the fluid moves to maximally fill its volume with a magnetic field [34,35]. The most impressive example of how strong these deformation can be is the so called normal-field instability [36], characterized by the formation of an ordered pattern of spikes at the air-ferrofluid interface as displayed in figure 2 (left). This normal field instability can also induce the formation of self-assembly of droplets [37] as shown in figure 2 (center). The application of magnetic fields also affects the viscosity of ferrofluids [38]. This is mainly due to the reversible creation of chain-like aggregates of nanoparticles in the bulk of the ferrofluid [32,38] (see figure 2 a and b). These effects are at the same time exotic and useful for a wide range of applications, from computer disk drives to rotary vacuum seals and speaker-damping technology [39].
In the last years, ferrofluid droplets are finding many application in microfluidics [40,41] where external magnetic fields are used to control drops [42–44], perform chemical ferrofluid synthesis [45], carry out continuous flow cell separation [46, 47] and study the drop breakup dynamics [48]. Another possibility is to exploit the magnetic fields to control the wetting properties of ferrofluid sessile drops and to drag them along a surface [30, 31, 49–52]. For instance, the shape and contact angles of ferrofluid drops can be continuously varied by moving a permanent magnet [52]. More recently, drops of a commercial ferrofluid placed below a magnet exhibits modifications of the shape on a time scale of several minutes due to the migration and accumulation of the magnetic nanoparticles at the top part of the drop that eventually leads to its detachment [53]. Ferrofluid drops have been dragged on a horizontal substrate using a permanent magnet moving at a constant velocity. If the magnetic force is large enough to overcome the friction and capillary forces, the drop can slide with the same linear velocity as the magnet up to a critical velocity, beyond which the drop is not able to follow the moving magnet [49]. The motion of ferrofluid drops on superhydrophobic surfaces in an external magnetic field has been studied, and the interaction force between the droplet and the surfaces is measured to be very low [54].

The aim of this thesis is to deepen the understanding of the control of the deformations and the motion of ferrofluid drops on open substrates caused by the presence of external magnetic fields. The thesis is divided in two parts: the former one introduces/reviews the main characteristics of microfluidics and ferrofluids. The latter one, deals with the description of the experimental methodologies adopted in this thesis and

the presentation of the main results.

Part I

Fundamentals on Microfluidics and Ferrofluids

Chapter 1

Drop dynamics

This chapter will present an overview of the physical properties of liquids at the microscale. Starting from the definition of surface tension and Laplace pressure in Section 1.1, the chapter will then focus on the characteristics of the emulsions and the conditions for the coalescence of droplets in Section 1.2. The wetting properties of droplets on horizontal substrates will be discussed in Section 1.3 and after that the sliding properties on open surfaces in Section 1.4.

§ 1.1. Surface Tension

The liquid surface can be seen as a membrane characterized by a surface tension that opposes distortion [1]. Understanding the physical origin of surface tension and how it influences the properties of liquids at the microscale is required to understand the whole variety of phenomena in microfluidics.

§ 1.1.1. Definition

A liquid is a condesed state in which there is a mutual attraction among the molecules stronger than the thermal agitation. We can define two different states for a molecule in a liquid: the bulk state and the interfacial state [1] (see fig. 1.1 left). The molecules in the bulk are surrounded by other molecules and so find themselves in a "happy state" because they can interact with a large number of other molecules. On the other hand, the molecules on the surface can interact with only half of the molecules "below" them so they are in an "unhappy state". An intuitive consequence of this is that in the case of a liquid-gas interface the liquid adjusts its shape to expose the smallest surface area. If we indicate as U the energy of the "happy state", then the energy of the "unhappy

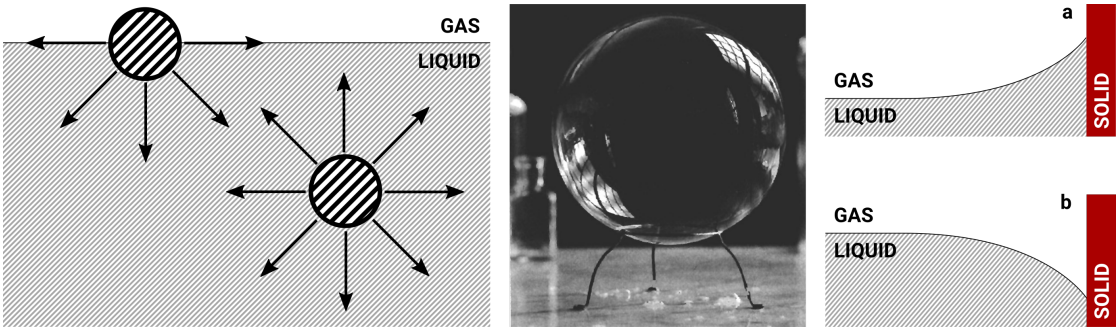

Figure 1.1 : From left to right: schematic representation of the interaction of two different water molecules of a liquid, one on the surface and one in the bulk, a soap bubble with a spherical shape [1], case of triple interaction between gas-liquid-solid: a) liquid-solid interaction stronger than liquid-liquid interaction; b) liquid-liquid interaction stronger than liquid-solid interaction.

state" can be indicated as U/2 and an energy of the order U/2 must be supplied to the molecule in the bulk to move to the interface. The surface tension $\gamma = U/2 \cdot a^2$ is a measure of this shortfall of energy.

This first simple example of a liquid phase interacting with a gaseous phase can be generalized for the case of the liquid interacting with both a gas and a solid. In this case, the interaction of the liquid molecules with the solid molecules is of different strength with respect to the interaction between two liquid molecules. We can define two different cases estimating the interaction between the molecules: the solid-liquid interaction can be higher or greater than the liquid-liquid interaction. When the interaction energy between the liquid and the solid is stronger (see fig. 1.1 a) the liquid will prefer the contact with the solid. This can have different consequences: for example, the liquid can "climb" a vertical section of the solid against the gravitational force. In the opposite case, the liquid tries to minimize the surface in contact with the solid and it will recede when in contact with it (see fig. 1.1 b).

Until now, we have given a generic definition of the surface tension, now we will provide a more accurate quantification of the phenomena [1]. Suppose we want to distort a liquid surface trying to increase the surface area of a quantity dA. The work we need to apply is proportional to the number of molecules we need to pull to the surface from the bulk and so to the increase of surface area dA. Of course, there is a coefficient in front of the surface area increase linked to the interaction energy between the liquid molecules: the stronger the interaction, the more work to increase the surface area. We call this coefficient surface tension of the liquid and we indicate it with the greek letter γ. The

equation for the work in this case is:

$$\delta W = \gamma \cdot dA \tag{1.1}$$

In other words we can define the surface tension as [1] :

"γ is the energy that must be supplied to increase the surface area by one unit"

§ 1.1.2. Laplace pressure

Surface tension regulates countless physical phenomena, like the overpressure existing in the interior of drops and bubbles [1]. This pressure difference has several consequences: the capillary adhesion between two plates, the presence of capillary bridges etc. To understand how this overpressure is generated we will study the case of a sphere of liquid and then this case will be generalized.
To study the case of a spherical droplet, we consider an oil droplet in water (see fig. 1.2 left). As we said before, to reduce the surface energy the drop adopts a spherical shape with radius R. Let us consider a displacement dR of the oil/water interface, in this case we can write the work of the pressure and capillary force as:

$$\delta W = -p_o dV_o - p_w dV_w + \gamma_{ow} dA \tag{1.2}$$

with $dV_o = 4\pi R^2 dR = -dV_w$, and $dA = 8\pi R dR$ are the increase in volume and surface, p_o and p_w are the pressure in oil and water and γ_{ow} is the surface tension between the oil and the water. At equilibrium, there will be no displacement in the surface of the droplets so $\delta W = 0$. In this case we can write:

$$\Delta p = p_o - p_w = \frac{2\gamma_{ow}}{R} \tag{1.3}$$

The smaller the drop, the higher the pressure difference from the outside fluid. A first consequence of this formula is that in emulsions of oil in water, small drops disappear in favor of large ones because the larger inner pressure makes them more thermodynamically unstable. We can now generalize this result to a generic surface with the *Laplace theorem*:

"The increase in hydrostatic pressure Δp that occurs upon traversing the boundary between two fluids is equal to the product of te surface tension γ and the curvature of the surface C:"

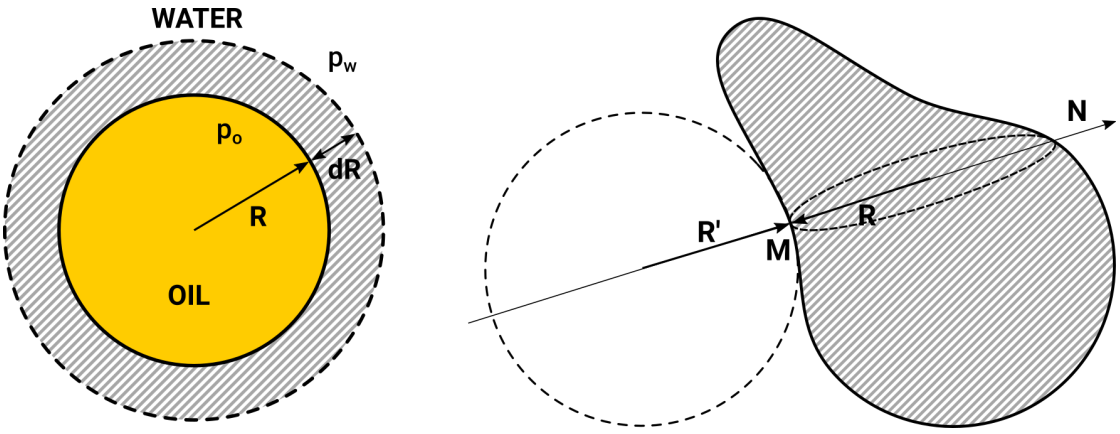

Figure 1.2 : From left to right: schematic representation of the surface displacement of an oil droplet in water, case of study to understand the concept of curvature of a surface.

$$\Delta p = \gamma \left(\frac{1}{R} + \frac{1}{R'} \right) = \gamma C \tag{1.4}$$

A clear example of how to measure the curvature of a surface is given by the example of a pear shape solid as depicted in fig. 1.2 (right). The curvature at a point M is determined by taking the normal $\mathbf{N}$ to the surface at that point. Next, the volume is cut along two mutually orthogonal planes intersecting each other along $\mathbf{N}$. The intersection of these planes with the surface of the volume defines two curves, the radii of curvature of which are R and R'. If the center of the circumference is inside the volume the value of the radius is taken with the positive sign, otherwise is taken with the negative sign.

§ 1.2. Coalescence of droplets

In the previous section, we introduced the Laplace equation and showed how it explains the coalescence of small droplets oil in water emulsions.
A liquid/liquid emulsion is a system formed by the dispersion of small droplets of one liquid in another. To form small droplets, it is necessary to work with weak interfacial energies (otherwise capillary effects, which favor the formation of large drops, destabilize the emulsion by causing droplets to coalesce); in practice, it is necessary to use surfactants to form an emulsion. Depending on the relative concentrations, different types of emulsions can be distinguished: simple emulsions, emulsion-gels, bi-liquid foams. We also introduce a classification according to the size of the droplets: macro-emulsions

are systems made up of droplets larger than one micrometer (e.g. milk), while micro-emulsions are made from submicrometric droplets. Macro-emulsions are in a metastable state, and are destined to undergo a separation of phases (for milk, this leads to the spontaneous formation of cream). Phase separation is energetically favorable because it minimizes, at a fixed volume, the area of contact between phases [55]. The study of the coalescence of droplets is a problem of major interest because of the implications in the emulsion stability and the generation of reaction platforms in closed microfluidics [56]. The coalescence phenomenon between two droplets immersed in another liquid is well described in a work by K. Chester in 1991 [57]. Following his reasoning, we can describe the shape of two droplets making contact using three different parameters: the radius of the drops R, the radius of the contact area between the drops a and the thickness of the film between the drops h (see fig. 1.3). In this case to perform the coalescence it is necessary to drain the liquid film between the droplets. The viscous force associated to the drainage of the film slows down the coalescence and can be quantified as [58]:

$$F_\eta = \frac{3}{2}\pi\eta\frac{a^4}{h^3}u \tag{1.5}$$

where η is the viscosity of the fluid around the two droplets and u is the velocity of approach of the droplets. The larger the approaching velocity is, the larger the viscous force acting against the motion due to the drainage of the film. After the drainage of the film has taken place, the two droplets can make contact. If the emulsion is stabilized with a surfactant, there is another repulsion effect to overcome in order to obtain the coalescence. In this case the coalescence phenomenon is linked to the probability of the displacement of the surfactant on the surface that allows the coalescence to take place [59].The coalescence can be enhanced either by the presence of a long range attraction force between the droplets that increases the pressure at the contact point, or by the change in ion concentration of the solution that reduces the repulsion due to the surfactant. To quantify these two contributions, we can write the characteristic time as:

$$\tau \sim \frac{e^{-\Delta P}}{[ion]} \tag{1.6}$$

Once the barrier between the drops is broken, the coalescence begins. In the center and on the right of fig. 1.3, the different steps of the coalescence process are described. In particular, the series of snapshots in the center [60] resembles the onset of the phenomenon with a wave propagating from a critical point in the center to the rest of the droplet for a case of two silicone oil droplets (1000 cSt) spreading and coalescing on a

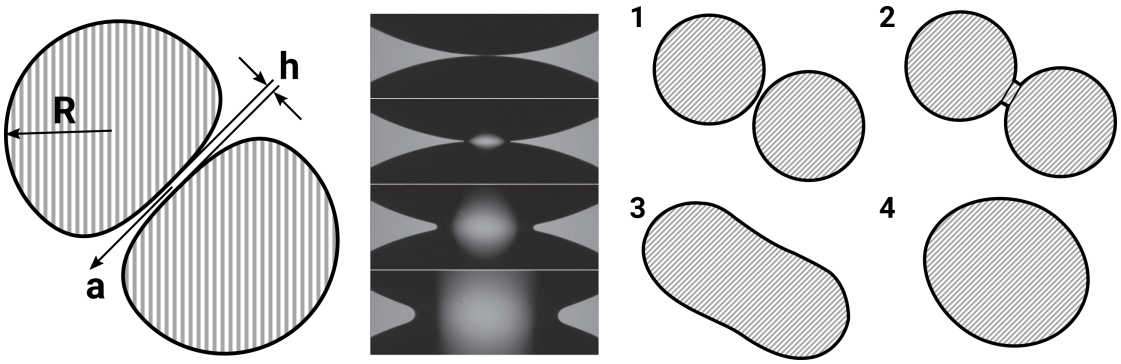

Figure 1.3 : From left to right: schematic representation of two droplets before the coalescence, optical microscopy images of two silicone oil droplets (1000 cSt) spreading and coalescing on a flat polystyrene substrate (dark regions are oil, light regions are background) [60], schematic representation of the different steps of the coalescence process: contact between the droplets (1), beginning of the coalescence (2), end of the coalescence (3), arrangement of the shape to minimize the surface area (4).

flat polystyrene substrate. Instead the schematic representation on the right represents the whole description of the phenomenon: contact between the droplets (1), beginning of the coalescence (2), end of the coalescence (3), arrangement of the shape to minimize the surface area (4).

§ 1.3. Wetting of drops on horizontal substrates

The presence of the surface tension has major effects also when a third solid phase is present in the system. The study of how liquids spread on solid surfaces is called *wetting*. Specific wetting topics of interest for this thesis are discussed in different subsections: the contact angle (1.3.1), heterogeneous and rough surfaces (1.3.3), liquid surfaces 1.3.4 and the shape of drops (1.3.2).

§ 1.3.1. The contact angle

The first consideration that has to be made when we consider a system in which a liquid and a solid interact is that there exist two different regimes of wetting: complete and incomplete wetting. The parameter that distinguishes them is the *spreading parameter* S, which measures the difference of the energy of the substrate when it is dry or wet:

$$S = [E_{substrate}]_{dry} - [E_{substrate}]_{wet} \tag{1.7}$$

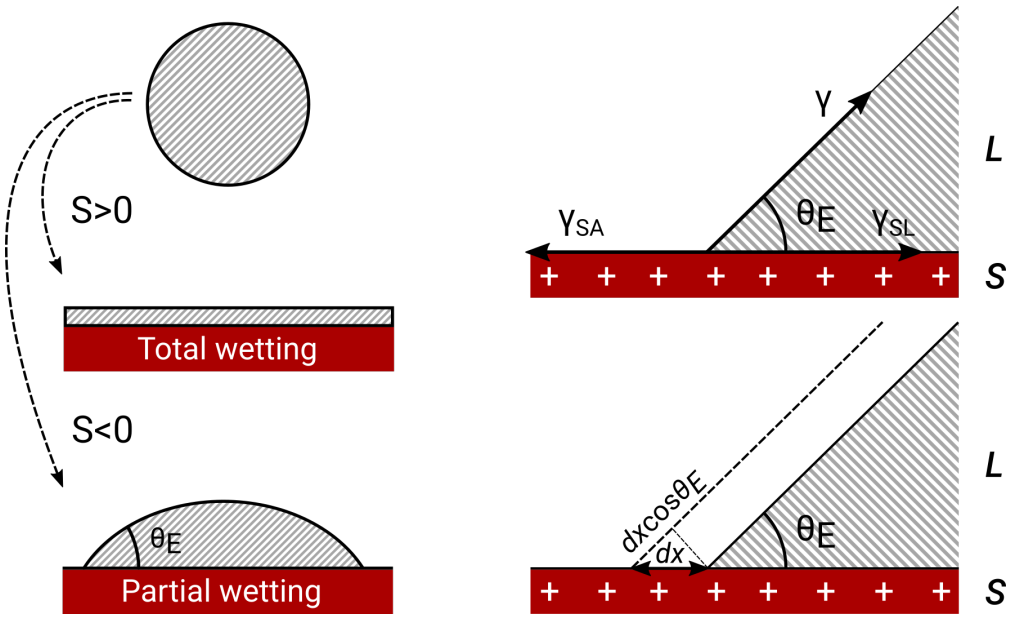

Figure 1.4 : From left to right: schematic representation of the consequences of different values of spreading parameter, two different methods to obtain the contact angle: studying the forces (top) or studying the works (bottom).

or

$$S = \gamma_{SA} - (\gamma_{SL} + \gamma) \tag{1.8}$$

where the three parameters γ are the surface tension at the solid/air, solid/liquid and liquid/air interfaces, respectively. If $S > 0$ the liquid spreads completely on the surface of the solid in order to lower its surface energy (complete or total wetting). If instead $S < 0$ the drop does not spread and forms at equilibrium a hemispherical cap resting on a surface with a contact angle θ_E (incomplete or partial wetting). There are two main ways to obtain a formula that quantifies the value of the contact angle on a surface. The first method (see figure 1.4 right, top) consists of evaluating the capillary forces acting on the line of contact (also called triple line) and equating their sum to zero. The equilibrium of this forces yields:

$$\gamma cos\theta_E = \gamma_{SA} - \gamma_{SL} \tag{1.9}$$

known as Young's relation for the contact angle. The projection of the capillary force onto the vertical axis is balanced by a reaction force exerted by the horizontal surface: if the surface soft, the contact leads to a deformation of the surface (for example this phenomenon can be seen when a drop of water is deposited on a surface with fresh paint,

the deformation leaves the mark on the surface if the drop is dried).
The second method relies on calculating the work done by moving the contact line of a distance dx:

$$\delta W = (\gamma_{SA} - \gamma_{SL})dx - \gamma cos\theta_E \tag{1.10}$$

At equilibrium this work equals zero and we find again the expression in equation 1.9.
There are several methods to obtain an experimental measure of the contact angle. In the case of large angles ($\geq\sim 40°$), that include all the examples presented in this thesis, the measure of the contact angle is performed taking a side view photograph of the droplet and using the snapshot to determine the angle.
Using the contact angle of water as a reference parameter, we can define three classes of surfaces:

- Hydrophilic surfaces: $\theta_E < 90°$
- Hydrophobic surfaces: $90° < \theta_E < 150°$
- Superhydrophobic surfaces: $\theta_E > 150°$

Figure 1.5 shows three examples of snapshots of water droplets on the three different surfaces. The hydrophobic/hydrophilic character mainly depends on the chemical nature of the surface. Superhydrophobicity requires also the presence of a rough surface at the micro/nano scale.

For a real surface the apparent equilibrium contact angle θ_E is not sufficient to describe the dynamics of a sessile drop due to the presence of chemical and morphological inhomogeneities which act as pinning sites of the contact line [1]. It is then useful to introduce the contact angle hysteresis ($\Delta\theta$) that is the key macroscopic parameter governing drop dynamics. The value of the contact angle varies between a maximum value (θ_A, advancing contact angle) and a minimum value (θ_R receding contact angle). As we will see in section 1.4 $\theta_A(\theta_R)$ corresponds to the angle that the a drop assumes when moving forward(backward) the contact line. We can define:

$$\Delta\theta = \theta_A - \theta_R \tag{1.11}$$

When we deposit a drop on a surface, it will assume a contact angle of equilibrium $\theta_R < \theta_E < \theta_A$, the exact value depending on the local properties of the surface in proximity of the contact line and on the way we have deposited the droplet on the surface. These facts have the obvious implication that the measure of the contact angle in a non-controlled environment is a very difficult task. To improve the quality of the

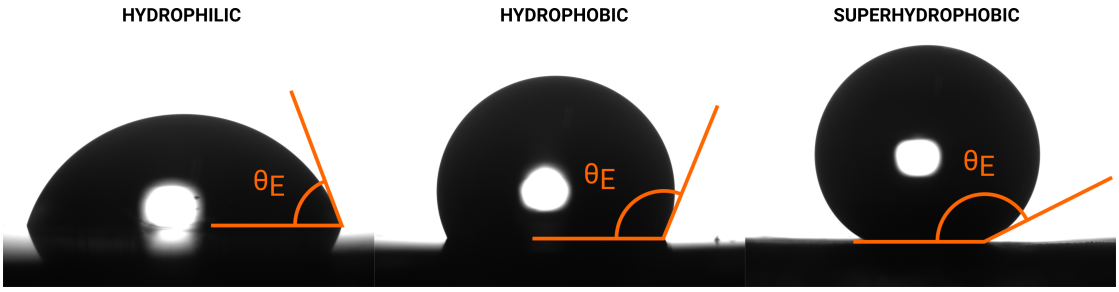

Figure 1.5 : From left to right snapshots of water droplets of 4 μl deposited on: a glass substrate (hydrophilic), a teflon substrate (hydrophobic) and a lotus leaf (superhydrophobic).

measurement the experimental procedure of preparation and cleaning of the surface and of deposition of the droplet must be performed accurately

§ 1.3.2. The shape of drops

The shape of drops on flat surfaces is the result of the balance between the surface tension and the gravitational force. To better describe the system it is necessary to introduce a new quantity called *capillary length* λ. The comparison between the capillary length (λ) and the characteristic length of the system l allow to understand which of the two contributes between gravity and surface tension is the most important to determine the shape of a droplet: if $l < \lambda$, the surface tension dominates, if instead $l > \lambda$ the gravitational force dominates.
The capillary length can be estimated by comparing the Laplace pressure γ/λ to the hydrostatic pressure $\rho g\lambda$ at a depth λ in a liquid of density ρ. Equating these two pressures defines the capillary length:

$$\lambda = \sqrt{\frac{\gamma}{\rho g}} \tag{1.12}$$

The value of λ is usually of the order of a millimeter (even for mercury which has large γ and ρ). To strongly change the value of λ without changing the chemical properties of the liquid it is necessary to change the value of g. This can be achieved by working in micro gravity or changing the density of the liquid around the droplet to take advantage of the buoyancy force or again taking advantage of an external force parallel to the gravitational force.
The capillary length plays a fundamental role in determining the shape of drops on a surface. At small volumes the shape is hemispherical. If we increase the volume we can observe that, over a certain volume, the drop tends to flatten under the influence

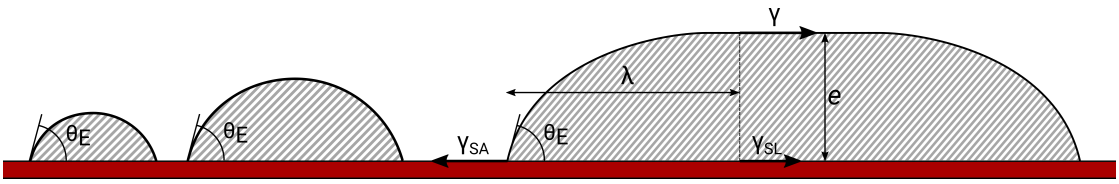

Figure 1.6 : From left to right schematic representation of the side view of different droplets at increasing volume on a surface, the increase of volume over a certain value lead to the formation of a flat droplet of defined thickness e.

of gravity. The shape of the drop will therefore change from perfectly similar to a hemispherical cap to almost completely flat depending on whether its radius R is small or large compared to the capillary length λ.
For the case of $R >> \lambda$ at equilibrium, the drop takes the shape of a puddle of thickness e. The value of e can be calculated and is linked with the value of λ and of θ_E. To calculate the relationship between these parameters we consider the horizontal forces acting on a portion of liquid. The equilibrium of the forces can be expressed as:

$$\frac{1}{2}\rho g e^2 + \gamma_{SA} - (\gamma + \gamma_{SL}) = 0 \tag{1.13}$$

where $\frac{1}{2}\rho g e^2$ is the hydrostatic pressure P integrated over the entire thickness of the liquid. Remembering the relations in the young equation (1.9) we find that:

$$\gamma \cdot (1 - \cos\theta_E) = \frac{1}{2}\rho g e^2 \tag{1.14}$$

which leads to:

$$e = 2\lambda \sin\left(\frac{\theta_E}{2}\right) \tag{1.15}$$

It is interesting to notice that for angles not too small the thickness of the puddle is of the same order of magnitude of λ.

§ 1.3.3. Heterogeneous and rough surfaces

One possible way to account for the imperfections of a real surface is to consider the case of a heterogeneous surface with domains of different wettability (see fig. 1.7.a). If the domains are small in comparison to the dimension of the droplet, the system is well described by the *Cassie Baxter model* [61]. In this case the drop will assume a static contact angle given by the weighted average of the wettability characterizing the different materials forming the surface. For the most simple scenario a flat surface is formed by only two different materials with contact angles θ_1 and θ_2. The resulting contact angle depends on the two contact angles and on the fraction of each materials under the droplet:

$$\cos\theta_{CB} = f_1 \cos\theta_1 + f_2 \cos\theta_2 \tag{1.16}$$

where f_1 and f_2 are the fractions of surface occupied by the materials 1 and 2.
If a surface is rough, liquid can fill all the voids as shown in figure 1.7.b. The roughness is quantified with a parameter $r \geq 1$, defined as the ratio between the real surface to the apparent surface area [62], which is equal to 1 in the case of a flat surface [63]. If we consider a displacement of the contact line as in equation 1.10 taking into account the contribute due to the roughness we find:

$$\delta W = r(\gamma_{SA} - \gamma_{SL})dx - \gamma cos\theta^* \tag{1.17}$$

At equilibrium, δW is equal to 0 and using the Young equation 1.9 we find the so called Wenzel equation:

$$\cos\theta^* = r\cos\theta_E \tag{1.18}$$

If we look at this result we can notice that:

- if $r = 1$ we recover the solution for a flat surface
- if the surface is hydrophilic ($\theta_E < 90°$), enhances its hydrophilicity, e.g. makes the contact angle lower
- if the surface is hydrophobic ($\theta_E > 90°$), enhances its hydrophobicity, e.g. makes the contact angle higher

We can conclude by saying that the roughness enhances the wetting properties of the surface.
This first analysis can be completed with the particular case of a droplet that does not

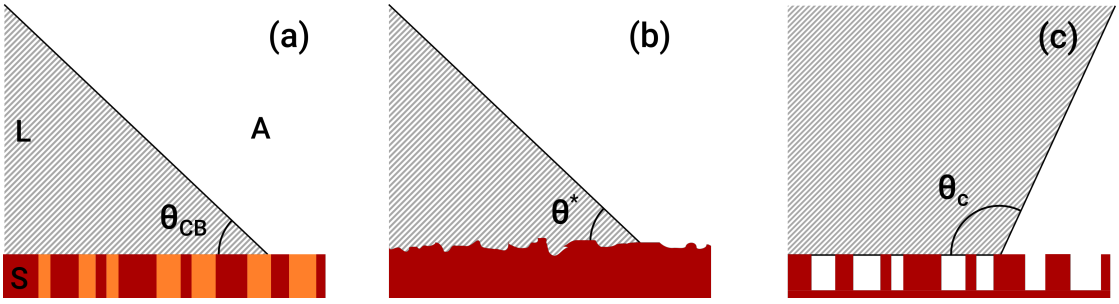

Figure 1.7 : From left to right schematic representations of a water drop on: a) an heterogeneous surface with domain with different wetting properties, b) a generic rough surface, c) an hydrophobic rough surface.

fill the underlying cavities of the surface (see fig 1.7.c) (fakir or Cassie state [64]). In this case the surface energy of the dry solid is lower than that of the wet solid and, as a consequence, air pockets are trapped between surface structures. Knowing that the water-air contact angle is $\theta_{air} = 180°$ we can use the Cassie-Baxter relation to write:

$$\begin{aligned} \cos\theta_{CB} &= f_A \cos\theta_{air} + f_S \cos\theta_c \\ &= (1 - f_S)(-1) + f_S \cos\theta_c \\ &= -1 + f_S(1 + \cos\theta_c) \end{aligned} \tag{1.19}$$

This formula describes very well what happens with the superhydrophobic surfaces. In the case of the lotus leaf, for example, the micro-nanoscopic structures of the surface of the leaf enhance the air trapping under the water droplets [65]. From equation 1.19, it is easy to see that the higher the fraction of air under the droplet, the higher the contact angle. In the lotus leaf the presence of a multi level roughness guarantee that the percentage of air under the droplet is very high and this produces contact angles $\theta_E \geq 150°$. Until now we have always talked about liquid drops on solid surfaces and we have seen approaches to vary the hydrophobicity by modifying either physical or chemical properties of a surface. For example, in the case of physical patterning of a hydrophobic material, the surface roughness can be considerably increased to reduce the surface-liquid contact area by introducing air pockets within the structure. The main advantage of these substrates is that high contact angle can bring to high water repellency properties and so hypothetically can be used in a lot of applications. On the other side, the main disadvantage of such surfaces is that heterogeneous wetting (Cassie-Baxter regime or superhydrophobic regime) can turn into homogeneous wetting (Wenzel

regime) by external stimuli such as pressure and vibrations [66] which is characterized by strong pinning. In other words it is the CA hysteresis rather than the CA that determines the water repellency of a surface.
As we said before, the CA hysteresis is linked with the presence of imperfections of the substrates either of chemical and morphological nature. In the past the effort to obtain real surfaces without defects was focused on developing more and more complicated surface treatments. Recently has been explored a novel approach to the problem: liquid surfaces.

§ 1.3.4. Liquid surfaces

A different approach to achieve low-hysteresis properties involves surfaces containing pockets of a lubricating liquid rather than of air [12] [13] [2]. These novel functional surfaces, known as liquid-infused surfaces (LIS) [12] , lubricant-impregnated surfaces (LIS) [14] or slippery liquid-infused porous surfaces (SLIPS) [13] (in the following identified with the acronym LIS), are textured materials usually imbibed by a lyophilic oil as shown in Figure 1.8. The premise for such a design is that a liquid surface is intrinsically smooth down to the molecular scale, provides immediate self-repair by wicking into damaged sites in the underlying substrate, is largely incompressible, and can be prepared to repel immiscible liquids of virtually any surface tension [13].
The approach just described is inspired by the Nepenthes pitcher plant that uses its external skin to lock-in an intermediary liquid that then acts as the repellent surface [67]. In pitcher plants, this liquid film is aqueous and effective enough to cause insects that step on it to slide from the rim into the digestive juices at the bottom by repelling the oils on their feet [68].
These surfaces can be replicated synthetically in different ways. To mimic the solid texture of the Nepenthes pitcher plant an ample variety of synthetic substrates has been used to trap the lubricant [2]: Teflon nanofibrous membranes [13], hierarchical textures comprising microposts covered with nanofeatures fabricated using laser ablation [69], regular arrays of microposts of different shape [70] and parallel grooves [71] made by standard photolithographic techniques, silicone oil films deposited on a substrate and annealed at high temperature [72] and self-assembly polystyrene microbeads on scotch tapes with the aid of an inkjet printer [73].
Since a drop on a LIS comprises four distinct phases (the textured solid, the lubricant, the liquid that needs to be shed and the surrounding gas,), it exhibits a rich phenomenology. Actually, there exist 12 different thermodynamically stable wetting states depending on the interfacial tensions, the roughness and the solid fraction [14]. While thermodynam-

ical arguments are sufficient to predict the presence of different drop configurations on LIS, to date there is no theory for computing the corresponding values of the contact angle and contact angle hysteresis, despite their relevance as key design parameters for any application. The most relevant configurations favouring slippery behaviour, i.e. configurations where the drop does not wet the substrate, are schematically represented in the snapshots a, b, c, d of figure 1.8. The drop may rest on top of the lubricant (Figure 1.8 (a) and (b)), it may sink into the lubricant and rest on top of the protrusions (Figure 1.8 (c) and (d)) or it may penetrate into the textured substrate (not shown). Either the lubricant cloaks the drop (Figure 1.8 (a) and (c)) or the drop sinks into the lubricant untill it reaches a certain height, at which point the lubricant forms an annular wetting ridge around the drop that is pulled above the substrate (Figure 1.8 (b) and (d)). Depending on the interplay of the interfacial tensions, a LIS can exhibit zero (Figure 1.8 (a)), one (Figure 1.8 (b) and (c)) or two (Figure 1.8 (d)) three-phase contact lines.
To obtain a stable impregnation, the contact angle $\theta_{os}(v)$ of the impregnating oil (subscript 'o') on the smooth solid (subscript 's') in the presence of vapor (indicated as 'v') has to be less than a critical angle θ_c, given by the expression:

$$\theta_c = \cos^{-1} \frac{1-\phi}{r-\phi} \tag{1.20}$$

where ϕ is the fraction of the projected area of the surface that is occupied by the solid and r is the roughness of the substrate [12]. The texture tops are submerged or exposed depending on the spreading coefficient of the impregnating oil on the solid in the presence of the drop given by $S_{os}(w) = \gamma_{sw} - \gamma_{ow} - \gamma_{os}$, where γ_{ij} is the interfacial energy between the phases i and j: if $S_{os} > 0$ (complete spreading of the lubricant), a thin Van Der Waals film submerges the top of textures and weakens or even eliminates pinning sites [14]. For a complete description of the droplet wetting state is also important to consider the possibility of cloaking (or encapsulation) of drops by the impregnated oil because it may prevent condensate growth, accelerate oil depletion from the texture and contaminate the droplets [74]. The cloaking occurs when the spreading coefficient of oil on water in the presence of vapour is positive ($S_{ow}(w) = \gamma_{wv} - \gamma_{ov} - \gamma_{ow}$). In the case of water drops, cloaking occurs with silicone or fluorinated oils as lubricants, whereas no cloaking takes place with ionic liquids. The extremely weak pinning of LISs makes these surfaces ideal for a variety of important applications. For intance the apparent contact angle on LISs is typically around 90°, that is low enough to provide significant contact with the substrate and thus significant temperature differences between both edges of the deposited droplet, unlike what is observed on superhydrophobic surfaces

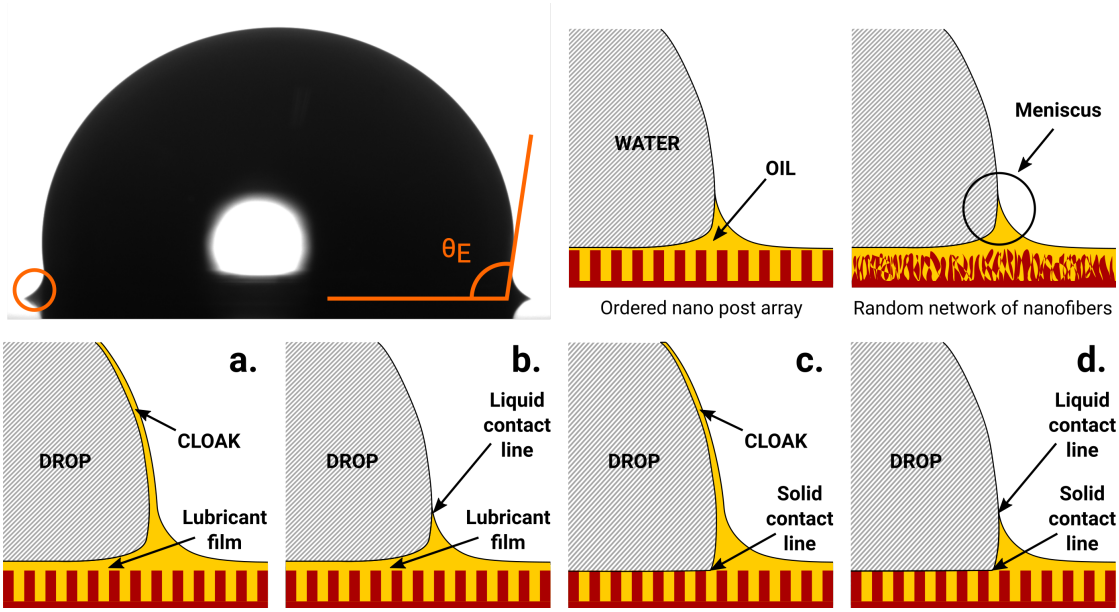

Figure 1.8 : TOP: from left to right: snapshot of a water droplet deposed on a LIS, schematic representations of a water drop on a LIS with an ordered nano post pattern, schematic representations of a water drop on a LIS with a random network of nano fibers. BOTTOM: possible wetting configurations of a slippery lubricant-impregnated surface (LIS): (b) and (d) the lubricant does not cloak the drop; (a) and (c) the lubricant cloaks the drop. Drops on LISs can exhibit zero (a), one (b) and (c) or two (d) three-phase contact lines.

for which contact is minimized. In other words LISs can enhance water transportation taking advantage of temperature gradients. Using a lubricant with viscosity comparable to that of water and temperature gradients as low as 2 K/mm, drops can propel at 6.5 mm/s [69], that is at least five times quicker than reported on conventional substrates [2]. Condensation of water drops on a LIS occurs with enhanced droplet mobility compared to superhydrophobic surfaces. The enhancement results from the fact that the condensed droplets stay afloat on the lubricant with minimal pinning to the surface compared for example with superhydrophobic surfaces, where condensation occurs within the texture so droplet get strongly pinned [2]. Another advantage of the LISs is that they can be iceophobic [75] [76]. Finally, LISs are promising candidates for anti-biofouling coatings, alternative to common methods based on toxic release, intensive chemical attack or mechanical removal [77] and for anti marine macrofouling organisms coatings [78].

§ 1.4. Sliding of droplets

This section will give an insight on the sliding properties of droplets on inclined surfaces. First the discussion will focus on the transition between static and dynamic phenomena deepening the role of the contact angle hysteresis (1.4.1), then the characteristics of the motion on a partially wetted plane will be presented (1.4.2) and, in the end, the focus will be moved to the properties of sliding on a LIS (1.4.3).

§ 1.4.1. The role of contact angle hysteresis on the sliding

To study the properties of moving droplets on inclined surfaces let us start from what we know about the contact angles. As explained previously, the defects on the solid surfaces cause a variation in the contact angles between a minimum and a maximum value. These two values are directly linked to the dynamic behavior, to see how, let us consider a droplet of water on a horizontal substrate and assume that the contact angle has the same value all around the droplet. At a certain point we begin to tilt the substrate in a certain direction: the shape of the droplet is no more symmetric [79] and the contact angle will no more assume the same value all around the droplet, increasing in the lower part and decreasing in the upper one (see fig. 1.9). The lower angle increases and the upper angle decreases until the droplet begins to slide. The two critical angles are called advancing (θ_A) and receding (θ_R) angles and the critical value of the tilting angle that should be applied to obtain the droplet movement is called sliding angle α_S. At this point it should be clear that the greater the contact angle hysteresis ($\theta_A - \theta_R$) the greater the sliding angle α_S. This fact is a clear indication of the link between the

contact angle hysteresis and the droplet-surface friction. To find the relation between the sliding angle α_S and contact angle hysteresis we can consider the work done to move the drop by a distance dx along the plane [80]. For the sake of simplicity, we assume an almost rectangular shape of the contact area of width w, as sketched in fig. 1.9. The active force is that gravitational and the corresponding work relative to a displacement equal to dx is:

$$W = mg \sin \alpha_S dx \tag{1.21}$$

where m is the mass of the droplet and g is the gravity acceleration. Moving down the plane, the droplet will wet an area equal to wdx and the same area will be dewetted by the rear edge. The work done in wetting a unit area of solid surface is equal to $\gamma(1+\cos\theta_A)$ and similarly, the work for dewetting a unit area of surface is $\gamma(1+\cos\theta_R)$. Hence the total work associated to capillary forces is:

$$W = wdx\gamma(1+\cos\theta_R) - wdx\gamma(1+\cos\theta_A) \tag{1.22}$$

Combining eq. 1.21 and eq. 1.22 we obtain:

$$\frac{mg\sin\alpha_S}{w} = \gamma(\cos\theta_R - \cos\theta_A) \tag{1.23}$$

A generalization of this formula valid in cases of different droplet shape is:

$$mg\sin\alpha_S = kR\gamma(\cos\theta_R - \cos\theta_A) \tag{1.24}$$

where R is the droplet radius and k is a dimensionless number linked with the geometry of the contact line shape [81]. The equation 1.24, known as Furmidge's equation, links the sliding angle with the values of θ_A and θ_R. The only problem with this formula is that the value of k is not of easy calculation.

§ 1.4.2. Motion of droplets on partially wetted surfaces

Drops on a surface inclined by more than the sliding angle move on the plane being subject to three forces, whose in-plane components, as showed in fig. 1.9, are [82] [83]:

- component of the gravitational force $\sim \rho V g \sin\alpha$
- viscous drag on the surface $\sim -\eta U V^{1/3}$
- interfacial force $\sim -\gamma\Delta_\theta V^{1/3}$

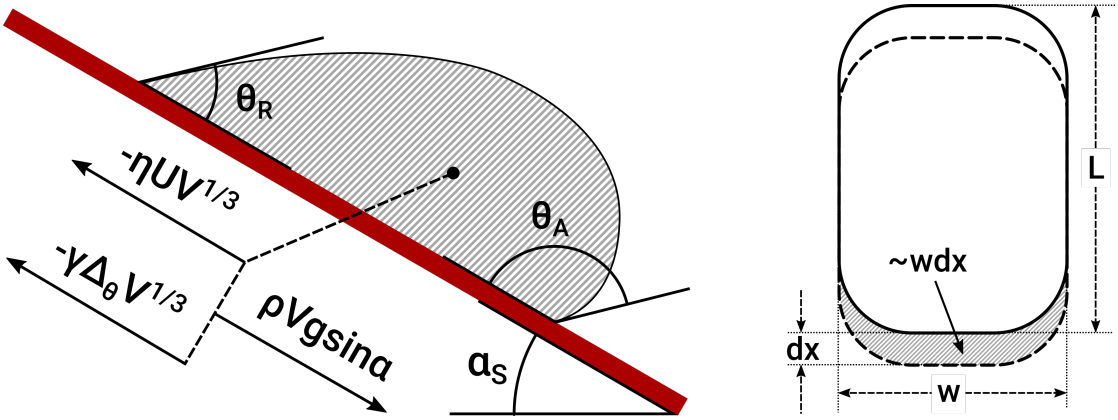

Figure 1.9 : From left to right schematic representation of the side and top view of a sessile droplet sliding down an inclined plane.

where ρ is the liquid density, V the droplet volume, α the plane inclination, η the liquid viscosity, U the droplet velocity, γ the surface tension and Δ_θ is a non dimensional factor depending on the distribution of the contact angle around the perimeter of the droplet and on the perimeter shape. Once the motion has started, forces will balance and the droplet will reach a constant velocity and almost a constant shape. Force balance implies a scaling law of the form:

$$Ca \simeq Bo - Bo_c \tag{1.25}$$

where:

- $Ca = \dfrac{\eta U}{\gamma}$ is the capillary number that represents the relative effect of viscous forces versus surface tension;
- $Bo = \dfrac{\rho g \sin\alpha V^{2/3}}{\gamma}$ is the Bond number relative to the gravity component versus the surface tension:
- Bo_c is a constant that depends on the contact angle hysteresis through Δ_θ

Ca and Bo are dimensionless numbers and so are very useful to compare measurements in different experimental situations when the drop is moving (droplets with different volumes, viscosities, sliding angles etc.). Another interesting aspect regarding the sliding of droplets is the study of the internal flow. Both theoretical studies [84], [85], [86] and experimental observations [87] have been conducted to understand the flows. Gao and McCarthy [88] postulated two mechanisms for droplets movement:

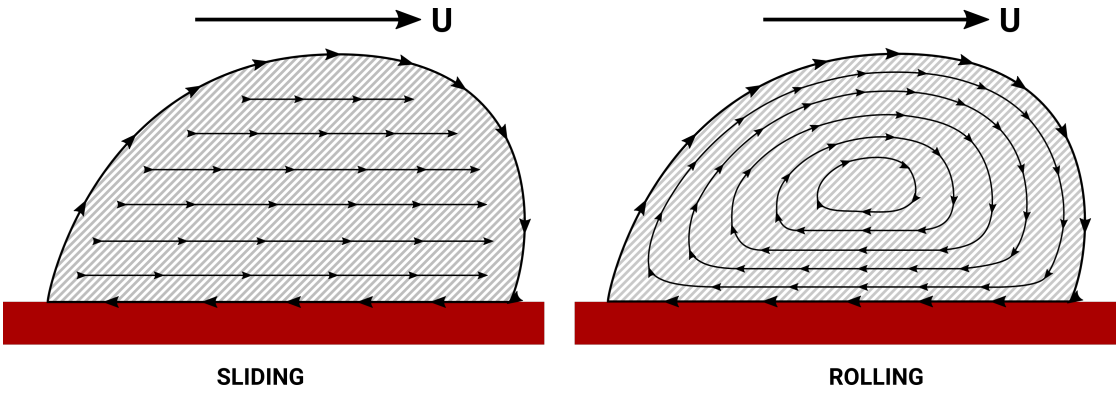

Figure 1.10 : Schematic representation of the flux inside a sessile droplet sliding down an inclined plane in the sliding (left) and in the rolling (right) configuration.

- a *sliding* motion (see fig. 1.10 left): particles near the solid liquid interface exchange their position with those at the gas-liquid interface, while the bulk of the liquid translates rigidly. Particles in the rotating layer undergo a movement similar to the motion of a tread of a caterpillar tank;
- a *rolling* motion (see fig. 1.10 right): the whole fluid mass assumes a circulatory movement.

These behaviors have been observed in simulations [84], [85], [86] and in experimental measurements [87]. In many cases, the internal motion of the fluid is a mix between the two situations. The predominance of one effect over the other is regulated by the viscosity contrast between the droplet fluid and the surrounding fluid [86]. In particular when the liquid droplet is more viscous than the surrounding one the rolling effect will dominate. On the opposite, if the surrounding fluid is more viscous the dynamics shifts toward the external fluid and so the drops slide in this case. This is consistent with intuition, for example a "bubble" will simply slide in a liquid rather than roll when moving on a surface.

§ 1.4.3. Motion of droplets on LIS

As expected, the dynamics of drops on inclined LIS is quite rich [14]. The case of the sliding on LISs is particular because the liquid surface not only is flat and without defects but because it presents also completely different boundary conditions with respect to the solid surface. This kind of surfaces presents sliding angles near zero and the contact angle hysteresis is below 5° degrees [13], [14], [72], [89]. The presence of two interfaces (solid-oil and oil-liquid) complicates the analysis of the droplet dynamics.

The friction associated to sliding droplets on LIS has been studied in [89]. Dissipation occurs in both water and oil: on one hand water moves inside the drop, on the other hand oil moves under the drop and along the edge meniscus. Which of these three factors dominates (if one dominates over the others) depends on the ratio between the droplet and the infused oil viscosity (η_w and η_o) and on the droplet velocity. In general three distinct situations can occur:

- $\eta_w >> \eta_o$ In this case the dissipation has a viscous origin and the interfaces keeps a quasi static shape [89]. The velocity satisfies a relationship similar to the one valid for a droplet sliding on a partially wet plane:

$$v \simeq \frac{\rho g \sin\alpha V^{2/3}}{\eta_w} \tag{1.26}$$

- $\eta_o > \eta_w$ Dissipation is expected to take place in oil, that is, in the underlying film and in the surrounding meniscus. If we consider the dynamic nature of the meniscus which is constantly pushed by the moving drop, the analysis of the viscous effects in the front edge of the moving meniscus yields superlinear friction:

$$v \simeq B \sin^{3/2}\alpha \tag{1.27}$$

  where the factor B include several contributes linked to the geometry of the pattern below the oil. As the driving force is increased, the wedge dissipation is suddenly suppressed, which leads to a different dynamical regime that seems to arise from the self-lubrication of the drop where:

$$v \propto \sin^3\alpha \tag{1.28}$$

  explained assuming that oil is constantly extracted from the texture by water surface tension before being reinjected below the drop [89].

In the case $\eta_o > \eta_w$ the oil-water interface moves at a negligibly small velocity relative to that of the droplet's center of mass. If we add particles to the water droplet and then track their displacement we can observe that the particles are subjected to a circular motion [14] i.e. the droplet undergoes rolling motion.

Chapter 2

Ferrofluids

This chapter deals with the physical properties of the ferrofluids. After giving a brief definition in section 2.1, the stability properties of the material will be studied in section 2.2, then we will focus on the magnetic properties and on the forces of interaction in section 2.3, on the topological instabilities of the ferrofluids in section 2.4 and on the magnetoviscous effect in section 2.5. Finally some techniques of synthesis and characterization will be presented in section 2.6.

§ 2.1. Definition

Ferrofluids are colloidal suspensions of ferromagnetic nanoparticles [34] and present themselves as black or dark brown liquids (this does not allow to study the internal structure using visible light). A colloidal suspension is in general a mixture between a liquid at the macroscopic scale (matrix phase) and another material at submicromiter size (dispersed phase). In the case of ferrofluids the dispersed phase is composed of ferromagnetic nanoparticles, which can have different shapes, chemical composition and mean size [90] [91]. These magnetic particles are so small that they behave similarly to the molecules of the liquid in which they are suspended. However, each particle acts like a small permanent magnets [33], which can interact with the external magnetic fields. Such magnetic interaction displays itself through different forces and pressures that allow to control the ferrofluid's viscosity [39], shape [52], motion [49] etc.
The versatility of the ferrofluids makes them of interest both for fundamental and more applied studies. Ferrofluids are widely used as liquid seals and lubricants held in place by magnetic fields, while actuation with dynamic magnetic fields allow building of ferrofluid based pumps, valves and tunable optical systems [92]. The possibility of tuning the interaction with the magnetic field makes the ferrofluids very interesting also for

various microfluidic applications [93] [92].

§ 2.2. Colloid stability

To obtain a ferrofluid, precise conditions for the physicochemical stability must be satisfied [34] (pag. 34). To understand the physical origin of the stability criteria it is useful to write the expressions of the various energy terms per particle and confront them. Initially we will consider the thermal energy as the only factor that opposes the precipitation and the aggregation of the nanoparticles. The thermal energy can be quantified as:

$$\text{thermal energy} \sim kT \tag{2.1}$$

where k is the Boltzmann's constant and T is the absolute temperature.
The nanoparticles are also subjected to the action of the gravitational field and the presence of the external magnetic field. The corresponding interaction energies can be estimated as:

$$\begin{aligned} \text{magnetic energy} &\sim MBV \\ \text{gravitational energy} &\sim \Delta\rho V g L \end{aligned} \tag{2.2}$$

where M is the magnetization of the single nanoparticle, B is the applied magnetic field, V is the volume of the nanoparticle, $\Delta\rho$ is the difference in density between the nanoparticle material and the carrier fluid and L is the elevation in the gravitational field (see fig. 2.1 left).
In a magnetic field gradient, the nanoparticles are attracted to where the magnetic field is higher while the thermal motion acts to disperse them all over the volume of the liquid. If the thermal energy is greater than the magnetic energy, the particles do not segregate by the action of the magnetic field, that is:

$$\frac{\text{thermal energy}}{\text{magnetic energy}} = \frac{kT}{MBV} > 1 \tag{2.3}$$

Evaluating the volume of a single nanoparticle as $V = \pi d^3/6$, we can write the previous relation in terms of a condition on a minimum diameter:

$$d < (6kT/\pi MB)^{1/3} \tag{2.4}$$

If, for example, we substitute the maximum magnetic field and magnetization values employed in this thesis ($B \approx 0.5$ T and $M \approx 50$ kA/m) inside the equation the maximum diameter to guarantee the stability is around $d \simeq 10$ nm at room temperature. This limit has also the conseguence that each nanoparticle corresponds to a single magnetic dipole because of its size.
The same reasoning can be followed to establish the criterion associated with the presence of a gravitational field. Again, we compare the gravitational energy with the thermal energy:

$$\frac{\text{thermal energy}}{\text{gravitational energy}} = \frac{kT}{\Delta\rho V g L} > 1 \tag{2.5}$$

If we consider nanoparticles of size $d < 10$ nm and typical values of ferrofluid thickness L ($\approx$1 cm) and $\Delta\rho$ ($\approx 4000\ kg \cdot m^{-3}$), the ratio between the two energies become far greater than one at room temperature.
Until now we have considered the interaction of the nanoparticles with the external fields but the nanoparticle interact also among themselves. There are two main contributions that favor the agglomeration of the nanoparticles: the dipole-dipole energy and the Van der Waals interaction. The dipole-dipole energy of two interacting magnetic particles separeted by a distance l can be written as:

$$E_{dd} = \frac{\pi}{9}\frac{\mu_0 M^2 d^3}{(l+2)^3} \tag{2.6}$$

If l is near to zero, we reach the maximum of interaction energy and the formula 2.6 becomes:

$$E_{dd} = \frac{1}{12}\mu_0 M^2 V \tag{2.7}$$

Again the thermal agitation tends to disrupt the agglomerates, accordingly we must consider the ratio:

$$\frac{\text{thermal energy}}{\text{dipole-dipole contact energy}} = \frac{12kT}{\mu M^2 V} \tag{2.8}$$

which yields the following criterion:

$$d < (72kT/\pi\mu_0 M^2)^{1/3} \tag{2.9}$$

The maximum particle size to avoid aggregation is again of the order of $d < 10$ nm. This estimate shows that normal magnetic fluids having particle size in the range up to

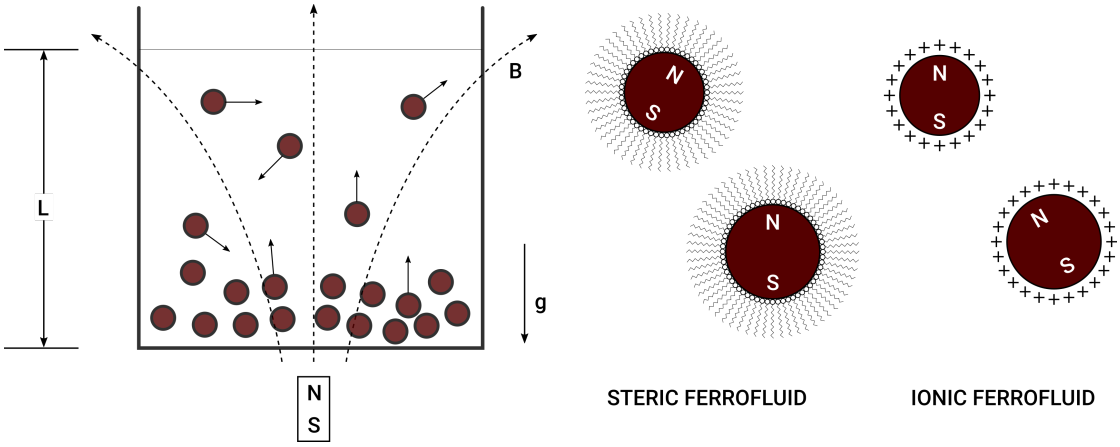

Figure 2.1 : Left: schematic representation of the forces acting on a ferrofluid. Center: stabilization of the nanoparticles using a steric repulsion. Right: stabilization of the nanoparticles using a ionic repulsion.

10 nm can be safely assumed as stable.

The case of the Van der Waals attractive force is a little more complicated. The Van der Waals forces arise spontaneously between neutral particles because of the fluctuating electric dipole-dipole forces that are always present. It turns out that this force of interaction varies as [34]:

$$\text{dipole fluctuation energy} = -\frac{A}{6}\left[\frac{2}{l^2+4l}+\frac{2}{(l+2)^2}+\ln\frac{l^2+4l}{(l+2)^2}\right] \tag{2.10}$$

where A is the so called *Hamaker constant* and for iron composites is around $10^{-19}N\cdot m$. This result obtained by Hamaker [94] indicates that the energy is proportional to l^{-1} for near spheres and l^{-6} for distant spheres. The l^{-1} indicates that infinite energy is necessary to separate two particles in contact, differently from the case of magnetic dipole attraction for which the value at contact was finite. It is thus necessary to prevent the contact between the particles by adding a repulsive force between the nanoparticles. This can be done in two ways as showed in figure 2.1: decorating the nanoparticles with a surfactant or charging the nanoparticles with electrical charges.

§ 2.3. Magnetic properties and forces of interaction

In the previous section we have seen that the thermal energy of the nanoparticles is sufficient to stabilize the colloid in almost all the cases. The thermal energy however has another important effect: it guarantees a continuous and random orientation of the magnetic dipoles inside the ferrofluid (each nanoparticle corresponds to a single magnetic dipole because of its size). If an external magnetic field is applied, the dipoles begin to align along the lines of magnetic field and, as the magnetic field is increased, this alignment extends to more and more nanoparticles, until, at a certain point, all nanoparticles are aligned with the field and the magnetization of the liquid reaches its maximum value. When the magnetic field is turned off, the dipoles return to have random directions thanks to the thermal agitation. As a result, the overall behavior of the ferrofluids is paramagnetic, i.e. they do not show any residual magnetization when the field is off. However, the ferrofluid exhibit a magnetic permeability that is orders of magnitude greater than the typical paramagnetic materials and this is obviously due to the fact that the nanoparticles inside the colloid are ferromagnetic.
We can describe the magnetic properties of a material in a more quantitative way through the magnetization curves, which represent the response of a material to an applied magnetic field. Some typical examples of magnetization curves are shown in figure 2.2. The magnetization curves are characterized by a *magnetic susceptibility* (χ_m) that corresponds to the tangent to the magnetization curve for a field applied near to zero and, if present, by a *saturation magnetization* (M_s) that corresponds to the maximum value of magnetization that can be reached at high B. The materials like the ferrofluids that present no hysteresis in the magnetization curve and a high χ_m, typically 10^5 times larger than normal paramagnetic materials, are called *superparamagnetic* [95].
Assuming that the particle-particle interaction is negligible, we can build a model for the superparamagnetism starting from the Langevin's classical theory [96]. The saturation magnetization of the ferrofluid can be calculated from:

$$\frac{M}{\phi M_d} = \coth\alpha - \frac{1}{\alpha} \equiv L(\alpha) \qquad \text{with} \qquad \alpha = \frac{\pi}{6}\frac{M_d B d^3}{kT} \tag{2.11}$$

where M_d is the saturation magnetization of the bulk material and ϕ is the volume fraction of solid present. For the same magnetic material, we have two ways to control the magnetic interaction: the diameter of the nanoparticles and the nanoparticle concentration. If we change the mean diameter of the nanoparticles while keeping constant the magnetic material concentration, what we obtain is to vary the value of χ_m as can be seen in the left graph of figure 2.2. If instead we change the concentration of the

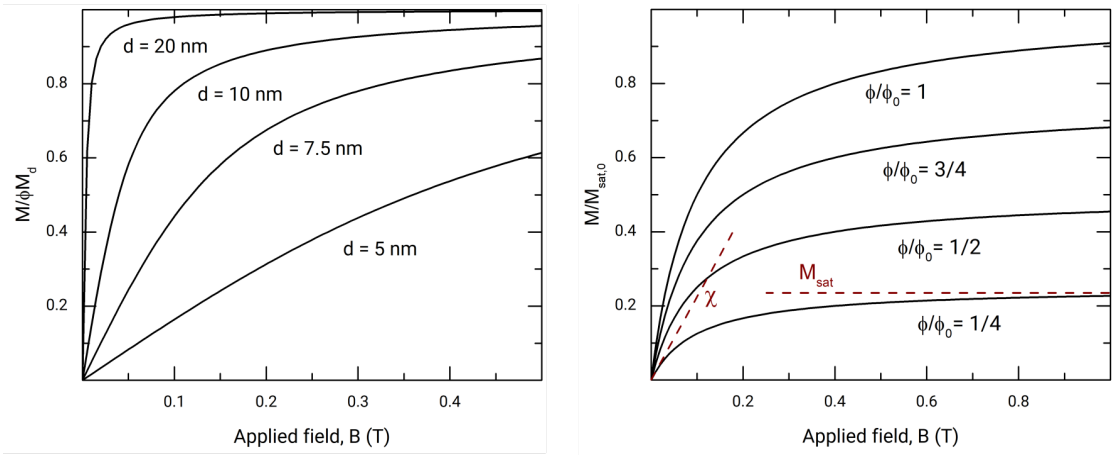

Figure 2.2 : From left to right: magnetization curves at different mean diameter of the nanoparticles, magnetization curves at different nanoparticle concentration.

nanoparticles, we vary both the value of χ_m and of M_s as can be seen in the right graph of figure 2.2. In this last scenario, if the concentration of nanoparticles is not too high (remember that this whole model needs to have negligible particle-particle interaction) the values of χ_m and of M_s change proportionally to the volume concentration ϕ.
A useful empirical formula which is commonly used to fit the magnetization curves of ferrofluids is the Frohlich-Kennelly relation [97], [98]:

$$M = \frac{M_s H}{H + M_s/\chi_m} \tag{2.12}$$

where $H = B/\mu_0$ and the free parameters are χ_m and M_s.

Now that the magnetization response to the applied magnetic field of a ferrofluid has been introduced, we can begin to describe the effects that this interaction implies. There are two main forces of interaction between a ferrofluid and a magnetic field: a bulk force due to the interaction of the dipoles of the nanoparticles with the gradient of the magnetic field and a surface force due to the difference in magnetization between the ferrofluid and the surrounding material. To describe the bulk force acting on the volume of the ferrofluid we can consider a portion of ferrofluid, with magnetization vector $\mathbf{M}$ and subjected to an applied magnetic field $\mathbf{B}$. If we consider the attraction between all the dipoles and the gradient of the magnetic field we can define the *Kelvin force density* as [34] (pag. 13):

$$\text{force density} = (\mathbf{M} \cdot \nabla)\mathbf{B} \tag{2.13}$$

In the case of a field and relative gradient only in the $\hat{x}$ direction, this force density

becomes:

$$f_m = M_x \frac{dB}{dx} \tag{2.14}$$

The ferrofluids are therefore subjected to two main bulk forces: the gravitational force and the magnetic attraction. If the magnetic attraction has the same direction of the magnetic force we can define an effective gravitational force:

$$g^* = g + \frac{M\nabla B}{\rho} \tag{2.15}$$

and an effective capillary length:

$$a^* = \sqrt{\frac{\gamma}{\rho g^*}} = \sqrt{\frac{\gamma}{\rho g + M\nabla B}} = \frac{a}{\sqrt{1 + \frac{M\nabla B}{\rho g}}} \tag{2.16}$$

which reduces to the standard capillary length a representing the characteristic size below which capillarity dominates gravity, in the absence of a magnetic field. If we want to evaluate the contribution of the bulk forces with respect to the surface tension, we can introduce a modified Bond number [99]:

$$\boxed{Bo_{g^*} = \frac{\rho g^* V^{2/3}}{\gamma}} \tag{2.17}$$

The evaluation of the surface magnetic force due to the difference of magnetic properties at the ferrofluid interface is more complex. This force is mainly due to the fact that the magnetization goes from a finite value to zero moving across the interface of the ferrofluids. Let us start from the most general case of a ferrofluid drop (1) surrounded by a fluid with no magnetization (2) and consider what occurs at the interface between the two fluids (see figure 2.3). In this case, the general form of the interfacial momentum transfer can be written as [34] (pag. 127):

$$\mathbf{n} \cdot (\mathbf{T_{m,2}} - \mathbf{T_{m,1}}) - \mathbf{n}p_c = 0 \tag{2.18}$$

where $\mathbf{n}$ is the vector normal to the surface, $\mathbf{T_{m,2}}$ and $\mathbf{T_{m,1}}$ are the magnetic stress tensor evaluated in the two fluids across the interface and p_c is the capillary pressure. At the same time we can consider a general form of the stress tensor namely:

$$\mathbf{T_m} = -(p^* + \frac{1}{2}\mu_0 H^2)\mathbf{I} + \mathbf{BH} \tag{2.19}$$

where p^* is the internal pressure of the fluid considering also the contribution of the magnetic bulk interaction and $\mathbf{I}$ is the identity matrix. If now we apply the boundary conditions for the continuity of the magnetic fields at the interface (normal component of $\mathbf{B}$ continuous at the interface and tangential component of $\mathbf{H}$ continuous at the interface) we find that the change in magnetization across the interface generates a *magnetic normal traction* defined by:

$$p_n \equiv \frac{\mu_0 M_n^2}{2} \tag{2.20}$$

where M_n is the component of the magnetization normal to the surface. Considering this last contribution the pressure balance at the surface can be written as:

$$p^* + p_n = p_0 + p_c \tag{2.21}$$

where p^* is the same as defined before and p_0 is the external pressure. As we can see in figure 2.3, in the case of a ferrofluid droplet the value of M_n varies a lot along the surface. A clear consequence of this fact is that the traction pressure is higher at the tip of the droplet than at the base, generating a net upward force that elongates the droplet.
Also in this case we can express this contribution in terms of a dimensionless number, the so called traction number S [34, 100]:

$$\boxed{S = \frac{\mu_0 M^2 V^{1/3}}{\gamma}} \tag{2.22}$$

which compares the pressure jump at the ferrofluid interface due to magnetization with the capillary pressure.
As we will see, the modified Bond number Bo_g^* and the traction number S are useful parameters to describe the phenomenology of the deformations on the ferrofluid volumes and their topological instabilities.

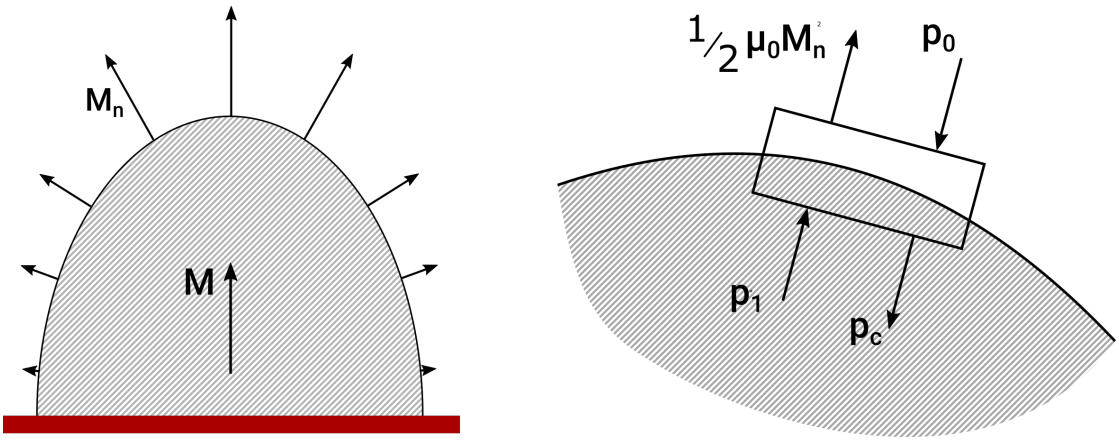

Figure 2.3 : From left to right: schematic representation of the different values of M_n along the profile of a droplet, schematic representation of the pressure balance at the surface of a ferrofluid.

§ 2.4. Topological instabilities

The topological instabilities of the ferrofluids are maybe one of their most characteristic features. There are two main topological instabilities: the normal field or Rosensweig instability [36] and the labyrinthine instability [101] (see fig. 2.4).
In the normal-field instability, a perpendicular and uniform magnetic field applied to a pool of ferrofluid produces the generation of a pattern of surface protuberances with the form of spikes if a critical magnetic field is reached. The generation of spikes is due to the difference in magnetization between the ferrofluid and the surrounding material. To understand the mechanism of generation of this instability let us consider an infinite flat surface of ferrofluid. The surface will experience the generation of capillary waves as a perturbation of the flat surface due to the interplay between the gravitational force and the surface tension.
When the capillary waves are generated in the ferrofluid, the magnetic field lines are focused at the ridges lowering locally the magnetic energy (see fig. 2.5). At the same time on the ridges the traction pressure is stronger than at the base as explained in section 2.3. These effects however are opposed by the action of the gravity that tries to restore the initial flat surface.
It can be shown [34] (pag. 178) that the surface waves satisfy the following dispersion relation:

$$\omega^2 = gk + \gamma k^3 - \frac{k^2 \mu_0 M_0^2}{1 + \mu_0/\mu} \tag{2.23}$$

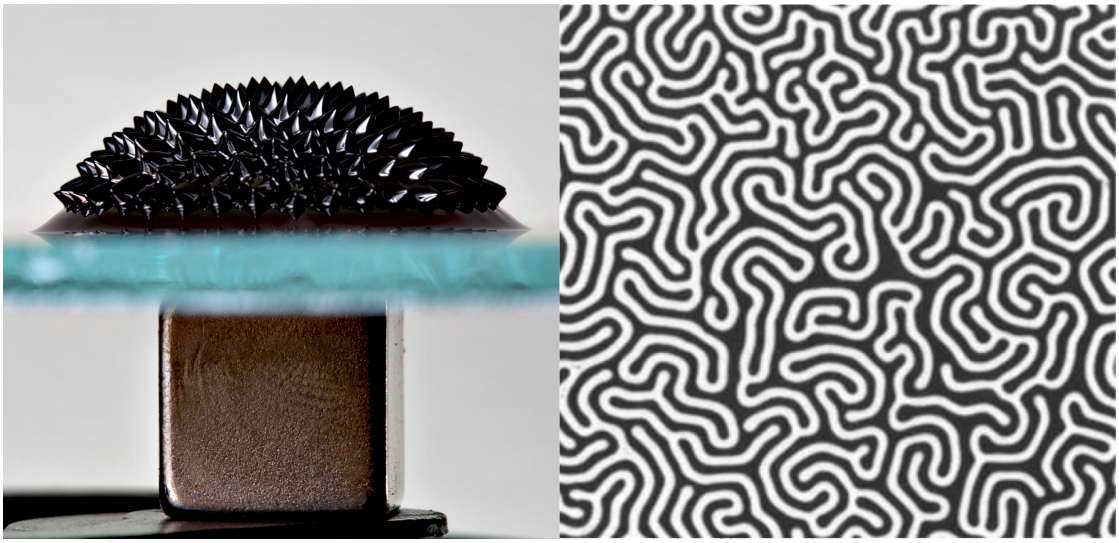

Figure 2.4 : From left to right: normal field instability generated at the free interface of a ferrofluid, labyrinthine instability caused on a confined ferrofluid by the magnetic field (the ferrofluid in black is surrounded by a non magnetic fluid in white) [101].

The three terms are, respectively, the gravity waves ($\omega^2 = gk$), the capillary waves ($\omega^2 = \sigma k^3$) and a quadratic magnetic term. As the magnetic field is increased, the quadratic term becomes dominant until a transition from a stable to an unstable state is reached characterized by:

$$\omega^2 = 0 \qquad \text{and} \qquad \delta\omega^2/\delta k = 0 \tag{2.24}$$

At this transition, ω changes from real to imaginary. In this situation we can identify two critical values:

$$k_c = (\rho g/\gamma)^{1/2} \tag{2.25}$$

$$M_c^2 = \frac{2}{\mu_0}\left(1 + \frac{\mu_0}{\mu}\right)(\rho g \gamma)^{1/2} \tag{2.26}$$

The two quantities are clearly linked between each other and indicate the conditions over which the normal field instability occurs. In particular, equation 2.25 indicates the periodicity of the ridges and equation 2.26 indicates the lowest value of magnetization

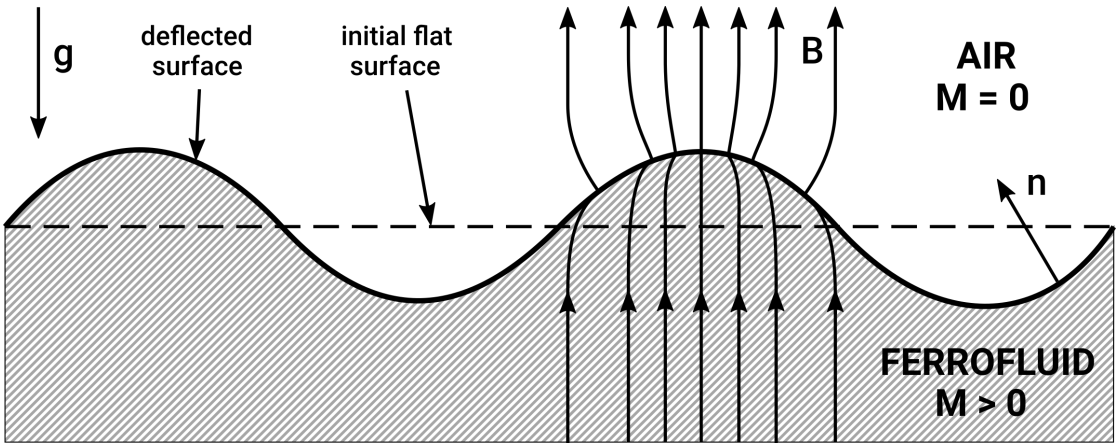

Figure 2.5 : Schematic representation of the onset of the normal field instability.

at which the phenomenon is observed. The presence of a magnetic field gradient [102]:

$$M_c^2 = \frac{2}{\mu_0}\left(1 + \frac{\mu_0}{\mu}\right)(\rho g^* \gamma)^{1/2} \tag{2.27}$$

where g^* is the effective gravitational acceleration defined in equation 2.15. We point out that can be made is that we can re-write eq. 2.31 using equations 2.17 and 2.22 as:

$$S_c = \alpha (Bo_{g^*})^{1/2} \tag{2.28}$$

Showing that the normal field instability is linked with the balance between the two forces of interaction acting on the ferrofluids described in section 2.3.

§ 2.5. Magnetoviscous effect

First described in 1969 [103], the variation of the viscosity of the ferrofluids as a function of the magnetic field has been widely studied for its useful applications in the mechanical industry [104] [105]. To describe this effects, we will follow the reasoning in [38]. First of all, let us consider the viscosity of the ferrofluids in the absence of a magnetic field. In the case of low concentrated, non-interacting rigid nanoparticles, the Einstein model states that:

$$\eta_0 = \eta_c \left(1 + \frac{5}{2}\phi\right) \tag{2.29}$$

where η_0 is the viscosity at zero field of the ferrofluid, η_c is the viscosity of the carrier fluid and ϕ is the volumetric fraction of the nanoparticles. If we want to describe more

concentrated dispersions, the viscosity is better accounted for by the Batchelor's model:

$$\eta_0 = \eta_c \left(1 + \frac{5}{2}\phi + b\phi^2\right) \tag{2.30}$$

where the parameter b is usually taken equal to 6.2 [38].
These models do not take into account the fact that at a certain volumetric fraction the viscosity should diverge. This increase at high concentrations can be described by [34]:

$$\eta_0 = \eta_c \left(1 - \frac{5}{2}\phi + \left(\frac{5}{2}\phi_c - 1\right)\left(\frac{\phi}{\phi_c}\right)^2\right)^{-1} \tag{2.31}$$

where ϕ_c is a critical value of the volumetric fraction.
In the case of ferrofluids, the Einstein model works well for values of ϕ up to 0.05, the Batchelor model works for values of ϕ up to 0.2 and the Rosensweig model works for values of ϕ up to 0.3 (see graph in figure 2.6 for a comparison between the three models). For ϕ greater than 0.3 a more complex analysis is needed that takes into account the interaction between the particles and the formation of clusters.
Let us now consider the case of a ferrofluid subjected to a magnetic field. In this case it is experimentally observed that an increase in the magnetic field from 0 to 0.01 T corresponds to an increase of the viscosity of the fluid of more than ten times [38]. Applying a magnetic field a tendency for the magnetic moments of the particles to orientate towards the field direction is expected [106]. On the other hand, due to the viscous friction in the shear flow, a mechanical torque will act on each particle and will rotate it. Thus, the free rotation of the particles in the flow is hindered and an increase in the viscosity of the fluid is observed. This explanation for the magnetoviscous effect applies only for large particles (diameter of about 13 nm for magnetite [39]) following the Brownian relaxation process of magnetization and thus having the magnetic moments fixed within. Thus, for commercial ferrofluids containing magnetite particles with a mean diameter of about 10 nm only, very weak magnetoviscous effects would be expected. On the contrary experiments using a specialized rheometer for magnetic fluids find that commercial ferrofluids show a strong magnetoviscous effect, which can only be explained by the formation of magnetic structures built up by numerous particles [39]. For the formation of clusters, the dipole-dipole energy of the particles has to overcome the thermal energy:

$$\frac{\text{thermal energy}}{\text{magnetic energy}} = \frac{kT}{MBV} > 1 \tag{2.32}$$

Since the dipole-dipole energy increases with the size of the particles, only 'large' particles can form structures (for magnetite-based ferrofluids the particles must have diameters larger than about 12 nm). Accordingly ferrofluids can be described, at a first approximation, as a bidisperse system containing a large fraction of small particles not contributing to magnetoviscosity and a small fraction of relatively large particles able to form agglomerates [39].
The enhancement of the magnetovisous effect can be achieved in two ways: changing the size of the nanoparticles or changing the nature of the nanoparticles using a material with a stronger magnetic interaction. Increasing the size of the nanoparticles have several collateral effects like introducing the precipitation of the nanoparticles due to gravity. Changing the material of the nanoparticle is usually the best option, because it promotes cluster formation at relative small size of the nanoparticles.
The increase of the viscosity is greater at low shear rates. As the shear rate is increased, the clusters are broken by the flow and the viscosity decreases [107]. In other words ferrofluids exhibit shear-thinning behavior. Furthermore the clusters particles are random at field equal to zero and they elongate in chains if the magnetic field is turned on (see fig.2.6). The fact that the nanoparticles are disposed in ordered chains along the magnetic field direction implies that the viscosity along the magnetic field is different from the one in the perpendicular direction [34].
One of the most complete studies on the magnetoviscous effect as a function of the size, nature of the nanoparticle and applied magnetic field has been performed in [106]. In particular, the internal structure of the ferrofluid has been studied using SANS (small angle neutron scattering).

§ 2.6. Synthesis and characterization

Understanding the techniques of synthesis of the ferrofluids is very useful to understand how it is possible to determine the shape and size of the ferrofluid's nanoparticles. The most effective way to synthetize a ferrofluid suspension is described in [108]. The Massart method consists of a coprecipitation technique: an aqueous mixture of ferric chloride and ferrous chloride is added to ammonia solution, then the gelatinous precipitate is isolated from the solution by centrifugation or magnetic decantation without washing with water. Finally, the precipitate is dispersed in alkaline or acidic solution. This simple technique allows to obtain polidispersed rock shape nanoparticles of maghemite. The mean size of the nanoparticle depends on the kinetics of the precipitation reaction. To obtain a

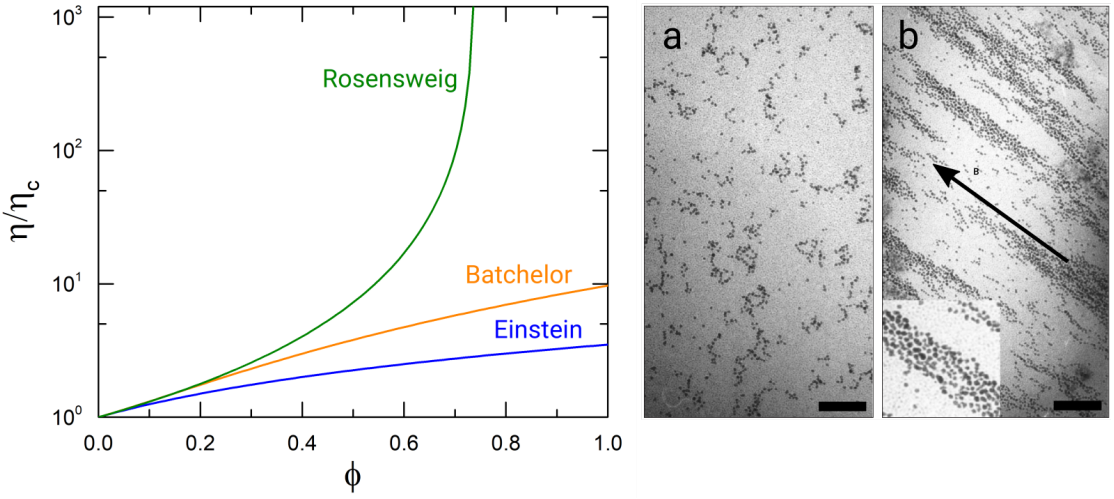

Figure 2.6 : Left graph: comparison between the three models for the viscosity of a colloidal solution in function of the volumic fraction. Figures a and b: cryogenic electron microscopy of ferrofluid nanoparticles in the case of zero field applied (a) and in the case of a magnetic field applied (b) [32].

monodisperse ferrofluid, Lefebure et al. [109] proposed a size sorting procedure based on the addition of alkaline or acidic solution to the ferrofluid and the subsequent increase of the magnetic field to obtain the precipitation of the biggest nanoparticles. In this way the nanoparticles can be separated by size taking advantage of the stability properties of the ferrofluid itself. The procedure to obtain nanoparticle of different materials like the cobalt ferrite is practically the same.
To characterize the ferrofluid properties there are different techniques depending on the properties that we want to study. Following is reported a list which associates the most used techniques to the respecively studied properties:

- Magnetization curve: VSM (vibrating sample magnetometer) [110]
- Size of the nanoparticles: direct measure with TEM [111] or indirect measure from the magnetization curve
- Volumetric fraction: indirect measure from the magnetization curve
- Iron concentration: atomic absorption.

Part II

Experimental activity

Chapter 3

Methods

In this chapter we will present the experimental techniques and methods used for the experimental activity in this thesis. In particular first the characteristics of the ferrofluids will be presented in section 3.1, then the characteristics of the magnets in section 3.2, after that the the optical setup in section 3.3 and, in the end, the preparation of the different substrate in section 3.4.

§ 3.1. Ferrofluids characteristics

The ferrofluids used in this work are stable aqueous suspensions of maghemite ($\gamma - Fe_2O_3$) nanoparticles (ferrofluid code: FFD64). They are synthesized according to the Massart process [108] with the following procedure: ammonium hydroxide (1 L, 20% from VWR) is added to a mixture of ferric and ferrous chlorides (0.9 and 1.8 mol, respectively) to obtain magnetite nanoparticles that are oxidized to maghemite by adding an iron nitrate solution (800 mL, 1.3 mol) and heating at 80 ° C for 30 min followed by washing and suspension in a nitric acid solution (360 mL, 2 mol/L). These nanoparticles are positively charged with NO_3^- as counter ions. To obtain a higher iron concentration of the ferrofluid, the aqueous suspension is dialyzed (spectra pore membrane MWCO (daltons): 12 000) in a bath (1 L) against nitric acid solution (0.1% wt) containing polyethylene glycol (PEG, MW 35 000; 7% wt). After dialysis, the final concentration of iron as obtained from atomic absorption measurements is 7.5 mol/L and the volumic fraction of the nanoparticles is $\phi = 11.75\%$ so for our ferrofluid is valid the relationship: $\phi\ [\%] = 1.566 \cdot c\ [\text{mol/L}]$. The nanoparticles have a rock shape with a mean diameter of about 8.5 nm, as determined from transmission electron microscopy (see top right panel of fig. 3.1). In figure 3.1 top left graph the magnetization curve of the ferrofluid obtained with a custom made VSM (vibrating sample magnetometer) is presented: the

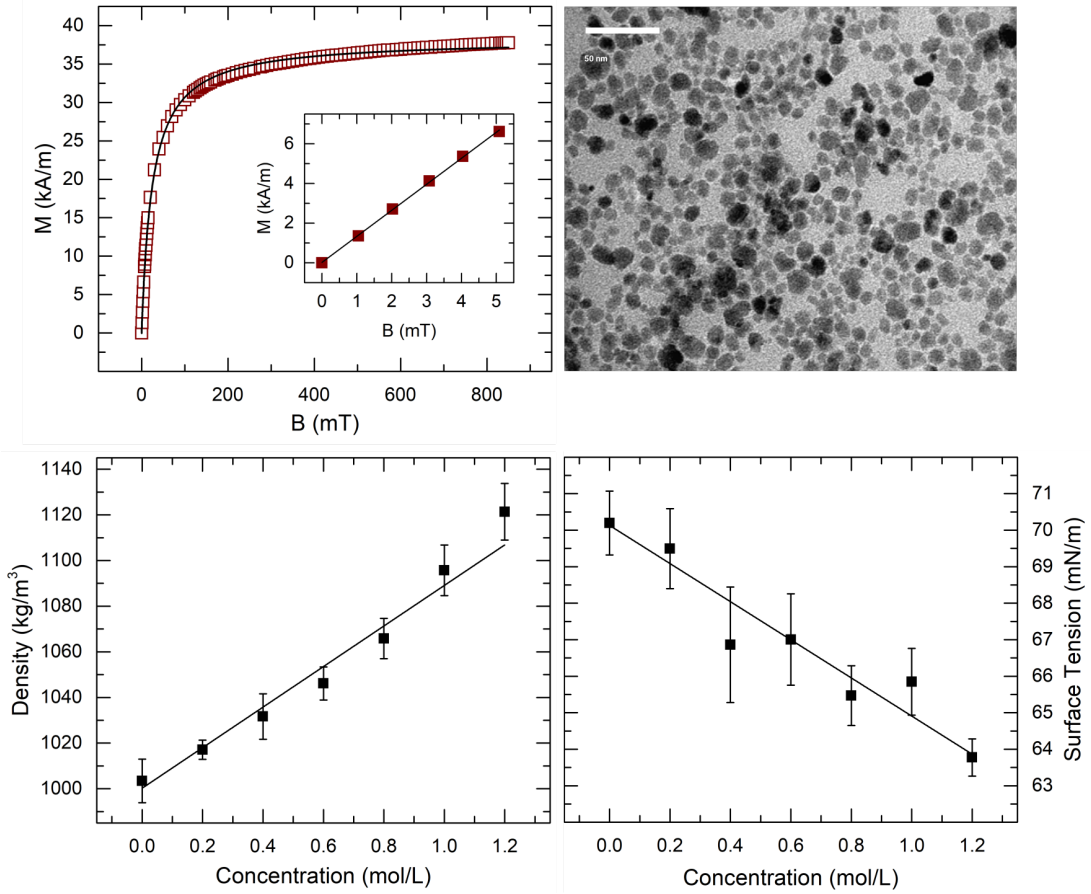

Figure 3.1 : Top Left: magnetization curve of the ferrofluid used in this research (inset: zoom of the same data at low magnetic field applied); Top Right: TEM image of the nanoparticles inside of the ferrofluid; Bottom Left: graph of the variation of the density in function of the iron concentration; Bottom Right: graph of the variation of the surface tension in function of the iron concentration.

value of the magnetic susceptibility is $\chi_m = 1.55 \pm 0.01$ and the value of the magnetic saturation is $M_{sat} = 38.22 \pm 0.05$ kA/m. Also for this ferrofluid the rule expressed in section 2.3 for the proportionality of χ_m and M_{sat} with the ferrofluid concentration is valid.

The presence of the nanoparticles inside the ferrofluids modifies other properties of the fluid in addiction to the magnetic ones. In the bottom part of figure 3.1 the changes in density and surface tension increasing the concentration are described. The density of the ferrofluid increases as expected while surface tension decrease increasing the iron concentration.

The density enhancement is due to the simple fact that the nanoparticles are heavier

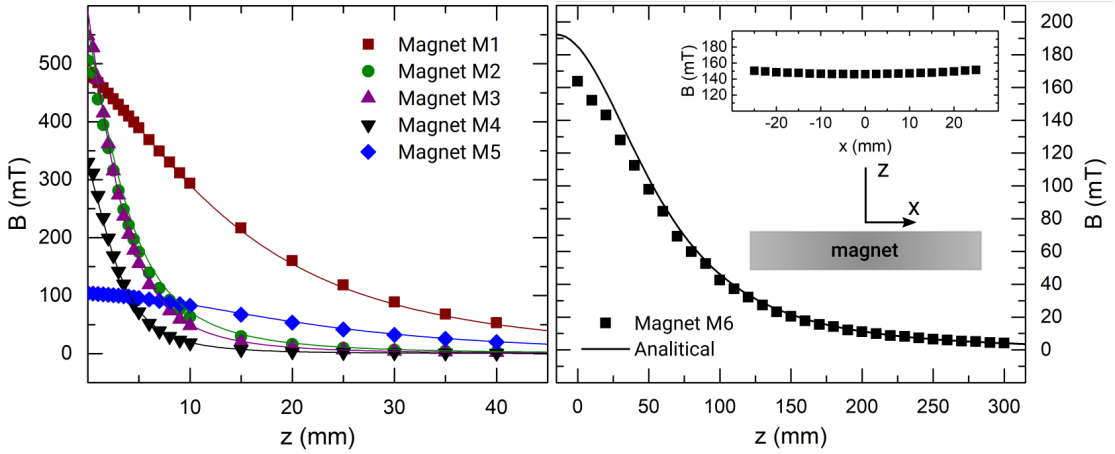

Figure 3.2 : Left: profile of the magnetic field along the magnet axis in function of the distance from the surface of the small and medium magnets (the continuous line represent the data calculated from the analytical formula for each magnet). Right: profile of the magnetic field along the magnet axis in function of the distance from the surface of the biggest magnet and in inset the profile of the magnetic field parallel to the axis in function of the distance from the center.

than the solvent and so adding nanoparticles the total density increases. In our case the value of density as a function of the concentration is $\rho = 1000.2 + 88.9 \cdot c$.
The trend of the surface tension instead is not immediate to explain [112]. In our case the decrease is about the 10% in the range studied, this variation has an influence on the contact angle value with a theoretical change of about 3% (calculated from the Young equation 1.9) that is lower than the experimental error on the measure of the contact angle (see section 3.3.1 for a better explanation on the measure of the contact angle).

§ 3.2. Magnets

In this section, the characteristics of the magnets used for the research activity will be presented. For the various studies, six different permanent magnets and one electromagnet have been used. In the following subsections the magnetic properties of each will be described.

§ 3.2.1. Permanent magnets

All the permanent magnets used in this study are Neodymium Iron Boron (NdFeB) magnets. This kind of magnets, which are the strongest magnets in commerce, manage to reach high magnetic fields (up to 0.5 T) and very high gradients of magnetic fields

Magnet	t (mm)	D (mm)	Type	$B_r(T)$	B_{max}
M1	30.0 ± 0.1	45.0 ± 0.1	N40	1.25	0.48 ± 0.5
M2	20.0 ± 0.1	12.0 ± 0.1	N35	1.17	0.50 ± 0.5
M3	10.0 ± 0.1	10.0 ± 0.1	N45	1.32	0.55 ± 0.5
M4	3.0 ± 0.1	9.0 ± 0.1	N35	1.17	0.33 ± 0.5
M5	5.0 ± 0.1	60.0 ± 0.1	N42	1.29	0.10 ± 0.5
M6	30.0 ± 0.1	180.0 ± 0.1	N35	1.17	0.19 ± 0.5

Table 3.1: Characteristics of the different permanent magnet used in this thesis. Magnet: code associated at each permanent magnet; t (mm): thickness/height of the permanent magnet; D (mm): permanent magnet diameter; Type: grade of neodymium of the magnets; $B_r(T)$: residual magnetic field; B_{max}: maximum magnetic field measured.

(up to 100 T/m). The characteristics of the six different magnets used in our studies are listed in table 3.1.

Figure 3.2 shows the measured magnetic field along the magnet axis as a function of the distance d from the magnet. The various measurements taken with a Hall probe (LakeShore 460 3-Channel Gaussmeter with a 3-axis probe) moved with a micrometer translator. As it can be seen, the magnetic field decreases faster for the magnets with a small diameter and much slower for those with a large diameter magnets. The profile of the magnetic field along the axis can be calculated from the following analytical formula [113]:

$$B_z(z) = \frac{B_r}{2}\left(\frac{t+z}{\sqrt{\left(\frac{d}{2}\right)^2+(t+z)^2}} - \frac{z}{\sqrt{\left(\frac{d}{2}\right)^2+z^2}}\right) \tag{3.1}$$

As it can be seen in fig. 3.2, the agreement between the measured data and the analytical formula is very good.

§ 3.2.2. Electromagnet

The right part of figure 3.3 shows a schematic representation of the electromagnet used in our studies. The electromagnet is composed by two coaxial coils with an AmCo Iron core. The distance between the poles (L) can be regulated. The graph in figure 3.3 shows the values of the magnetic field along the axis as a function of the applied current with separation between the expansions of L = 4 cm. In the center of the electromagnet the field is almost uniform and the gradients are very low (under 1 T/m). This electromagnet

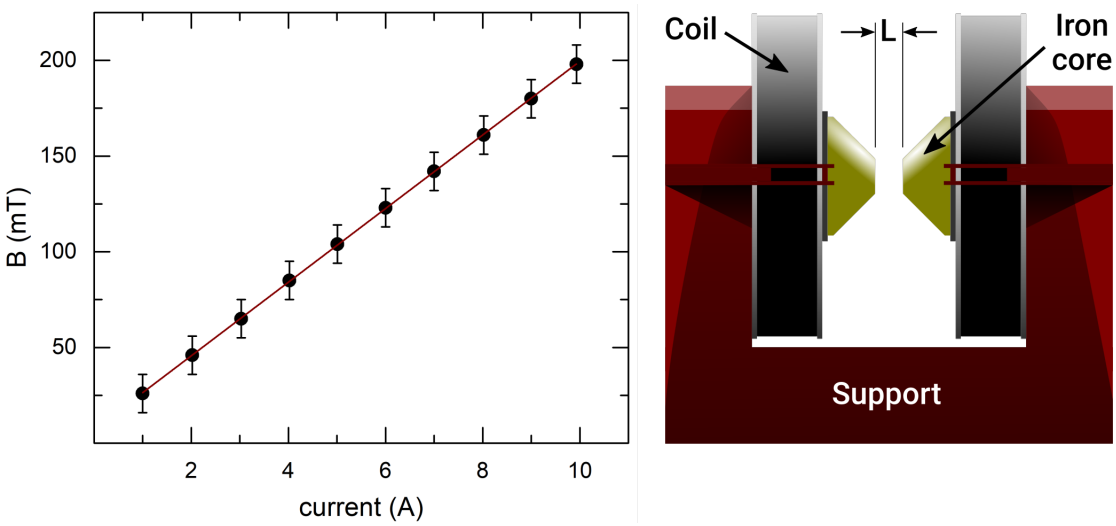

Figure 3.3 : Left: graph of the magnetic field along the axis measured at the center of the electromagnet in function of the current applied to the coils. Right: schematic representation of the electromagnet used for the experiments.

has been used for preliminary measurements on the motion of ferrofluid droplets on inclined planes [114]

§ 3.3. Optical set up and image analysis

Two different main optical setups have been used which will be described in the following subsections.

§ 3.3.1. Contact angle setup

Figure 3.4 shows the top and side views of the contact angle apparatus. It has been used to perform the experiments described in Chapters 4.3 and 6.3. The droplets deposited on the substrate are illuminated by a backlight-collimated LED, and their profile is viewed using a CCD video camera (Manta G-146, Allied Vision Technologies) mounting a telecentric lens (2X magnification).The two cameras can acquire single images, for the evaluation of the static contact angle, or sequences of images working up to 17 fps, to measure the advancing or receding contact angles by progressively increasing or reducing the droplet volume. An automatic actuator varies the distance of the permanent magnets from the bottom of the substrate slide in a controlled way (less than 0.1 mm of error on the value of the distance z). The acquired images are analyzed through a custom-made program, written in LabVIEW 2013. The program uploads a stack of images and allows

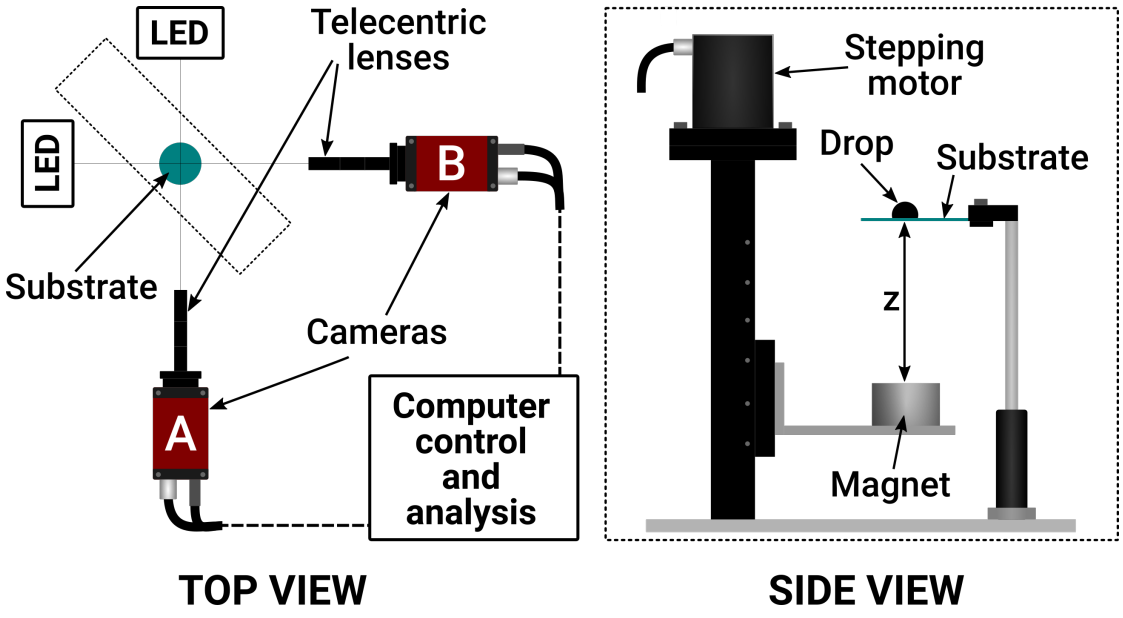

Figure 3.4 : Left: top view of the apparatus for the measure of the contact angle. The dotted area is occupied by a z-stage and a sample holder. Right: side view of a part of the contact angle setup in particular a schematic representation of the the motorized z-stage and the sample holder.

the user to fix a ROI (Region Of Interested) and to regulate contrast, illumination and saturation. Once selected, the correct ROI the program takes advantage of the contrast between the droplets and the white background to individuate the drop profile and to perform a polynomial fit to individuate the key parameters of the profile, namely the apparent contact angle, the height and the lateral extension of the contact line of the ferrofluid drops.

§ 3.3.2. Sliding setup

Figure 3.5 shows the axial and frontal view of the sliding setup, which has been used to perform the experiment described in Chapter 5.3. The magnet M6 is mounted inside an aluminum box fixed to a rotating structure, whose inclination angle can be controlled by a stepping motor. The droplet sliding on the substrate is illuminated by a backlight LED, and the video of the motion is collected by a fast camera (Phantom v7.3 Vision Research) able to reach up to 2k fps mounting a macro objective (Navitar 7000). The acquired images and videos are analyzed off-line using a custom-made program (always written in LabVIEW 2013) that calculates the apparent front and rear contact angles, and the front and rear position over time.

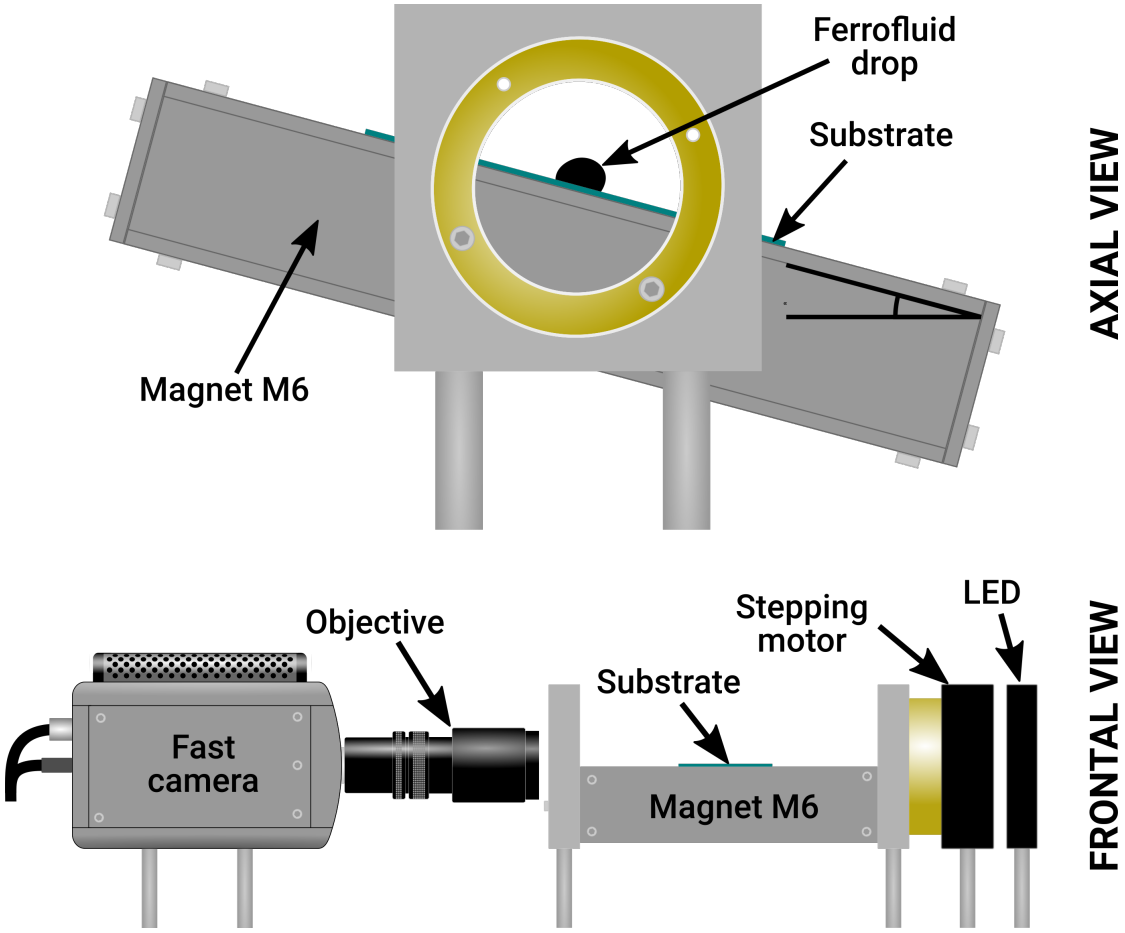

Figure 3.5 : Top: axial view of the sliding apparatus. Bottom: frontal view of the sliding apparatus.

§ 3.4. Substrates

Several different substrates have been prepared for the different experiments performed in this thesis. The different wetting characteristics of the substrates are summarized in table 3.2.

	θ_c (CA)	$\Delta\theta_c$ (CAH)
Glass	60	5
Noa	70	30
PDMS	105	30
Teflon	115	30
Lotus	155	5
LIS	100	< 5

Table 3.2: Contact angle θ_c and contact angle hysteresis $\Delta\theta_c$ of the different substrates used in this thesis.

The following list reports the details of production techniques to obtain the different substrates.

- Glass: this substrate is a simple glass slide cleaned with distilled water, ethanol and acetone.
- NOA: this substrate is produced with a glass slide coated by a thiolenic adhesive (NOA 81 by Norland Products Inc., USA). First, the adhesive is spread on the glass slide through spin-coating. It is then exposed to UV light to obtain the polymerization.
- PDMS: this substrate is produced coating a glass slide with a layer of polydimethylsiloxane (PDMS) which is an hydrophobic silicon based polymer. To prepare the PDMS, ten parts of a vinyl PDMS prepolymer (VDT-731, Gelest Corp., www.gelest.com) are mixed with one part of a Pt catalyst (platinum divinyltetramethyldisiloxane, SIP6831.1, Gelest Corp.). The prepared PDMS is spin-coated on a glass slide to obtain a uniform layer and then the sample is exposed to 80° for 30-40 minutes to allow the catalyst to perform the reticulation of the polymer.
- Teflon: this substrate is a simple commercial teflon tape used for hydraulic applications.
- Lotus: a flat portion of a fresh Lotus leaf is attached to a glass slide.

- LIS: this Liquid Impregnated Surface is obtained following the recipe described in [72]. In brief: after cleaning a glass slide with acetone, some liquid silicone oil (viscosity 5 cSt) is spread on the glass substrate and then is baked at 300 ° for 1-3 minutes. This produces a thin porous silicone layer attached to the glass slide (around 3 nm of thickness). After the sample is back at room temperature, the substrate is cleaned with acetone a second time. After waiting for the evaporation of the residual acetone left on the substrate, the sample is ready to be impregnated. The impregnation phase is quite simple: a small amount of silicone oil of the desired viscosity is spread on the silicone-coated glass slide. The sample is then left for around 20 minutes in vertical position to eliminate the residual silicon oil. After 20 minutes, the substrate is ready to be used.
  The resulting substrates have been characterized by performing static and dynamic tests using drops of distilled water and infusing the solid spongy matrix with three silicone oils of different viscosities (5, 100, and 1000 cSt respectively). Regardless of the viscosity, we have measured a value of contact angle of sessile water drops equal to 107 ± 2°, and a value of contact angle hysteresis around a few degrees (3.1 ± 0.5°). Furthermore, the downward velocity of water drops of volume $\Omega = 20\mu L$ has been measured at different inclination angles α and oil viscosity scales as expected (see figure 3.6). The left graph of fig. 3.6 shows the droplet speed as a function of the inclination angle. A characteristic parabolic profile can be observed with increasing velocity for decreasing oil viscosity. The right graph displays the same data plotted in terms of the eq. (15) in [14]:

$$Bo(\sin\alpha - \sin\alpha^*)f(\theta) = Ca\frac{\mu_o}{\mu_w} \tag{3.2}$$

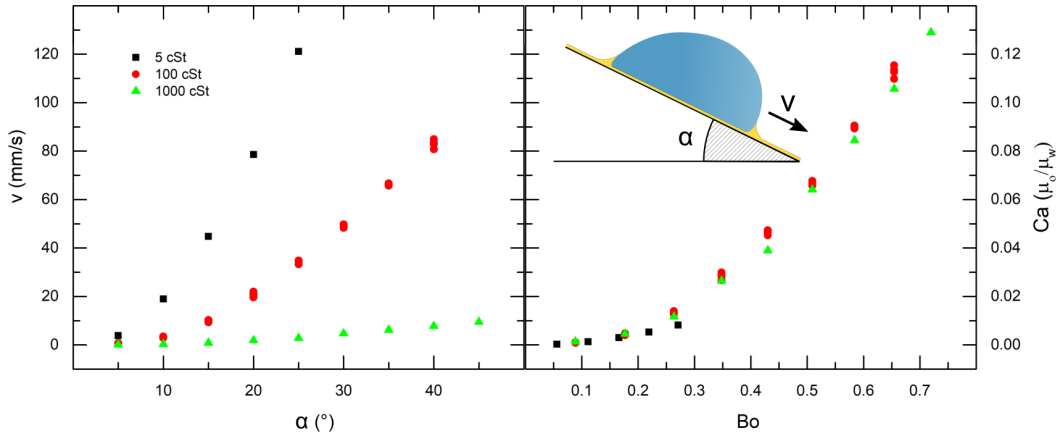

Figure 3.6 : Left: mean velocity v of water droplets of volume $\Omega = 20\mu L$ deposited on oil impregnated surfaces tilted by an increasing inclination angle α. Three silicone oils of different viscosity have been used: 5, 100 and 1000 cSt. Right: the same data plotted in terms of the capillary and scaled Bond numbers as done in [14].

Chapter 4

Magnetowetting

In this chapter we will present the research activity about the study of the wetting properties of sessile drops of water-based ferrofluid. To characterize completely the magnetowetting we have changed the iron concentration of the ferrofluids, the substrates on which the droplets where deposited on and the magnetic field applied using permanent magnets of different sizes and strengths. The research activity summarized in this chapter has been also published in Langmuir [52].
After a brief introduction in section 4.1 the experimental results in section 4.2 will be presented: a rich phenomenology is observed, ranging from flattened drops caused by the magnetic attraction to drops extended normally to the substrate because of the normal traction of the magnetic field. We find that the former effect can be conveniently described in terms of the effective Bond number that compares the effective drop attraction with the capillary force, whereas the drop vertical elongation is effectively expressed by the dimensionless traction number S, which compares the pressure jump at the ferrofluid interface because of the magnetization with the capillary pressure. In the end, in section 4.3, some conclusions and future perspective of this work willl be presented.

§ 4.1. Introduction

As we said at the beginning of the thesis, a good understanding of the sliding of ferrofluid drops requires prior knowledge about their static wetting properties under an external magnetic field. For the case of a water-based ferrofluid drop surrounded by immiscible mineral oil is found that the droplet is stretched by a uniform magnetic field parallel to the field lines [115]. In the case of a droplet on a flat surface instead a stronger magnetic field is found to pull down and laterally stretch the ferrofluid droplet, increasing its base diameter and decreasing its height and its apparent contact angle, with all variations

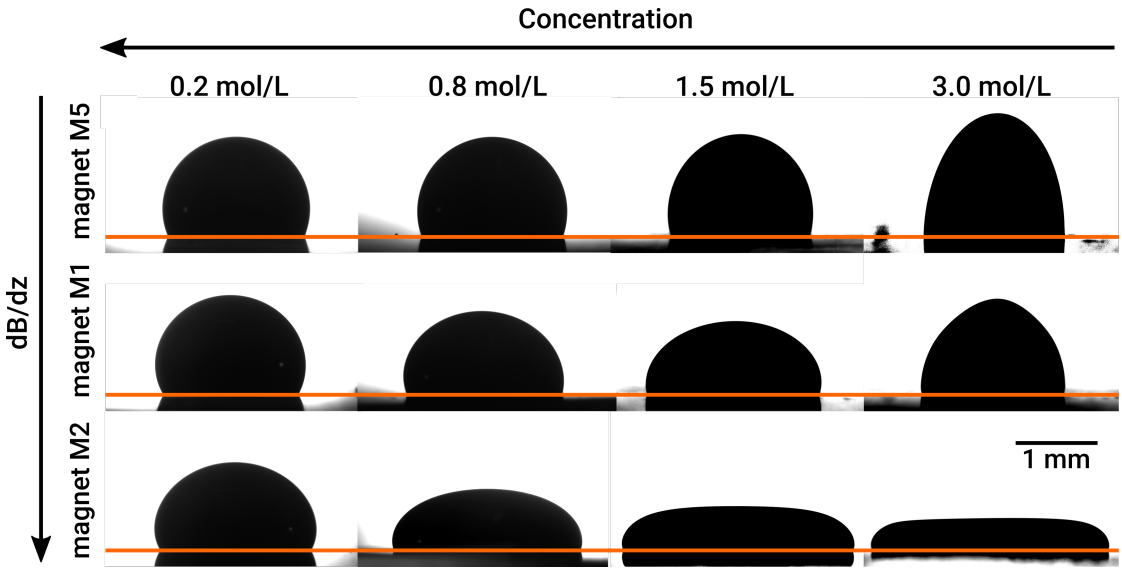

Figure 4.1 : Summary of the different cases observed in the magnetowetting: from left to right snapshots of droplets at increasing iron concentration, from top to bottom snapshots of droplets subjected at increasing gradient of magnetic field.

being linear [49]. The study of the shape of liquid oxygen drops subject to the magnetic field of a permanent magnet, whose distance from the substrate is varied, confirms the flattening of the drop, which can be accounted for by the modification of the capillary length because of the magnetic force [116].
We have consequently decided to systematically explore the magnetowetting effect by measuring the morphology of ferrofluid drops subjected to the action of five different permanent magnets. By varying the magnets and their distance to the surface, it is possible to change both the amplitude and the gradient of the magnetic field. Magnetic forces several times the gravitational one and magnetic gradients up to 100 T/m can be achieved. In this way, we can observe flattened drops caused by the magnetic attraction to drops extended normally to the substrate because of the polarizing effect of the magnetic field.

§ 4.2. Results and discussion

The ferrofluid used for the experiments described in this chapter is the one described in 3.1. In particular seven dilutions have been studied: F1 = 0.2 mol/L, $\chi_{F1} = 0.042$; F2 = 0.4 mol/L, $\chi_{F2} = 0.144$; F3 = 0.8 mol/L, $\chi_{F3} = 0.144$; F4 = 1.5 mol/L, $\chi_{F4} = 0.28$; F5 = 2.0 mol/L, $\chi_{F5} = 0.35$; F6 = 3.0 mol/L, $\chi_{F6} = 0.57$; and F7 = 4.0 mol/L, $\chi_{F7} =$

0.74.
The five magnets used are the ones described in section 3.2 and the optical setup is the one customized for the measure of the contact angle described in 3.3.1. The droplets have been deposited on three different substrates: one hydrophilic of NOA, one hydrophobic of PDMS and one superhydrophobic similar to a lotus leaf (see 3.4 for a better explanation of the characteristics and the production techniques). Figure 4.1 summarizes the overall phenomenology observed for the magnetowetting of ferrofluid drops deposited on a PDMS surface. All of the drops have the same volume V = 2.5 μL but different molar concentrations and are placed at a distance of 1 mm from three different magnets (M1, M2, M5). For each concentration, increasing the gradient of the magnetic field causes a flattening of the drop. A progressive flattening of the drop is also observed as the concentration of the drop is increased in the presence of magnet M2 but only at low concentration. In the case of the middle sequence observed with magnet M1 and, above all, the top one with magnet M5 show an opposite trend: increasing the concentration and therefore the magnetization produce an elongation of the drop profile along the field direction, which assumes the shape of a cusp, as recently observed in a recent experiment on the self-assembly of ferrofluid drops [37]. Before describing in detail the various cases that we will show to be the result of a rich interplay between the strength of the magnetic field and its gradient is necessary to verify that the phenomena we observe are compatible with the theory we described in section 2.3.
Remembering that the magnetic force exerted by a magnet per unit volume is:

$$f_m = M(B)\nabla B \tag{4.1}$$

where $M(B)$ is the magnetization of the ferrofluid and ∇B is the gradient of the magnetic field.

Figure 4.2 (left) shows the calculated values of the ratio between the magnetic force per unit volume and the gravitational force per unit volume in function of the distance of the magnet and for two values of iron concentration. Far from the magnets (z $>$ 30 mm), the magnetic force is negligible compared to the volumic weight. For z $\approx$ 20 mm, these two forces are on the same order for most of the combinations magnet/solution, and the ratio $f_m/\rho g$ can go up to 80 at 1 mm from the magnet M2 for the solution 1.5 mol/L.
Always remembering the reasoning carried on in section 2.3 if the magnetic force acts in the same direction as gravity, one can define a modified capillary length λ^* corresponding

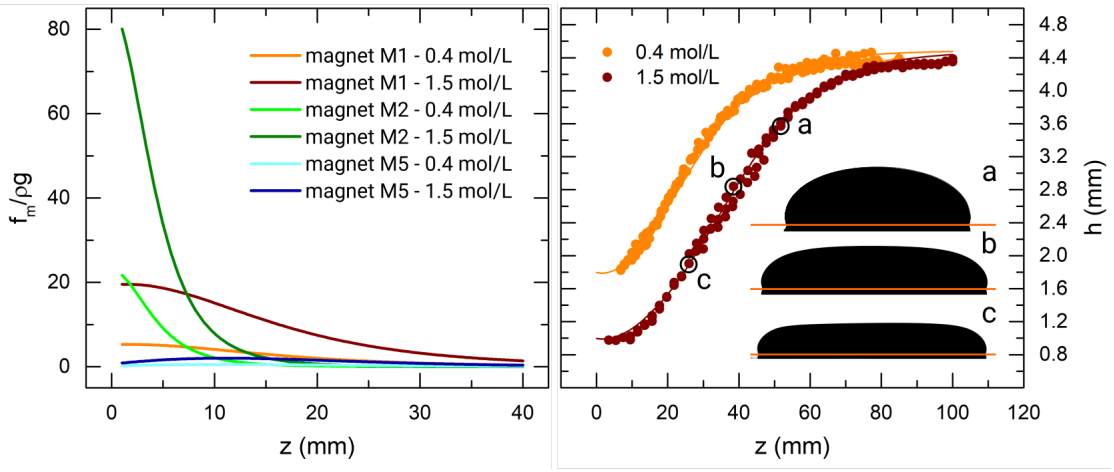

Figure 4.2 : Left: Modulus of the magnetic force per unit volume f_m, normalized by the volumic weight of the drop ρg, as a function of the distance z between the top face of the magnet and the bottom of the drop. The curves refer to three different magnets and two different ferrofluidic solutions concentrations as indicated in the caption; right: variation of the thickness h of ferrofluid puddles of two different molar concentrations deposited on a PDMS surface as the distance z from the top face of magnet M1 is varied. The continuous lines are twice the values derived from eq 4.2.

to an effective gravitational acceleration g^* [116]:

$$\lambda^* = \sqrt{\frac{\gamma}{\rho g + M\nabla B}} = \frac{\lambda}{\sqrt{1 + \dfrac{M\nabla B}{\rho g}}} \tag{4.2}$$

where γ is the ferrofluid surface tension. Its value, measured with a Kruss K10T ring tensiometer, is 71.4 mN/m at 20 °C. It is very close to the surface tension of pure water (73.2 mN/m), in agreement with the fact that our ionic ferrofluid is free of surfactants. Now remembering that in the case of big volumes ($> 80\mu$L) the shape of the drop is that of a puddle which height h has the following particular relationship with the capillary length (see section 1.3.2 for further details):

$$h = 2\lambda \sin\left(\frac{\theta_E}{2}\right) \tag{4.3}$$

where θ_E is the contact angle and λ is the capillary length. Taking into account these two last equation we can predict what will be the height of a puddle at a certain applied magnetic field and gradient. In figure 4.2 the values of measured thickness for a puddle of ferrofluid at two different concentrations and the corresponding predicted values are

compared. As can be seen the two profiles are in very good agreement with each other suggesting that the demagnetization factor due to the drop shape is not very important in this case. The capillary length can therefore be varied continuously by a factor up to nearly 5 without practically changing either the surface tension or the density of the liquid.

The graph in figure 4.3 (left) shows the dependence of the key shape parameters of ferrofluid drops of different concentrations deposited on a PDMS-coated glass surface kept at a 1 mm distance from the five different magnets. The contact angle θ remains constant except in the presence of magnet M5, where it is found to decrease with the drop concentration and a decrease down to the 50% is observed for the 3 mol/L solution. The height of the drop h and the diameter of the contact line D show even more complex behavior. For the magnets M1 to M4, a nonlinear decrease in D is accompanied by a nonlinear increase in h. These deformation effects can be very pronounced: at the concentration 3 mol/L, the diameter doubles, whereas the height becomes one-third with respect to the corresponding values of a diluted solution. This behavior confirms what reported in previous studies, which was explained in terms of a strong magnetic attraction that enhances the effect of the gravitational field [116] [49] [50]. Instead, for the magnet M5, D hardly changes, whereas h increases with the drop magnetization, suggesting that the normal traction due to a uniform magnetic field is dominant in this case (see section 2.3 for detailed explanation of the phenomenon).

The graph in figure 4.3 (right) shows that the drop flattening due to the gradient of the magnetic field and drop elongation due to the magnetic field, can be easily observed by varying the distance between the magnet and drop. Figure 4.3 shows the dependence of the key morphological parameters of ferrofluid drops of concentration 3 mol/L on the distance z from the three chosen magnets. With the largest magnet M5, which exhibits the smallest gradient, the maximum height h decreases by about 20% over a distance z $\sim$ 60 mm, whereas the diameter of the contact line D hardly changes. Mass conservation then implies an increase in the contact angle θ as displayed in the top graph: an increase of about 40° within 60 mm. With the magnet M2, characterized by the steepest magnetic field, the variations occur very close to it (z $<$ 20 mm) as expected. Within the first 10 mm, h increases sharply by a factor of 3, whereas D decreases by 30%, which is a clear indication of a pronounced flattening effect. After reaching a maximum (minimum) value, h(D) slowly decreases (increases), suggesting that above 10 mm the polarizing effect of the magnetic field becomes dominant. The contact angle θ trails h: after an initial peak, there is a weak increase at larger distances. Switching to the magnet M1, whose field variation is between the previous two, widens the flattening region to about

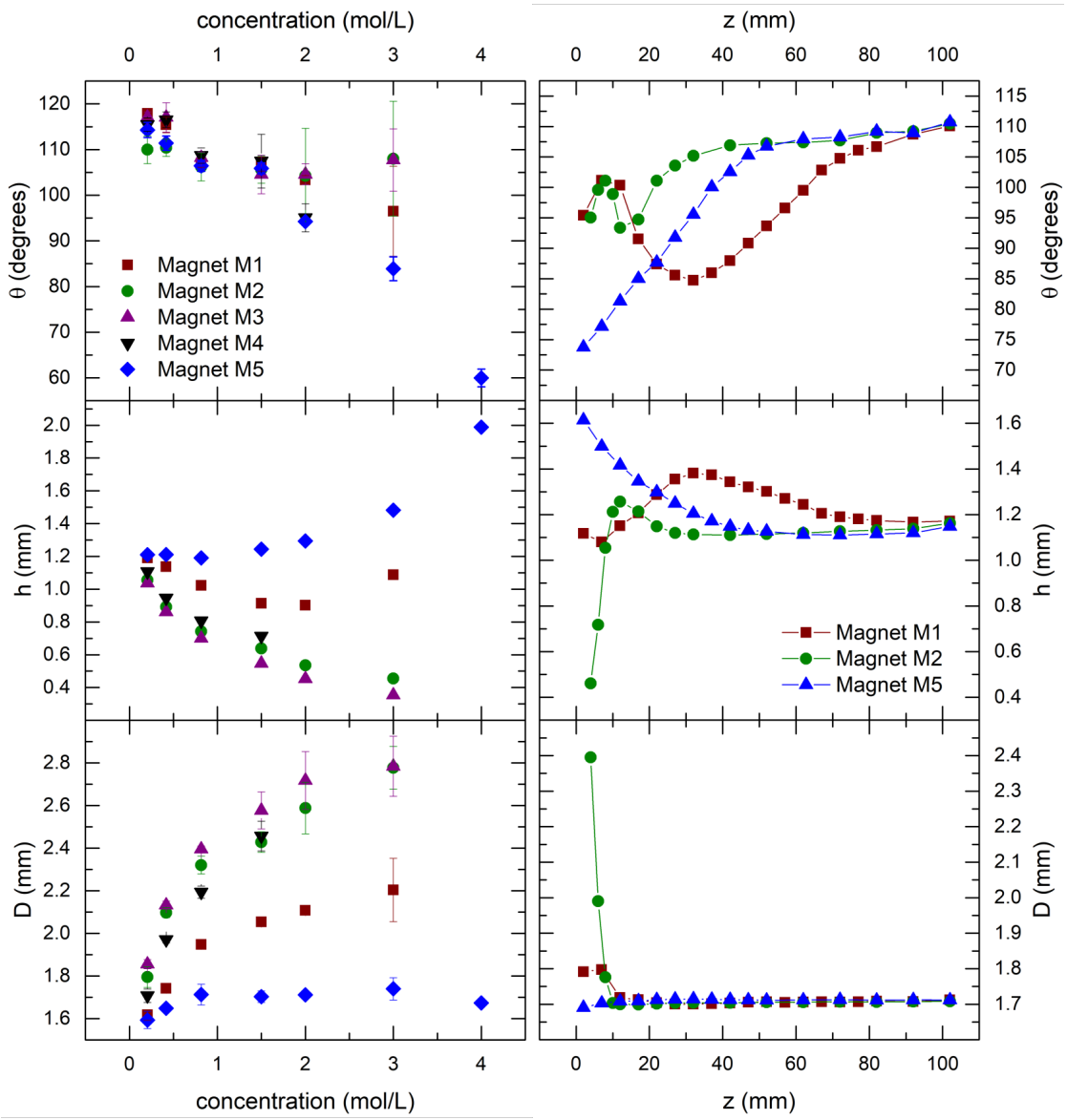

Figure 4.3 : Left: Contact angle (top graph), maximum height (middle graph), and diameter of the contact line (bottom graph) of ferrofluid drops of volume V = 2.5 μL and different concentrations deposited on a PDMS-coated glass slide in contact with the various magnets. Right: Variation of the contact angle (top graph), maximum height (middle graph), and diameter of the contact line (bottom graph) of ferrofluidic drops of volume V = 2.5 μL and concentration 3 mol/L with the distance z from the three characteristic magnets used before. The drops are deposited on a PDMS-coated glass slide.

40 mm. The nontrivial behavior just reported cannot be simply classified in terms of the intensity of the magnetic field to which the ferrofluid drops are exposed as done in refs [49] and [37]. In the effort to find a suitable scaling parameter to rationalize the role played by a magnet in the wetting properties of ferrofluid drops, we have plotted the main drop geometric data versus different dimensionless numbers. It turns out that the results for flattened ferrofluid drops are well described by the effective Bond number (see chapter 2.6): $Bo_{g^*} = \rho g^* V^{2/3} \gamma^{-1}$, which compares the effective attraction of a ferrofluid drop with the capillary force.

Figure 4.4 (left) shows the morphological data of ferrofluid drops of different concentrations and subject to the action of the five magnets placed at varying distances z in terms of Bo_{g^*}. The left graphs show only the data for $Bo_{g^*} > 1$. For a few selected points labeled with capital letters, the corresponding snapshots of the drop profiles are shown in insets. Most of the data are found to exhibit very similar trends within the reproducibility level of these measurements estimated to be about $\pm 5\%$: a nearly linear decrease (increase) in h(D), whereas θ hardly varies. The data corresponding to drops of concentration 3 mol/L interacting with the M1 magnet show a distinct behavior. Inset D clearly shows that in this case the normal traction dominates the attraction probably because of the low gradient of the magnetic field. This difference can be conveniently expressed in terms of the critical magnetization M_c, that is, the lowest value of the magnetization at which the Rosenweig instability can be observed [34] which we estimated from the formula valid for a flat slab of the ferrofluid with constant permeability:

$$M_c = 2\left(1 + \frac{\mu}{\mu_0}\right)\sqrt{\rho g^* \gamma} \tag{4.4}$$

We have found that the drops of concentration 3 mol/L in the presence of M1 are the only data points in figure 4.4 (left) where the drop magnetization is bigger than M_c. In other words, for all other data points, such a threshold is never reached regardless of the strength of the magnetic field. The points corresponding to $Bo_{g^*} < 1$ represent elongated drops whose profile is mainly affected by the normal traction pressure. In this limit, we find that a convenient way to describe the drop morphology is in terms of the dimensionless number [34] (see chapter 2.6): $S = \mu_0 M^2 V^{1/3} \gamma^{-1}$ which compares the magnetic traction pressure with the capillary pressure. At the upper point of the sessile drop, where B is normal to the drop surface, there is a reduced pressure inside of the drop as compared to the points in contact with the substrate, where the field component normal to the surface nearly vanishes. This pressure decrease can be balanced by increasing the curvature at the upper point and decreasing it at the contact points.

As a result, the drop is stretched along the field. Figure 4.4 (right) shows the main morphological quantities of elongated drops characterized by $Bo_{g^*} < 1$ plotted in terms of S. Also in this set of graphs the drop profiles shown in insets corresponds to a few selected points labeled with capital letters. The data are found to nicely collapse on single curves: a linear decrease (increase) in θ(h), whereas D hardly varies, suggesting that the apparent contact line remains pinned. We point out also that all data with $S > 1$ have a magnetization bigger than M_c and this might be a clue that the elongation on linked to the Rosensweig critical phenomenon. The same overall behavior has been observed with sessile ferrofluid drops deposited on hydrophilic surfaces and on nearly superhydrophobic surfaces (see figures 4.5 and 4.6).

§ 4.3. Conclusions

In conclusion, we have studied the magnetowetting behavior of sessile drops of ferrofluid water solutions at various concentrations deposited on a flat substrate and subject to the action of permanent magnets of different sizes and strengths. A rich phenomenology has been observed, ranging from the flattining of drops caused by the magnetic attraction to the elongation of drops due to the normal traction pressure in a uniform magnetic field. We find that the flattening effect can be conveniently described in terms of the effective Bond number $Bo_{g^*} = \rho g^* V^{2/3} \gamma^{-1}$, which compares the effective downward drop attraction with the capillary force, whereas the drop vertical elongation can be expressed using the dimensionless Traction number $S = \mu_0 M^2 V^{1/3} \gamma^{-1}$, which compares the magnetic traction pressure with the capillary pressure. This phenomenology can be exploited to manipulate ferrofluid drops [37].

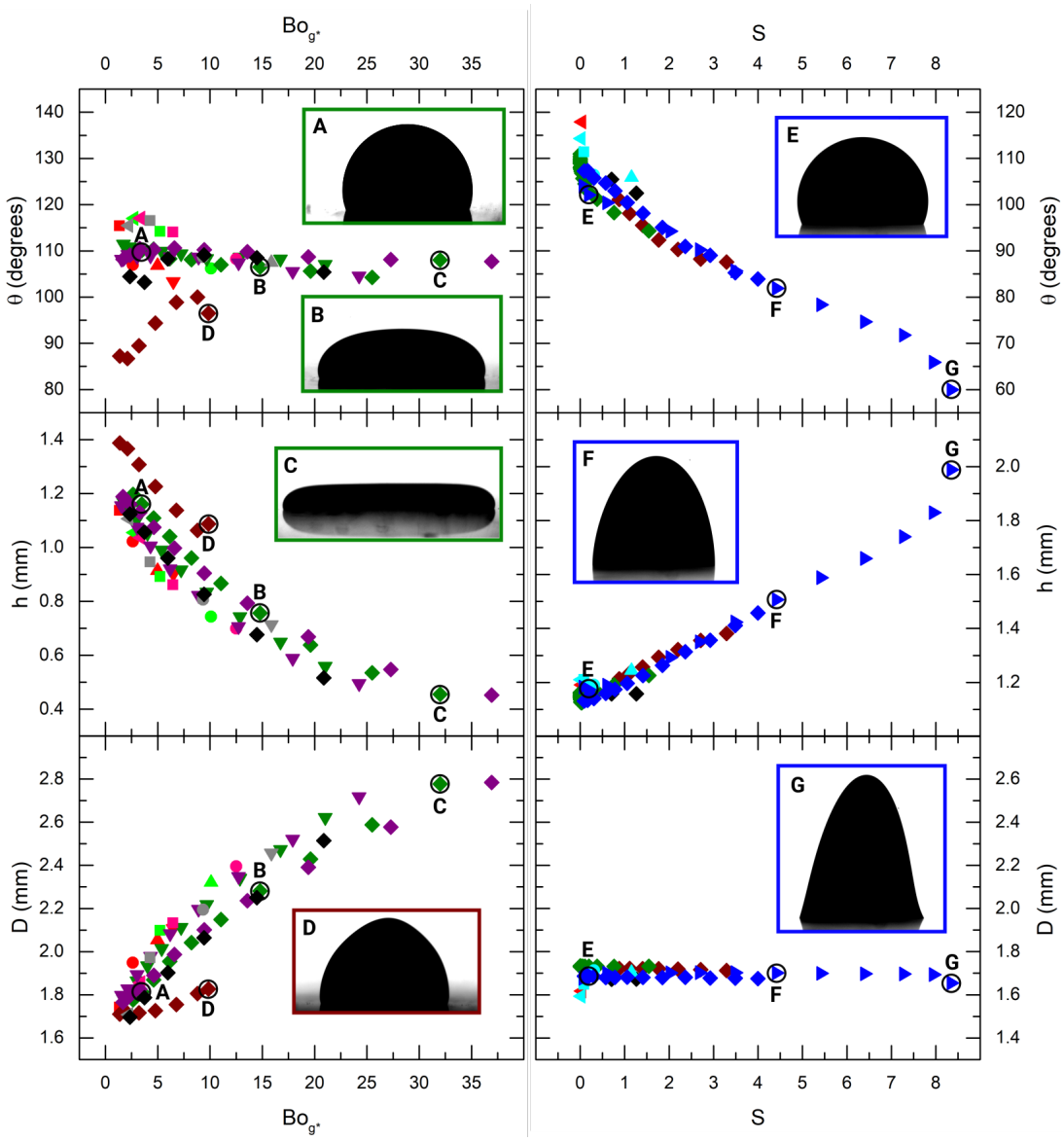

Figure 4.4 : Contact angle (top), maximum height (middle), and diameter of the contact line (bottom) of ferrofluid drops of volume V = 2.5 μL as a function of the effective Bond number Bo_{g*} (left) and in function of the traction number S (right). The symbols represent different concentrations of the ferrofluidic solutions: $\triangleleft$ 0.2 mol/L, $\square$ 0.4 mol/L, $\circ$ 0.8 mol/L, $\triangle$ 1.5 mol/L, $\triangledown$ 2 mol/L, $\diamond$ 3 mol/L, and $\triangleright$ 4 mol/L. Different colors are associated with the magnets according to the following palette: (maroon and red) magnet M1, (dark green and light green) magnet M2, (purple and pink) magnet M3, (black and gray) magnet M4, and (blue and aqua blue) magnet M5, where the first (second) color corresponds to measurements done changing the distance of the magnet from the sample (with the magnet in contact with the substrate). The drops are deposited on a PDMS-coated glass slide.

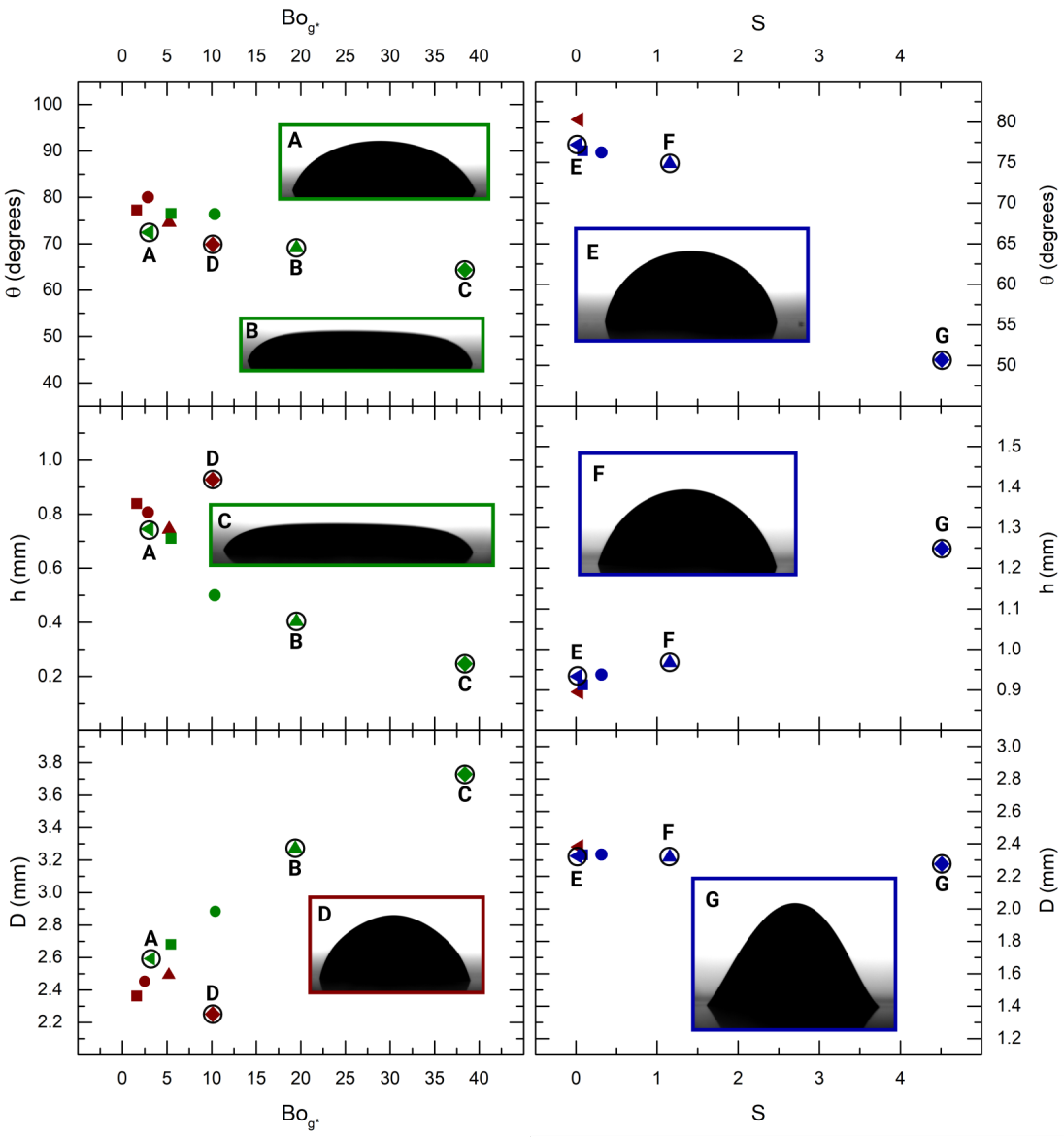

Figure 4.5 : Contact angle (top), maximum height (middle), and diameter of the contact line (bottom) of ferrofluid drops of volume V = 2.5 μL as a function of the effective Bond number Bo_{g*} (left) and in function of the traction number S (right). The symbols represent different concentrations of the ferrofluidic solutions: $\triangleleft$ 0.2 mol/L, $\square$ 0.4 mol/L, $\circ$ 0.8 mol/L, $\triangle$ 1.5 mol/L, $\triangledown$ 2 mol/L and $\diamond$ 3 mol/L. Different colors are associated with the magnets according to the following palette: maroon magnet M1, dark green magnet M2, and blue and magnet M5. The drops are deposited on a NOA-coated glass slide.

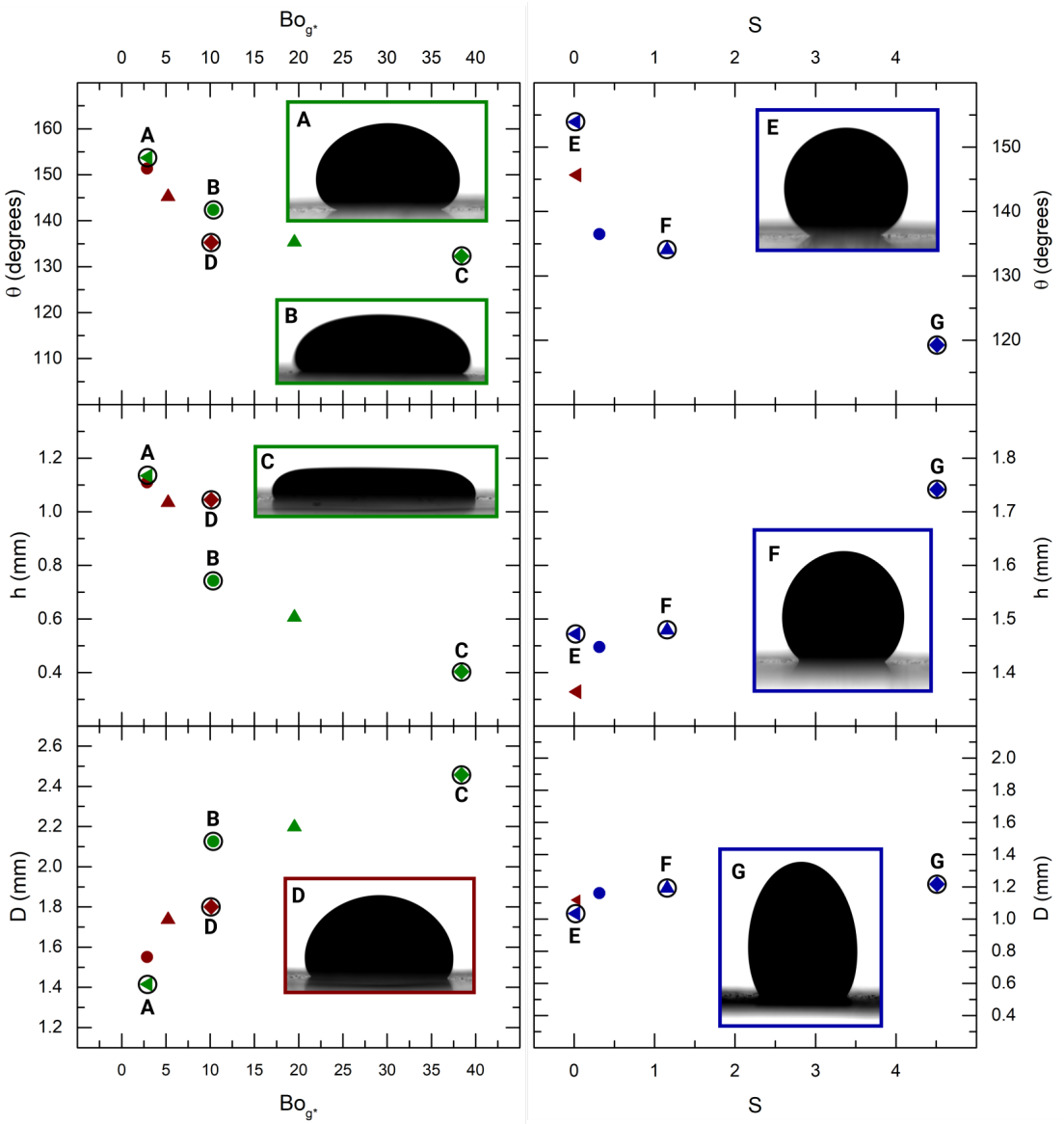

Figure 4.6 : Contact angle (top), maximum height (middle), and diameter of the contact line (bottom) of ferrofluid drops of volume V = 2.5 μL as a function of the effective Bond number Bo_{g*} (left) and in function of the traction number S (right). The symbols represent different concentrations of the ferrofluidic solutions: ◁ 0.2 mol/L, □ 0.4 mol/L, ○ 0.8 mol/L, △ 1.5 mol/L, ▽ 2 mol/L and ◇ 3 mol/L. Different colors are associated with the magnets according to the following palette: maroon magnet M1, dark green magnet M2, and blue and magnet M5. The drops are deposited on a Lotus leaf.

Chapter 5

Magnetosliding

The dynamics of liquid drops on solid surfaces is attracting a lot of attention thanks to its fundamental implications and technological applications. In this chapter, a comprehensive experimental study of the interaction between gravity-driven ferrofluid drops and a patterned magnetic field is presented. To exclude any pinning effect and understand completely the role of the magnetic field we have used oil impregnated surfaces. We have found that the drop speed can be accurately tuned regulating the magnetic interaction and drops are found to undergo a stick-slip motion whose contrast and phase can be easily controlled by changing either the strength of the magnetic field or the nanoparticles concentration in the ferrofluid. This particular motion is the result of the periodic modulation of the external magnetic field. After giving a brief introduction to the topic on the motion of sessile droplets in section 5.1 we will describe the experimental results and their interpretation in confront to the literature in section 5.2. The results presented in this chapter are described also in an article published in Langmuir [117].

§ 5.1. Introduction

A way to control passively the droplet motion is to tailor chemically heterogeneous surfaces. For instance, water drops sliding on alternating stripes of different wettability introduce anisotropic behavior: drops slide more easily along the alternating stripes than across them [118, 119], and periodic variations in the contact angles, possibly accompanied by fluctuations in the drop velocity, take place in this latter direction [119]. Another interesting observation for this case of study is that if the wettability contrast between adjacent stripes is high, then drops undergo a stick-slip motion whose average speed can be an order of magnitude smaller than that measured on a homogeneous surface having the same apparent contact angle [120]. This motion is the result of the

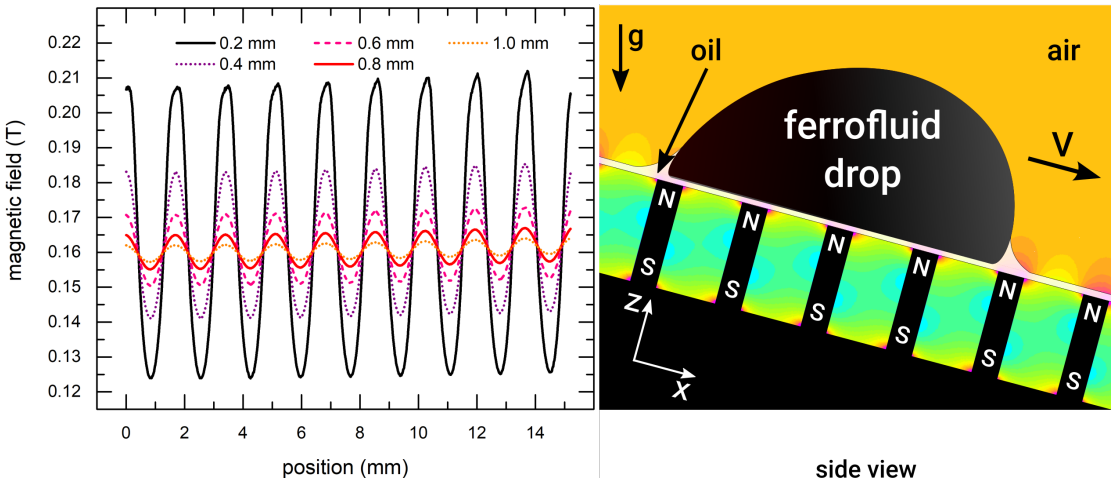

Figure 5.1 : Left: spatial modulation of the magnetic field at different distances from the magnet. Right: experimental setup: a ferrofluid drop of known volume is deposited on a silicone oil-impregnated surface tilted by an angle α placed above a permanent magnet. Its stationary speed is denoted as v. To modulate the magnetic field, an iron comb is placed between the magnet and the impregnated surface.

periodic deformations of the drop interface when crossing the stripes. Lattice Boltzmann simulations reproduce the stick-slip motion and indicate that the slowdown is the result of the localized energy dissipation due to the pinning-depinning transition of the contact line [16, 120]. More recent numerical studies have analyzed additional features of the stick-slip motion of drops on chemically patterned surfaces [121–124]. In this chapter, we present the first experimental evidence of the role played by a patterned magnetic field on the dynamics of ferrofluid drops. A continuous and controlled evolution from uniform to stick-slip motion is observed, changing the ferrofluid concentration and/or the magnetic field. More interestingly, the delay between the depinning of the front and rear contact lines is found to depend on the mean speed of the drop.To exclude any pinning effect and understand completely the role of the magnetic field we have a rough surface impregnated with oil. Since the oil surface is intrinsically smooth and free from chemical and morphological defects typical of solid surfaces, these so-called liquid impregnated surfaces (LISs) are recognized to hardly pin sessile drops [2, 12, 13].

§ 5.2. Results and discussion

In this study we use ferrofluid drops on conventional LIS produced following the recipe described in section 3.4. On the basis of preliminary measurements, the 100 cSt silicone oil has been chosen as a lubricant for this work because it allows us to easily explore an

ample interval of velocities with suitable inclinations. Its viscosity (around 100 times that of the ferrofluids) avoids drainage of the impregnated oil by the moving drops and, at the same time, yields very low roll-off angles well below 5°. To explore the influence of the magnetic interaction on the dynamics of ferrofluid drops, eight different concentrations are used. The experimental setup described in section 3.3.2 allows us to acquire images of a drop on an inclined surface (see also figure 5.1 left). During a typical experiment, a drop (with volume $\Omega \simeq 10 - 40$ μL) is deposited on the already-tilted surface and its motion is recorded. Side views show that drops are quasi-hemispherical and surrounded by a small oil meniscus as shown schematically in figure 5.1. This surrounding meniscus, pulled from the oil film by the surface tension of water [125], is found to persist under dynamic conditions, which influence the friction opposing the moving drop [89]. The permanent magnet, described in section 3.2, is made of neodymium and has a cylindrical shape (diameter 18 cm, height 3 cm). The wide surface guarantees that a drop moving on its central part experiences an almost uniform magnetic field whose strength depends only on the vertical distance z from the surface of the magnet as can be seen in the right graph of figure 3.2. A comb-shaped iron sheet of thickness 2 mm is placed on the permanent magnet and modulates the magnetic field along the drop sliding direction (x axis, see schematic representation in figure 5.1), as reported in the graph in figure 5.1. The teeth have a width of 0.5 mm and a period of 1.7 mm. The drop is deposited on the LIS sample placed on the iron comb. We can control the modulation effect by changing the distance of the sample from the magnet: as the distance is increased the modulation of the magnetic field decreases as shown in the graph figure 5.1. The profile of the patterned magnetic field used in this study is that corresponding to a distance of 0.2 mm. The droplet interaction with the magnetic field can be characterized by the effective gravitational acceleration $g^* = g + f_m(z)$, with g being the acceleration due to gravity, $f_m = M(B)\nabla(B)$ being the magnetic force per unit volume exerted by the magnet, M(B) being the ferrofluid magnetization at the applied magnetic field B, and $\nabla(B)$ being the gradient of the magnetic field. For the uniform magnetic field $g^* \simeq 10$ m/s^2, while on the patterned magnetic field, g^* can be as high as 1300 m/s^2 locally.

The left graph of figure 5.2 shows the data relative to the time evolution of the drop frontal position of ferrofluid drops deposited on lubricant-impregnated surfaces inclined by an angle $\alpha = 25°$ in the presence of either a uniform or a modulated magnetic field. The drops subject to a uniform magnetic field slide at a constant speed that decreases with ferrofluid concentration (corresponding data indicated with the empty symbols). Since no apparent variations in the oil meniscus or the drop shape are observed, we ascribe this loss to the magnetoviscous effects [39]: the viscosity of maghemite ferrofluids

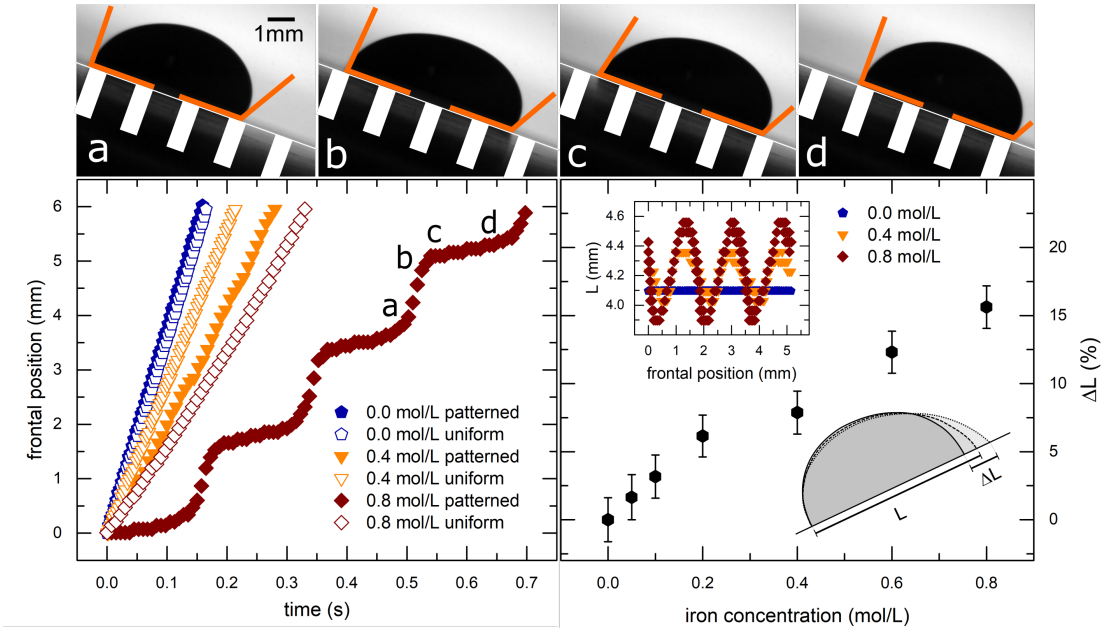

Figure 5.2 : (Upper slideshow): the snapshots show the position of the drop with respect to the underlying magnetic pattern at specified instants. The orange lines indicate the contact angles. (Left) Time evolution of the frontal point of ferrofluid drops at different concentrations (volume = 20 μL) moving on liquid-impregnated surfaces inclined by an angle $\alpha = 25°$ in the presence of either a uniform or a patterned magnetic field. (Right) Percentage variation of the drop length ΔL during stick-slip as a function of ferrofluid concentration. The inset underlines the drop length oscillation (L) during the motion for three particular concentrations.

increases with concentration and the application of a magnetic field further enhances this effect (see section 2.5 for further details). On a patterned magnetic field, the speed decreases and, at highly concentrated solution, a pronounced stick-slip motion appears, similar to what has been reported for water drops sliding on stripes of alternating wettability [120]. In other words the motion of the drop can be continuously changed from a "rigid" drop moving at constant speed to an oscillating drop undergoing periodic stick-slip motion by varying either the ferrofluid concentration, as done here, or, more generally, the magnetic strength. This tuning is a significant advantage with respect to the passive control provided by chemically heterogeneous surfaces whose effects on the drop dynamics can be modified only by varying the nature or shape of the different chemical domains [2]. Selected snapshots in the top part of the figure indicate the position of the droplet contact line (CL) with respect to the underlying iron comb. Between images a and b, the rear part of the CL is pinned at the edge of a tooth of the comb while the frontal part CL slowly moves down; at consecutive instant c, the frontal CL stops at the edge of a tooth comb and the rear starts moving until in instant d it gets pinned at the edge of the following tooth comb and the system recovers the initial configuration with only a spatial transition by one pattern periodic distance. This alternating pinning and depinning of the frontal and rear CL implies a periodic oscillation in the instantaneous length L of the sliding drop. Additionally, the oscillation ΔL, evaluated as the difference between the maximum and minimum measured values of droplet length L, increases with the ferrofluid concentration ad so with the magnetic interaction, as shown in the right graph of figure 5.2.

We exploit the possibility to tune the oscillations to systematically characterize the phase shift φ of the stick-slip motion by varying the inclination angle of the plane α, the drop volume and ferrofluid concentration. The phase shift is calculated from the ratio $\varphi = 2\pi\frac{\Delta T}{T}$, where ΔT is the time interval between the consecutive instants of maximum acceleration of the frontal and rear contact points and T is the time interval between two consecutive instants of maximum acceleration of the frontal contact point. Therefore, $\varphi = 0$ corresponds to a rigid translation of the drop, while when $\varphi = \pi$ the front and rear contact points alternate their motion in counter-phase. The graph in figure 5.3 shows the variation of φ in function of the drop speed v. In each case, the mean drop speed is determined by the slope of least-squares linear fits of the time evolution of the frontal points for either uniform (v_u) or patterned (v_p) magnetic fields. A linear trend is seen up to $v = 60$ mm/s. Increasing he volume up to $\Omega = 40$ μL the droplets reach $\varphi = 2\pi$ at around 80 mm/s. Above this speed, φ keeps on increasing linearly. Furthermore, two distinct regimes are observed during drop motion. If the speed is low (shaded area of

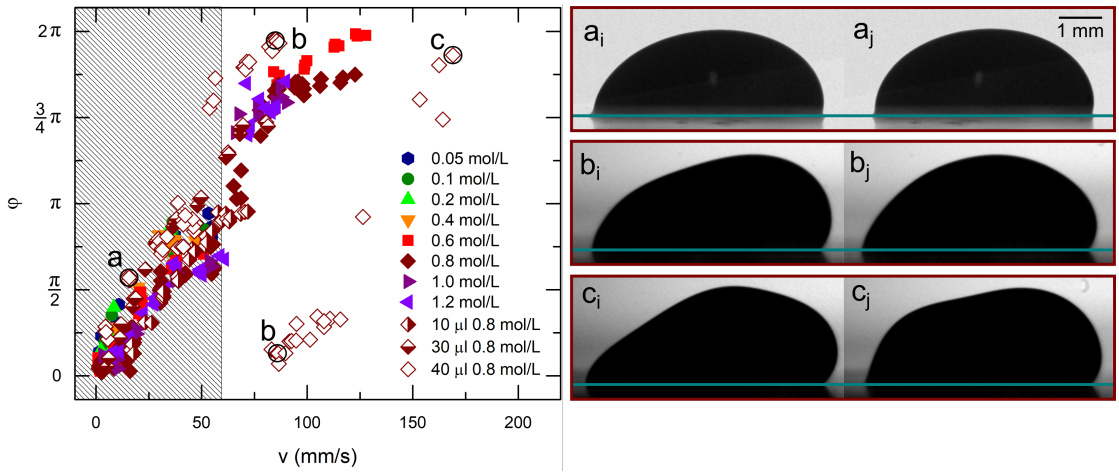

Figure 5.3 : (Left) Sliding phase as a function of the drop speed, varying ferrofluid concentration (different colors), and drop volume (different fill of the symbol). The gray background represents conventional stick-slip, while the white part indicates where the vertical oscillations of the drop profile appear. (Right) Frames at the maximum (i) and minimum (j) elongation instants of drops (40 μL, 0.8 mol/L) moving at three different speeds. The two points b in the graph display the same motion described in snapshots b_i and b_j.

the graph), only the edge near the front and rear contact lines change during a stick-slip motion as shown by the snapshots a_i (a_j) taken at the instant of maximum (minimum) elongation of the moving drop. At higher speed, the oscillation motion involve entire drop profile as indicated by the images b_i and b_j. If we increase the speed further, this oscillation becomes more pronounced (see images c_i and c_j). If we analyze in more detail the data at high ferrofluid concentration where the stick-slip motion is more marked, we find that φ does not depend on the ferrofluid concentration and thus the magnetic force. This last observation might indicate that the properties observed are characteristic of the stick-slip motion itself.

To understand better the interplay between drop dynamics and the magnetic field, systematic measurements are performed at a constant drop volume ($\Omega = 20$ μ L) changing the ferrofluid concentration and the angle α. The left graph of figure 5.4 summarizes all speed data plotted in terms of the ferrofluid concentration for increasing inclination angles. It clearly shows that the drop speed decreases with the ferrofluid concentration as already discussed. At concentrations greater than 0.4 mol/L, the presence of the pattern significantly slows the drops as compared to the uniform field, indicating the presence of extra dissipation due to deformation of the drop undergoing stick-slip. The speed decrease is larger at higher concentrations where the oscillations are more pronounced,

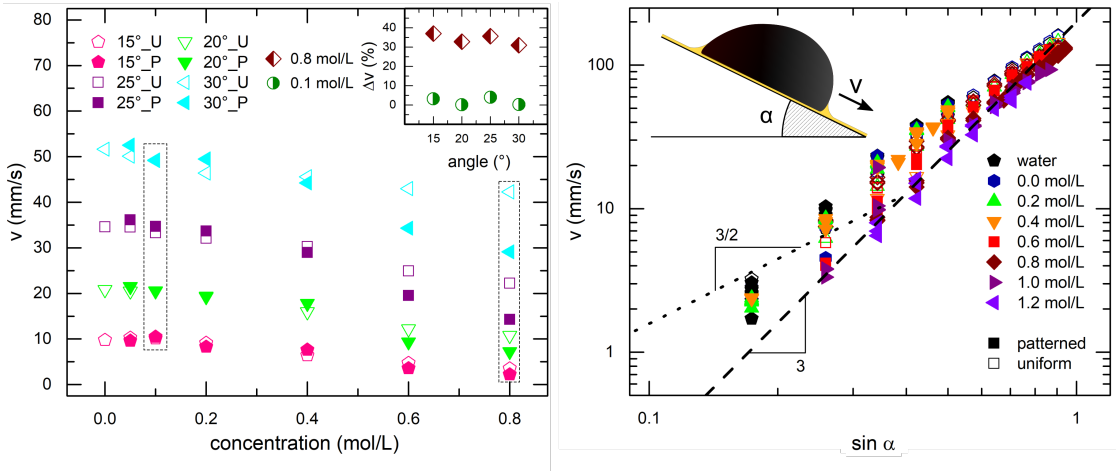

Figure 5.4 : (Left) Mean velocity of ferrofluid drops ($\Omega = 20$ μL) of different concentrations moving on LIS at increasing inclination angles in the presence either of a uniform (U, open symbols) or a patterned (P, full symbols) magnetic field. The inset compares the relative velocity decrease at two ferrofluid concentrations (the points enclosed in the two dashed boxes) on the same patterned surface at increasing α. (Right) The same data plotted in terms of $\sin\alpha$ proportional to the in-plane component of the gravitational driving force.

as displayed in the inset of figure 5.4, where the relative velocity decrease $\Delta v = \dfrac{v_u - v_p}{v_u}$ is plotted as a function of α. The patterning reduces the drop speed by about 35% for a droplet concentration of 0.8 mol/L, and it is barely observable at a concentration of 0.1 mol/L. Interestingly, this decrease does not seem to depend on the inclination angle, at least in the explored range. Finally, as a result of the weak pinning LIS, we notice that this decrease is much smaller than the factor of 10 reported for water drops sliding on chemically heterogeneous surfaces [120].

Following the approach described [89] we decided to plot the speed on a log scale as a function of the sine of the inclination angle as shown in the right graph in figure 5.4. The plotted data corresponds to ferrofluid drops having $\Omega = 20$ μL and different molar concentrations in the presence of either uniform or patterned magnetic fields. On this compressed scale, the differences in drop velocity observed between the uniform and patterned magnetic fields disappear and the data show that v is not linear in driving force but rather exhibits power law behavior. Because the silicone oil is more viscous than the ferrofluid, dissipation is expected to mainly occur in the oil, that is, in the underlying film and in the surrounding meniscus. In the already cited recent study [89] is shown that, contrary to what one could think a priori, the dominant contribution to dissipation is not in the subadjacent film. The analysis of the viscous effects in the front edge of the

moving meniscus yields nonlinear friction and estimates that $v \simeq \sin^{3/2}\alpha$ [89]. As the driving force is increased, the wedge dissipation is suddenly suppressed, which leads to a different dynamic regime that seems to arise from the self-lubrication of the drop where $v \simeq \sin^3\alpha$, explained by assuming that oil is constantly extracted from the texture by water surface tension before being reinjected below the drop [89]. In our case we observe a superlinear behavior which, at the highest inclinations and in the presence of a uniform magnetic field (full symbols), is consistent with a power law with exponent 3. As $\sin\alpha$ decreases, the exponent becomes smaller, and there may be a crossover to the $sin^{3/2}\alpha$ regime at a critical velocity of $v \simeq 1$ cm/s.

§ 5.3. Conclusions

In this chapter we have characterized the influence of a uniform and a heterogeneous magnetic field on the motion of ferrofluid drops on slippery surfaces. The application of a uniform magnetic field slows gravity-driven ferrofluid drops. The presence of magnetic patterning significantly enriches the drop dynamics. In particular, a linear modulation in the magnetic field causes a stick-slip motion whose contrast and phase can be easily tuned. We have also found that the phase shift between the moving frontal and rear contact points changes continuously with the drop velocity from 0 to 2π. These effects could also be seen with a standard solid surface but the data reproducibility would be much lower, and constructing a graph of the phase variation like that in figure 5.3 would be practically impossible. A specific feature of LIS is the nonlinear friction of moving drops, which we have measured and found to be consistent with a recent specific study [89] where it is attributed to the dissipation taking place in the oil meniscus surrounding the drop.

These experimental results suggest that ferrofluid drops moving in the presence of heterogeneous magnetic fields represent an ideal playground for fundamental studies on drop dynamics and provide useful strategies for passive and active control of drop motion. Surprisingly, there is very little in the literature on the dynamics of ferrofluid drops in the presence of magnetic fields. It is our hope that this preliminary work be a stimulus for further studies, both experimental and theoretical.

Chapter 6

Droplet division

In this chapter we report a comprehensive study of the division of ferrofluid drops caused by their interaction with a permanent magnet. As the magnet approaches the sessile drop, the drop deforms into a cone and then divides into two droplets. This process is the result of a complex interplay between the polarizing effect caused by the magnetic field and the magnetic attraction due to the field gradient. To describe this phenomenon, in each scan we identify two characteristic magnet-droplet distances: z_{max}, corresponding to distance for which the drop reaches its maximum height, and z_{saddle}, corresponding to the distance for which appears a saddle point on the drop peak identifying the beginning of the drop breakup. To investigate the phenomena we have used sessile drops of ferrofluid water solutions at various concentrations and volumes, deposited on four surfaces of different wettability. An empirical scaling law based on dimensionless parameters is found to accurately describe these experimental observations. Finally we have also estimated the maximum diameter of the ferrofluid drops in the moment before the division and found that it is very close to a critical size, which value depends on the magnetic attraction. These results have been recently published in Langmuir [126].

§ 6.1. Introduction

Ferrofluid drops on superhydrophobic surfaces represent a model system to study and bridge the gap from static to dynamic self-assembly [37]. The droplets self assemble under a static external magnetic field into simple regular patterns that can be switched to complicated dynamic dissipative structures by applying a moving magnetic field. In a typical experiment, one drop of aqueous ferrofluid is placed on a superhydrophobic surface and subjected to a magnetic field of a cylindrical permanent magnet below the substrate. Increasing the field strength B and the vertical gradient dB/dz acting on

the drop (by approaching the magnet to the surface) eventually leads to the breakup of the drop into two or more smaller daughter droplets. The division phenomenon is quite fast and takes a few tens of milliseconds, after which the daughter droplets briefly oscillate before settling at their equilibrium separation. The drop breakup is in some way related to the normal-field instability of ferrofluids (so-called Rosensweig instability) [37]. The characteristic pattern of the normal-field instability is observed by applying a perpendicular uniform magnetic field to a pool of ferrofluid, which produces the spontaneous generation of an ordered pattern of surface peaks having a critical wavelength [34, 36]:

$$\lambda_c = 2\pi\sqrt{\frac{\gamma}{\rho g}} \tag{6.1}$$

with ρ and σ being the density and the surface tension of the ferrofluid, when the magnetization exceeds the critical magnetization [34, 36]:

$$M_c^2 = \frac{2}{\mu_0}\left(1 + \frac{\mu_0}{\mu}\right)\sqrt{\rho g \gamma} \tag{6.2}$$

where μ_0 (μ) is the vacuum (ferrofluid) magnetic permeability [34, 36]. If we increase the magnetic field starting from zero, we observe that the fluid interface is perfectly flat over a range of field intensities up to the point when the transition suddenly occurs. Conversely, no increase in the applied field, no matter how large, can cause the interface to be unstable if the saturation magnetization of the fluid is less than M_c. In contrast to the scenario of a pool of ferrofluid, the gravitational force in the droplet experiment [37] is negligible as compared to the magnetic force due to the vertical field gradient; that is, the effective gravitational acceleration [52, 116] $g^*(z) = g + \dfrac{M(B)\nabla(B)}{\rho}$, where $M(B)$ is the ferrofluid magnetization corresponding to B and $\nabla(B)$ is the gradient of the magnetic field, is up to 2 orders of magnitude larger than g. Thus, the revised formula of the critical length:

$$d_c = 2\pi\sqrt{\frac{\gamma}{\rho g^*}} \tag{6.3}$$

does not determine the periodicity of the pattern but instead provides a criterion for the division: a droplet divides when the d_c becomes smaller than the diameter [37]. Numerical simulations of a thin ferrofluid film subjected to an applied uniform magnetic field show that the subtle competition between the applied field and the Van der Waals induced dewetting determines the appearance of satellite droplets [127]. The division of the ferrofluid drops is a subject not fully understood, in fact apart from the cited studies, the division of ferrofluid drops has not been further analyzed. To shed more

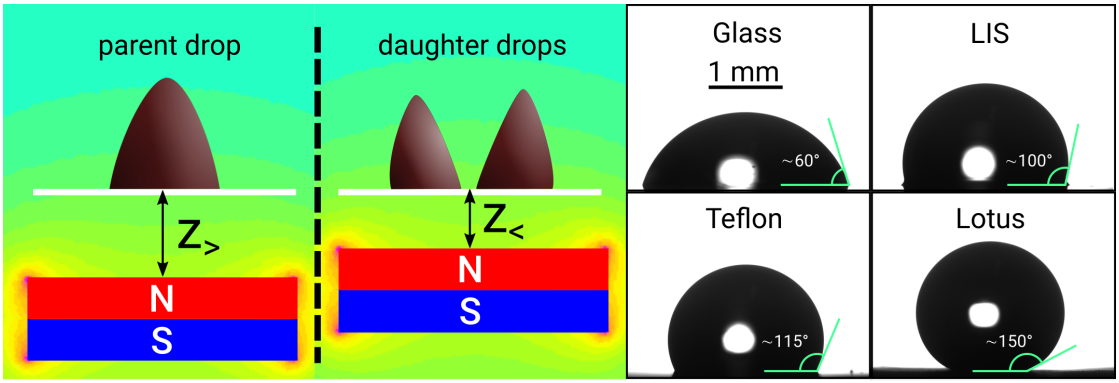

Figure 6.1 : Schematic representation of the disposition of the substrate, ferrofluid drop, and magnet. Colors highlight the intensity of the B in arbitrary units. (Right) Snapshots of water drops on the four different surfaces used in this study. The volume of the drops is 4 μL. For each surface, the apparent contact angle is reported

light on this phenomenon, we have thus decided to systematically study the division of a ferrofluid drop in two daughter droplets induced by a magnetic field exploring its dependence on the major quantities involved, that is, the nature of the substrate, the magnetic interaction, and the drop volume.

§ 6.2. Results and discussion

The typical experimental procedure is the following: ferrofluid drops of volume Ω (on the order of tens of μL) are gently deposited on a horizontal substrate with a micropipette and are subject to an external magnetic field. The magnetic field B is produced by a cylindrical neodymium magnet (diameter 45 mm, thickness 30 mm), of grade N40 and residual magnetic field 1.25 T (see section3.2 for further details, magnet code: M1). An elevator controlled by a stepping motor varies the distance of the permanent magnet from the bottom of the glass slide in a precise way. For further details on the optical setup see section 3.3.1. Four different substrates are chosen to span an ample wettability range (see section 3.4 for further details on the production and fig. 6.1 for a collection of snapshots of water droplets on these surfaces). The iron concentrations, the magnetic susceptibilities (χ_m), and the magnetizations at saturation (M_{sat}) of the ferrofluid solutions used in this study are: 7.5 mol/L ($\chi_m = 1.56$, $M_{sat} = 38.2$ kA/m), 6.0 mol/L ($\chi_m = 1.28$, $M_{sat} = 32.4$ kA/m), 5.0 mol/L ($\chi_m = 1.11$, $M_{sat} = 29.6$ kA/m), and 4.0 mol/L ($\chi_m = 0.76$, $M_{sat} = 24.3$ kA/m. We point out that our highest M_{sat} is less than one-half that used in the original work [37].

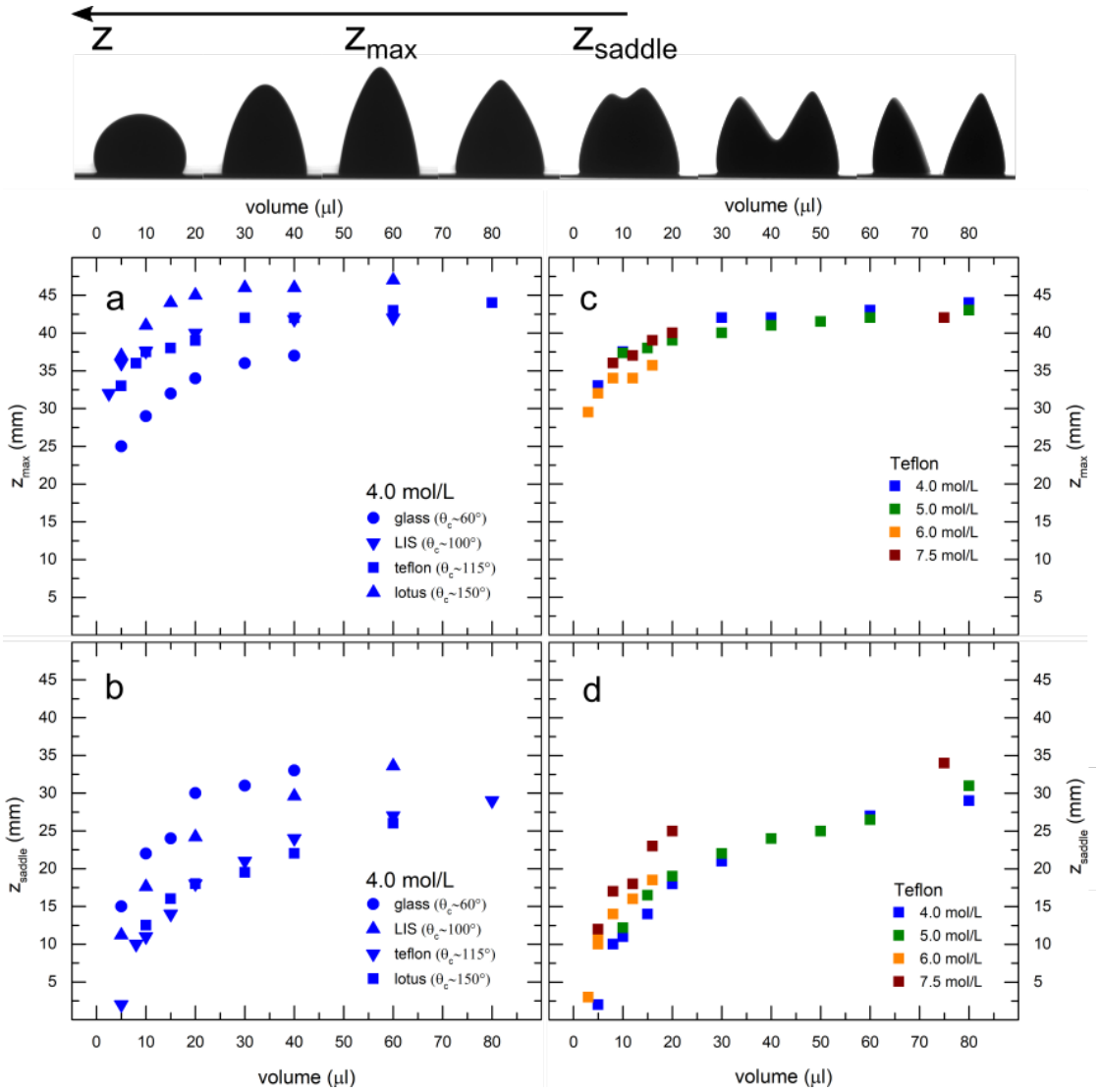

Figure 6.2 : (Top) From left to right snapshots of the deformations of a ferrofluid droplet at decreasing distances z from the magnet. The snapshots after z_{saddle} is reached are taken with the magnet kept at constant magnet-substrate distance ($z = z_{saddle}$), at successive times, increasing from left to right. (a) Variation of the distance magnet-substrate corresponding to the maximum elongation of the drop with the drop volume Ω. The data refer to a ferrofluid concentration equal to 4.0 mol/L and to different surfaces. (b) Variation of the distance magnet-substrate corresponding to the formation of a saddle point at the top of the drop with Ω. (c) Variation of the distance magnet-substrate corresponding to the maximum elongation of the drop with Ω. The data refer to ferrofluid droplets of different concentrations deposited on a Teflon substrate. (d) Variation of the distance magnet-substrate corresponding to the formation of a saddle point at the top of the drop with Ω.

The contour of the droplet is recorded as the distance z from the permanent magnet is gradually decreased (see figure 6.1). The resulting increase of the magnetic interaction with the drop leads to a deformation of the drop from a spherical cap into a spiked cone and a division into smaller drops at precise z values. The division of the drop is due to a combination of high magnetic field and high vertical magnetic field gradient and, therefore, does not take place in a homogeneous magnetic field [37]. This process is irreversible: the droplets do not coalesce back to a single drop when the magnet is moved away due to their magnetic repulsion [37]. In the specific case of our experimental setup, if the volume of the mother drop is less than about 40 μL, it divides into two daughter droplets. If $40 < \Omega < 60$ μL, three daughter droplets are observed. In this study, we consider only the division into two droplets. Figure 6.2 (top slideshow) shows a typical evolution of the drop shape. The overall behavior is not affected by the nature of the substrate and resembles that reported on a superhydrophobic surface [37]. Despite the overall behavior is the same, we do find quantitative differences among the different surfaces. As a first attempt to describe this process, during each scan we identify two characteristic distances: z_{max}, corresponding to distance for which the drop reaches its maximum height, and z_{saddle}, corresponding to the distance for which appears a saddle point on the drop peak identifying the beginning of the drop breakup. With the magnet fixed at this position, the saddle becomes more pronounced and moves downward, until it touches the surface forming two separated droplets. The division process takes a fraction of a second to be completed (see supplementary movie S2 of article [126]). We have not analyzed in detail these dynamics but we can affirm that increasing the ferrofluid concentration accelerates the division and that the different substrates do not seem to play any major role. The two left graphs of figure 6.2 a and b show the variation, respectively, of z_{max} and z_{saddle} with the volume of ferrofluid drops having a concentration of 4 mol/L deposited on the four different surfaces. Each data point is the average of at least five z measurements repeated under the same nominal conditions. we have chosen 4 mol/L as the lowest concentration because for lower concentrations, no formation of the saddle point is observed. The graph of figure 6.2a shows that z_{max} practically does not change for large drops ($\Omega \geq 30\mu L$). If the volume is smaller instead, the magnet must get closer to overcome the surface tension contribution. The data exhibit a distinct dependence on the substrate: z_{max} increases with the apparent contact angle, indicating that the magnetic interaction required to change the shape to form an elongated drop decreases with the degree of hydrophobicity of the surface. A similar trend is shared by z_{saddle}, although the values are now smaller, indicating that the formation of the saddle point requires a larger magnetic interaction. Instead, there

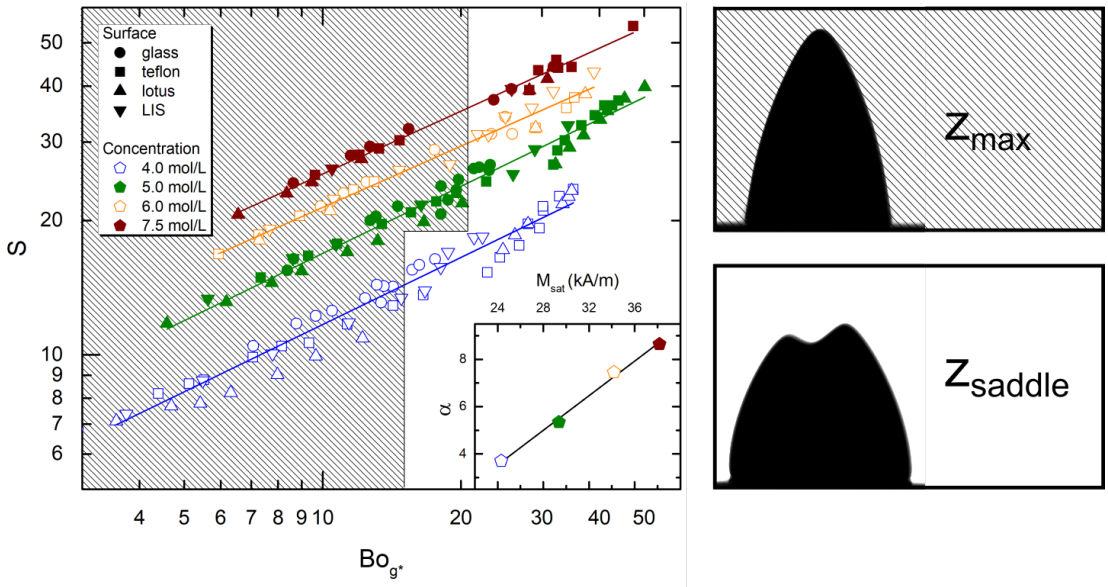

Figure 6.3 : Saddle points (graphically enclosed in the white region) and maximum points (enclosed in the dashed region) plotted in terms of the dimensionless parameters Bo_{g^*} and S. Lines are power-law fits according to the formula $S_c = \alpha Bo_{g^*}$, where α is a free parameter. Its value is reported in the inset as a linear function of the magnetization at saturation of the ferrofluid solutions.

does not seem to be a dependence on the ferrofluid concentration for a given substrate as displayed by the graphs of figure 6.2c and d. However, the ferrofluid concentration must be higher than a threshold concentration, below which no complete division is found.This minimum concentration depends on the magnetic field generated by the magnet and is found at about 6 mol/L in our case.

In the attempt to rationalize these empirical observations, we have tried to convert these data in terms of dimensionless parameters. Following the reasoning presented in section 2.4 in the presence of a strong gradient of the magnetic field, the Rosensweig instability of a pool of ferrofluid takes place at a critical magnetization yielded by inserting the effective gravitational acceleration g^* in eq. 6.2. If we introduce the effective Bond number $Bo_{g^*} = \rho g^* V^{2/3} \gamma^{-1}$ and the dimensionless traction number $S = \mu_0 M^2 V^{1/3} \gamma^{-1}$ the critical magnetization can be expressed as

$$S_c = 2\left(1 + \frac{\mu_0}{\mu}\right)\sqrt{Bo_{g^*}} \tag{6.4}$$

This equation suggests that we can try to convert the raw data of figure 6.2 to the dimensionless numbers Bo_{g^*} and S and fit the data according to the scaling law $S_c = \alpha Bo_{g^*}$,

where $\alpha = 2\left(1 + \frac{\mu_0}{\mu}\right)$ is taken as a free parameter. The results of this attempt are shown in the log-log graph of figure 6.3. As can be seen, the data are found to nicely collapse on parallel straight lines having a slope of 1/2 as expected. Moreover, the straight lines seem to fit rather well both the data relative to the saddle points (graphically enclosed in the white region) and the data relative to the maximum height points (enclosed in the dashed region). Another interesting observation that can be done is that the data corresponding to different surfaces are found to collapse on the same curves. Instead, there is a marked dependence on the ferrofluid concentration and thus on the magnetic interaction: as the concentration increases, the straight line moves upward. The inset graph shows that the coefficient α is linearly dependent on the ferrofluid saturation magnetization magnetization and so from the concentration. We have compared these values with those derived from $\alpha = 2\left(1 + \frac{\mu_0}{\mu}\right)$ using the measured ferrofluids susceptibilities. The numerical agreement is fair but, more important, the formula predicts a decrease of α with the ferrofluid magnetization which is the opposite of the trend of our data. This clearly suggests that the formula of the parameter α valid for a ferrofluid pool must be suitably corrected for a ferrofluid drop.

The last analysis we have performed is the connection between the drop size just before the breakup and the critical size defined in eq. 6.2, which can be written in terms of the magnetic capillary length [**?**]: $a^*(z) = \sqrt{\frac{\gamma}{\rho g^*(z)}}$ as $d_c = 2\pi a^*$. If there is no magnetic field, a^* reduces to the standard capillary length. The snapshots in figure 6.4 show the characteristic profiles assumed by ferrofluid drops of volume $\Omega = 10\mu L$ deposited on the four surfaces when the saddle point is observed. The green horizontal lines indicate the maximum lateral diameter D exhibited by the drops. Experimentally, it is obtained by taking the maximum value between the two diameters measured from the two orthogonal cameras just before the saddle point is observed. The graph in figure 6.4 displays D as a function of the critical length d_c deduced from the distance z_{saddle} for drops of different volume and concentration, deposited on the four surfaces. The data points refer to ferrofluid drops of different volumes (from 5 to 40 μL) and concentrations (from 4 to 7.5 mol/L) deposited on the four surfaces represented with different symbols. Within the intrinsic scatter of the measurements, there do not seem to be systematic variations attributable to volume, concentration, or substrate. The data lie on a straight line of equation $D = 1.25d_c - 0.3$. This result confirms that the drop starts to divide when its transversal diameter is somewhat larger than or close to the critical size d_c [37].

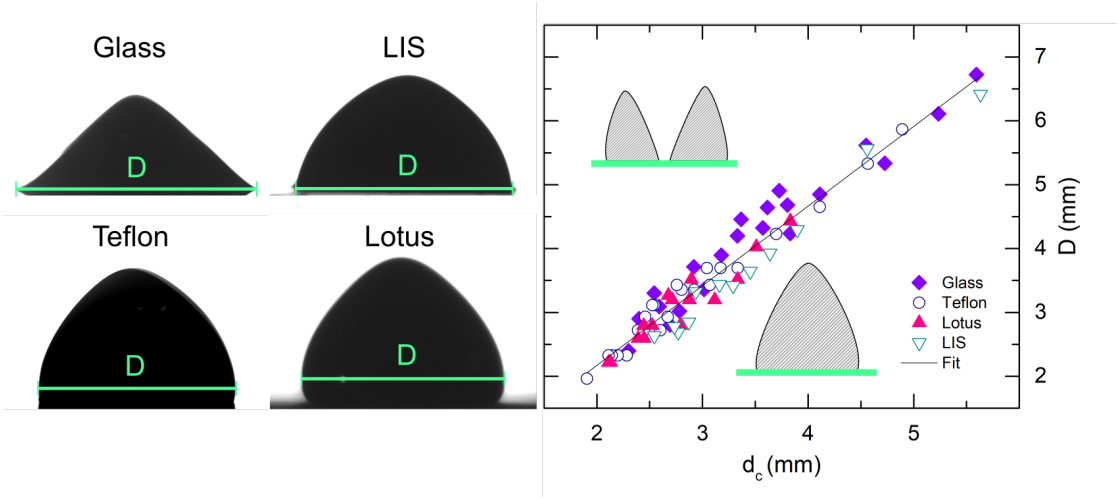

Figure 6.4 : (Left) Snapshots of the profiles assumed by ferrofluid drops of concentration 4 mol/L and volume $\Omega = 20\mu L$ deposited on the four surfaces Just before the reaching of the saddle point. The green horizontal lines indicate the maximum lateral diameter D. (Right) Maximum diameter D as a function of the critical length d_c deduced from the distance z_{saddle}. The data points refer to ferrofluid drops of different volumes (from 5 to 40 μL) and concentrations (from 4 to 7.5 mol/L) deposited on the four surfaces represented with different symbols. The linear fit separates the region of stability of one drop (bottom snapshot) from that of two daughter droplets (top snapshot).

§ 6.3. Conclusions

In this chapter, we have systematically investigated the phenomenon of the division of a ferrofluid drop in two droplets caused by the application of an external magnetic field. By moving the permanent magnet closer to the drop, we have identified two characteristic distances: z_{max}, corresponding to the drop reaching its maximum height, and z_{saddle}, corresponding to the formation of a saddle at the top of the drop peak identifying the beginning of the drop breakup. If we consider the variation of these two critical distances in function of the parameter changed we observe that the data exhibit a distinct dependence on the substrate: both z_{max} and z_{saddle} increase with the apparent contact angle. Instead, for a given substrate, there does not seem to be a dependence on the ferrofluid concentration. If instead we rescale these quantities in terms of the dimensionless bond number (Bo_{g^*}) and traction number (S_c), the data on different surfaces are found to nicely collapse on curves having the form $S_c = \alpha Bo_{g^*}^{1/2}$, where α is found to depend on the ferrofluid concentration. Finally we have measured the maximum diameter of the drops right before the division and found that it is linearly linked linked to a critical size, which depends on the magnetic attraction. It is our hope that this preliminary study paves the way to detailed magnetohydrodynamic investigations of this fascinating nonlinear phenomenon, which can provide physical grounds to our empirical observations.

Conclusions

In this thesis we have shown that ferrofluids droplets on functionalized surfaces provide an ideal playground for fundamental studies on drop statics and dynamics and can suggest useful strategies for passive and active control of drop motion. To demonstrate this, first we have presented some basics concepts about ferrofluids and microfluidics that clearly indicate that the characteristics of ferrofluids offer a wide range of options for microfluidic applications from the control of the shape of the interface to the control of the viscosity. After that we have presented three different case studies about ferrofluid droplets in open microfluidics.

In these research activities we have used the same ferrofluid, varying its concentration to tune the magnetic interaction. The ferrofluid used in this work is a stable aqueous suspension of maghemite ($\gamma - Fe_2O_3$) nanoparticles synthesized according to the Massart procedure.

We have reported results of a comprehensive study of the wetting properties of sessile drops of ferrofluid at various concentrations deposited on flat solid substrates and subjected to the action of permanent magnets of different sizes and strengths. Magnetic forces up to 100 times the gravitational one and strong magnetic gradients up to 1 T/cm are achieved. A rich phenomenology is observed, ranging from flattened drops caused by the magnetic attraction to drops elongated normally to the substrate because of the normal traction of the magnetic field. We find that the flattening effect can be described in terms of the effective Bond number $Bo_{g^*} = \rho g^* V^{2/3} \gamma^{-1}$, which compares the effective downward drop attraction with the capillary force, and that the drop vertical elongation can be expressed using the dimensionless Traction number $S = \mu_0 M^2 V^{1/3} \gamma^{-1}$, which compares the magnetic traction pressure with the capillary pressure.

We have then characterized the effects of a uniform and a heterogeneous magnetic field on the motion of ferrofluid drops on slippery surfaces (LIS). The application of a uniform magnetic field only slows down gravity-driven ferrofluid drops probably for the magnetoviscous effect. The presence of magnetic patterning instead significantly enriches the

drop dynamics. In particular, a linear modulation in the magnetic field of alternated stripes of high and low magnetic field causes a stick-slip motion whose contrast and phase can be easily tuned. We have also found that the phase shift between the moving frontal and rear contact points changes continuously with the drop velocity from 0 to 2π.

Finally we have systematically investigated the phenomenon of the division of a ferrofluid drop in two daughter droplets caused by the application of an external magnetic field. By approaching the magnet to the drop, we have identified two characteristic distances: z_{max}, corresponding to the drop reaching its maximum height, and z_{saddle}, corresponding to the formation of a saddle at the top of the drop peak identifying the beginning of the drop breakup. If we consider the variation of these two critical distances as a function of the parameter changed we observe that the data exhibit a distinct dependence on the substrate: both z_{max} and z_{saddle} increase with the apparent contact angle. Instead, for a given substrate, there does not seem to be a dependence on the ferrofluid concentration. If instead we rescale these quantities in terms of the dimensionless bond number (Bo_{g^*}) and traction number (S_c), the data on different surfaces are found to nicely collapse on curves having the form $S_c = \alpha\sqrt{Bo_{g^*}}$, where the value of α is found to be linked to the ferrofluid concentration. Finally we have measured the maximum diameter of the drops right before the division and found that it is linearly linked linked to a critical size, which depends on the magnetic attraction.

The results of these three cases of study prove that the use of ferrofluid in microfluidics can enlarge the possibilities of controlling the shape and the motion of droplets. Moreover the division phenomenon is a peculiar property of the ferrofluid drops that can hardly be achieved in other ways.

There is an ample variety of possible ways to extend this research. The first is to repeat the same experiments but using ferrofluid with different properties like ferrofluids made out of nanoplatelets instead of nanoparticles or using cobalt ferrite nanoparticles instead of maghemite nanoparticles for which we expect stronger changes in the viscosity. Another possibility is to study the effect of a uniform magnetic field applied to an oscillating droplet.

It is in our belief that a deep and complete understanding of the behavior of ferrofluid droplets interacting with magnetic field will certainly open the way to new and smart solution to control the droplets on open surfaces.

Acknowledgements

Bibliography

[1] P.-G. da Gennes, B.-W. Francoise, and D. Quere, *Capillarity and Wetting Phenomena: Drops, Bubbles, Pearls, Waves.* Springer, 2004.

[2] G. Mistura and M. Pierno, "Drop mobility on chemically heterogeneous and lubricant-impregnated surfaces", *Advances in Physics: X*, vol. 2, no. 3, pp. 591–607, 2017.

[3] D. Bonn, J. Eggers, J. Indekeu, and J. Meunier, "Wetting and spreading", *Reviews of Modern Physics*, 2009.

[4] R. Seemann, M. Brinkmann, T. Pfohl, and S. Herminghaus, "Droplet based microfluidics", *Reports on Progress in Physics*, 2012.

[5] D. Quéré, "Wetting and Roughness", *Annual Review of Materials Research*, 2008.

[6] F. T. Malik, R. M. Clement, D. T. Gethin, W. Krawszik, and A. R. Parker, "Nature's moisture harvesters: A comparative review", *Bioinspiration and Biomimetics*, 2014.

[7] K. C. Park, P. Kim, A. Grinthal, N. He, D. Fox, J. C. Weaver, and J. Aizenberg, "Condensation on slippery asymmetric bumps", *Nature*, 2016.

[8] A. Roth-Nebelsick, M. Ebner, T. Miranda, V. Gottschalk, D. Voigt, S. Gorb, T. Stegmaier, J. Sarsour, M. Linke, and W. Konrad, "Leaf surface structures enable the endemic Namib desert grass Stipagrostis sabulicola to irrigate itself with fog water", *Journal of the Royal Society Interface*, 2012.

[9] S. Nishimoto and B. Bhushan, "Bioinspired self-cleaning surfaces with superhydrophobicity, superoleophobicity, and superhydrophilicity", *RSC Advances*, 2013.

[10] P. Roach, N. J. Shirtcliffe, and M. I. Newton, "Progess in superhydrophobic surface development", *Soft Matter*, 2008.

[11] L. Bocquet and E. Lauga, "A smooth future?" *Nature Materials*, 2011.

[12] A. Lafuma and D. Quéré, "Slippery pre-suffused surfaces", *Epl*, vol. 96, no. 5, 2011.

[13] T. S. Wong, S. H. Kang, S. K. Tang, E. J. Smythe, B. D. Hatton, A. Grinthal, and J. Aizenberg, "Bioinspired self-repairing slippery surfaces with pressure-stable omniphobicity", *Nature*, vol. 477, no. 7365, pp. 443–447, 2011.

[14] J. D. Smith, R. Dhiman, S. Anand, E. Reza-Garduno, R. E. Cohen, G. H. McKinley, and K. K. Varanasi, "Droplet mobility on lubricant-impregnated surfaces", *Soft Matter*, vol. 9, no. 6, pp. 1772–1780, 2013.

[15] C. Semprebon, S. Varagnolo, D. Filippi, L. Perlini, M. Pierno, M. Brinkmann, and G. Mistura, "Deviation of sliding drops at a chemical step", *Soft Matter*, 2016.

[16] M. Sbragaglia, L. Biferale, G. Amati, S. Varagnolo, D. Ferraro, G. Mistura, and M. Pierno, "Sliding drops across alternating hydrophobic and hydrophilic stripes", *Physical Review E - Statistical, Nonlinear, and Soft Matter Physics*, vol. 89, no. 1, pp. 1–12, 2014.

[17] S. Varagnolo, V. Schiocchet, D. Ferraro, M. Pierno, G. Mistura, M. Sbragaglia, A. Gupta, and G. Amati, "Tuning drop motion by chemical patterning of surfaces", *Langmuir*, vol. 30, no. 9, pp. 2401–2409, 2014.

[18] M. K. Chaudhury and G. M. Whitesides, "How to make water run uphill", *Science*, vol. 256, no. 5063, pp. 1539–1541, 1992.

[19] Y. Chen, B. He, J. Lee, and N. A. Patankar, "Anisotropy in the wetting of rough surfaces", *Journal of Colloid and Interface Science*, vol. 281, no. 2, pp. 458–464, 2005.

[20] C. Semprebon, G. Mistura, E. Orlandini, G. Bissacco, A. Segato, and J. M. Yeomans, "Anisotropy of water droplets on single rectangular posts", *Langmuir*, vol. 25, no. 10, pp. 5619–5625, 2009.

[21] L. Y. Yeo and J. R. Friend, "Surface Acoustic Wave Microfluidics", *Annual Review of Fluid Mechanics*, vol. 46, no. 1, pp. 379–406, 2014.

[22] D. Quéré, "Leidenfrost Dynamics", *Annual Review of Fluid Mechanics*, 2013.

[23] L. Dong, A. Chaudhury, and M. K. Chaudhury, "Lateral vibration of a water drop and its motion on a vibrating surface", *European Physical Journal E*, 2006.

[24] P. Brunet, J. Eggers, and R. D. Deegan, "Vibration-induced climbing of drops", *Physical Review Letters*, 2007.

[25] X. Noblin, R. Kofman, and F. Celestini, "Ratchetlike motion of a shaken drop", *Physical Review Letters*, 2009.

[26] P. Sartori, D. Quagliati, S. Varagnolo, M. Pierno, G. Mistura, F. Magaletti, and C. M. Casciola, "Drop motion induced by vertical vibrations", *New Journal of Physics*, vol. 17, no. 11, 2015.

[27] F. Mugele and J. C. Baret, "Electrowetting: From basics to applications", *Journal of Physics Condensed Matter*, 2005.

[28] K. Choi, A. H. Ng, R. Fobel, and A. R. Wheeler, "Digital Microfluidics", *Annual Review of Analytical Chemistry*, vol. 5, no. 1, pp. 413–440, 2012.

[29] E. Bormashenko, R. Pogreb, Y. Bormashenko, A. Musin, and T. Stein, "New investigations on ferrofluidics: Ferrofluidic marbles and magnetic-field-driven drops on superhydrophobic surfaces", *Langmuir*, vol. 24, no. 21, pp. 12 119–12 122, 2008.

[30] H. Asakura, A. Nakajima, M. Sakai, S. Suzuki, Y. Kameshima, and K. Okada, "Deformation and motion by gravity and magnetic field of a droplet of water-based magnetic fluid on a hydrophobic surface", *Applied Surface Science*, vol. 253, no. 6, pp. 3098–3102, 2007.

[31] M. Latikka, M. Backholm, J. V. Timonen, and R. H. Ras, "Wetting of ferrofluids: Phenomena and control", *Current Opinion in Colloid and Interface Science*, 2018.

[32] K. Butter, P. Bomans, P. Frederik, G. Vroege, and A. Philipse, "Direct observation of dipolar chains in iron ferrofluids by cryogenic electron microscopy", *Nature Materials*, vol. 2, no. 2, pp. 88–91, 2003.

[33] J. C. Bacri, R. Perzynski, and D. Salin, "Magnetic Liquids", *Endeavour*, 1988.

[34] R. E. Rosensweig, *Ferrohydrodynamics*. Cambridge University Press, 1985.

[35] N. A. Clark, "Soft-matter physics: Ferromagnetic ferrofluids", *Nature*, vol. 504, no. 7479, pp. 229–230, 2013.

[36] M. D. Cowley and R. E. Rosensweig, "The interfacial stability of a ferromagnetic fluid", *Journal of Fluid Mechanics*, vol. 30, no. 04, p. 671, 1967.

[37] J. V. Timonen, M. Latikka, L. Leibler, R. H. Ras, and O. Ikkala, "Switchable static and dynamic self-assembly of magnetic droplets on superhydrophobic surfaces", *Science*, 2013.

[38] S. Odenbach, *Magnetoviscous effect in ferrofluids*. Springer, 2002.

[39] ——, "Ferrofluids - Magnetically controlled suspensions", *Colloids and Surfaces A: Physicochemical and Engineering Aspects*, vol. 217, no. 1-3, pp. 171–178, 2003.

[40] Y. Zhang and N. T. Nguyen, "Magnetic digital microfluidics - a review", 2017.

[41] G. Katsikis, J. S. Cybulski, and M. Prakash, "Synchronous universal droplet logic and control", *Nature Physics*, vol. 11, no. 7, pp. 588–596, 2015.

[42] N. T. Nguyen, "Micro-magnetofluidics: Interactions between magnetism and fluid flow on the microscale", *Microfluidics and Nanofluidics*, 2012.

[43] B. Teste, N. Jamond, D. Ferraro, J. L. Viovy, and L. Malaquin, "Selective handling of droplets in a microfluidic device using magnetic rails", *Microfluidics and Nanofluidics*, 2015.

[44] D. Ferraro, J. Champ, B. Teste, M. Serra, L. Malaquin, J. L. Viovy, P. De Cremoux, and S. Descroix, "Microfluidic platform combining droplets and magnetic tweezers: Application to HER2 expression in cancer diagnosis", *Scientific Reports*, 2016.

[45] D. Ferraro, Y. Lin, B. Teste, D. Talbot, L. Malaquin, S. Descroix, and A. Abou-Hassan, "Continuous chemical operations and modifications on magnetic γ-Fe2O3nanoparticles confined in nanoliter droplets for the assembly of fluorescent and magnetic SiO2@γ-Fe2O3", *Chemical Communications*, 2015.

[46] A.-E. Saliba, L. Saias, E. Psychari, N. Minc, D. Simon, F.-C. Bidard, C. Mathiot, J.-Y. Pierga, V. Fraisier, J. Salamero, V. Saada, F. Farace, P. Vielh, L. Malaquin, and J.-L. Viovy, "Microfluidic sorting and multimodal typing of cancer cells in self-assembled magnetic arrays", *Proceedings of the National Academy of Sciences*, 2010.

[47] M. Hejazian, W. Li, and N. T. Nguyen, "Lab on a chip for continuous-flow magnetic cell separation", *Lab on a Chip*, 2015.

[48] Y. Wu, T. Fu, Y. Ma, and H. Z. Li, "Ferrofluid droplet formation and breakup dynamics in a microfluidic flow-focusing device", *Soft Matter*, 2013.

[49] N. T. Nguyen, G. Zhu, Y. C. Chua, V. N. Phan, and S. H. Tan, "Magnetowetting and sliding motion of a sessile ferrofluid droplet in the presence of a permanent magnet", *Langmuir*, vol. 26, no. 15, pp. 12 553–12 559, 2010.

[50] N.-T. Nguyen, "Deformation of Ferrofluid Marbles in the Presence of a Permanent Magnet", *Langmuir*, 2013.

[51] C. Rigoni, "Studio delle proprietà di wetting di ferrofluidi", 2015.

[52] C. Rigoni, M. Pierno, G. Mistura, D. Talbot, R. Massart, J. C. Bacri, and A. Abou-Hassan, "Static Magnetowetting of Ferrofluid Drops", *Langmuir*, vol. 32, no. 30, pp. 7639–7646, 2016.

[53] U. Banerjee and A. K. Sen, "Shape evolution and splitting of ferrofluid droplets on a hydrophobic surface in the presence of a magnetic field", *Soft Matter*, 2018.

[54] Z. G. Guo, F. Zhou, J. C. Hao, Y. M. Liang, W. M. Liu, and W. T. Huck, ""Stick and slide" ferrofluidic droplets on superhydrophobic surfaces", *Applied Physics Letters*, vol. 89, no. 8, pp. 8–11, 2006.

[55] P. Tabeling, *Introduction to microfluidics*. Oxford university press, 2005.

[56] G. F. Christopher, J. Bergstein, N. B. End, M. Poon, C. Nguyen, and S. L. Anna, "Coalescence and splitting of confined droplets at microfluidic junctions", *Lab on a Chip*, vol. 9, no. 8, p. 1102, 2009.

[57] a. K. Chesters, "The modelling of coalescence process in fluid-liquid dispersions: A Review of Current Understanding", *Chemical Engineering Research and Design*, vol. 69, no. 4, pp. 259–270, 1991.

[58] L. D. Landau and E. M. Lifshitz, *Fluid Mechanics*, 1987, vol. 6, no. 1.

[59] V. Castelletto, I. Cantat, D. Sarker, R. Bausch, D. Bonn, and J. Meunier, "Stability of soap films: Hysteresis and nucleation of black films", *Physical Review Letters*, vol. 90, no. 4, pp. 10–13, 2003.

[60] W. D. Ristenpart, P. M. McCalla, R. V. Roy, and H. A. Stone, "Coalescence of spreading droplets on a wettable substrate", *Physical Review Letters*, vol. 97, no. 6, pp. 1–4, 2006.

[61] A. B. D. Cassie and S. Baxter, "Wettability of porous surfaces", *Transactions of the Faraday Society*, vol. 40, p. 546, 1944.

[62] R. N. Wenzel, "Resistance of solid surfaces to wetting by water", *Industrial and Engineering Chemistry*, vol. 28, no. 8, pp. 988–994, 1936.

[63] S. Varagnolo, "Study and control of drop motion on inclined surfaces", Ph.D. dissertation, University of Padua, 2016.

[64] D. Quéré, "Surface chemistry: Fakir droplets", *Nature Materials*, vol. 1, no. 1, pp. 14–15, 2002.

[65] W. Barthlott and C. Neinhuis, "Purity of the sacred lotus, or escape from contamination in biological surfaces", *Planta*, vol. 202, no. 1, pp. 1–8, 1997.

[66] A. Lafuma and D. Quéré, "Superhydrophobic states", *Nature Materials*, vol. 2, no. 7, pp. 457–460, 2003.

[67] H. F. Bohn and W. Federle, "Insect aquaplaning: Nepenthes pitcher plants capture prey with the peristome, a fully wettable water-lubricated anisotropic surface", *Proceedings of the National Academy of Sciences*, vol. 101, no. 39, pp. 14 138–14 143, 2004.

[68] U. Bauer and W. Federle, "The insect-trapping rim of Nepenthes pitchers: surface structure and function." *Plant signaling & behavior*, vol. 4, no. 11, pp. 1019–1023, 2009.

[69] N. Bjelobrk, H. L. Girard, S. B. Subramanyam, H. M. Kwon, D. Quéré, and K. K. Varanasi, "Thermocapillary motion on lubricant-impregnated surfaces", *Physical Review Fluids*, vol. 1, no. 6, pp. 1–7, 2016.

[70] T. V. Charpentier, A. Neville, S. Baudin, M. J. Smith, M. Euvrard, A. Bell, C. Wang, and R. Barker, "Liquid infused porous surfaces for mineral fouling mitigation", *Journal of Colloid and Interface Science*, vol. 444, pp. 81–86, 2015.

[71] J. S. Wexler, I. Jacobi, and H. A. Stone, "Shear-driven failure of liquid-infused surfaces", *Physical Review Letters*, vol. 114, no. 16, pp. 1–5, 2015.

[72] A. Eifert, D. Paulssen, S. N. Varanakkottu, T. Baier, and S. Hardt, "Simple Fabrication of Robust Water-Repellent Surfaces with Low Contact-Angle Hysteresis Based on Impregnation", *Advanced Materials Interfaces*, vol. 1, no. 3, 2014.

[73] S. Ling, Y. Luo, L. Luan, Z. Wang, and T. Wu, "Inkjet printing of patterned ultra-slippery surfaces for planar droplet manipulation", *Sensors and Actuators, B: Chemical*, vol. 235, pp. 732–738, 2016.

[74] S. Anand, A. T. Paxson, R. Dhiman, J. D. Smith, and K. K. Varanasi, "Enhanced condensation on lubricant-impregnated nanotextured surfaces", *ACS Nano*, vol. 6, no. 11, pp. 10 122–10 129, 2012.

[75] M. J. Kreder, J. Alvarenga, P. Kim, and J. Aizenberg, "Design of anti-icing surfaces: Smooth, textured or slippery?" *Nature Reviews Materials*, vol. 1, no. 1, 2016.

[76] H. A. Stone, "Ice-phobic surfaces that are wet", *ACS Nano*, vol. 6, no. 8, pp. 6536–6540, 2012.

[77] A. K. Epstein, T.-S. Wong, R. A. Belisle, E. M. Boggs, and J. Aizenberg, "Liquid-infused structured surfaces with exceptional anti-biofouling performance", *Proceedings of the National Academy of Sciences*, vol. 109, no. 33, pp. 13 182–13 187, 2012.

[78] S. Amini, S. Kolle, L. Petrone, O. Ahanotu, S. Sunny, C. N. Sutanto, S. Hoon, L. Cohen, J. C. Weaver, J. Aizenberg, N. Vogel, and A. Miserez, "Preventing mussel adhesion using lubricant-infused materials", *Science*, vol. 357, no. 6352, pp. 668–673, 2017.

[79] A. I. ElSherbini and A. M. Jacobi, "Liquid drops on vertical and inclined surfaces: I. An experimental study of drop geometry", *Journal of Colloid and Interface Science*, vol. 273, no. 2, pp. 556–565, 2004.

[80] C. G. L. Furmidge, "Studies at phase interfaces. i. the sliding of liquid drops on solid surfaces and a theory for spray retention." *Journal of Colloid Science*, vol. 4, pp. 309 – 324, 1962.

[81] C. W. Extrand and Y. Kumagai, "Liquid Drops on an Inclined plane: The Relation between contact Angles, Drops Shape, and Retentive Force", *Journal of Colloid And Interface Science*, vol. 170, pp. 515–521, 1995.

[82] T. Podgorski, J. M. Flesselles, and L. Limat, "Corners, cusps, and pearls in running drops", *Physical Review Letters*, vol. 87, no. 3, pp. 361 021–361 024, 2001.

[83] N. Le Grand, A. Daerr, and L. Limat, "Shape and motion of drops sliding down an inclined plane", *Journal of Fluid Mechanics*, vol. 541, no. -1, p. 293, 2005.

[84] S. Ravi Annapragada, J. Y. Murthy, and S. V. Garimella, "Prediction of droplet dynamics on an incline", *International Journal of Heat and Mass Transfer*, vol. 55, no. 5-6, pp. 1466–1474, 2012.

[85] A. K. Das and P. K. Das, "Simulation of drop movement over an inclined surface using smoothed particle hydrodynamics", *Langmuir*, vol. 25, no. 19, pp. 11 459–11 466, 2009.

[86] S. P. Thampi, R. Adhikari, and R. Govindarajan, "Do liquid drops roll or slide on inclined surfaces?" *Langmuir*, vol. 29, no. 10, pp. 3339–3346, 2013.

[87] M. Sakai, J. H. Song, N. Yoshida, S. Suzuki, Y. Kameshima, and A. Nakajima, "Direct observation of internal fluidity in a water droplet during sliding on hydrophobic surfaces", *Langmuir*, vol. 22, no. 11, pp. 4906–4909, 2006.

[88] L. Gao and T. J. McCarthy, "Contact angle hysteresis explained", *Langmuir*, vol. 22, no. 14, pp. 6234–6237, 2006.

[89] A. Keiser, L. Keiser, C. Clanet, and D. Quéré, "Drop friction on liquid-infused materials", *Soft Matter*, vol. 13, no. 39, 2017.

[90] T. Hyeon, "Chemical synthesis of magnetic nanoparticles", *Chemical Communications*, no. 8, pp. 927–934, 2003.

[91] A. Mertelj, D. Lisjak, M. Drofenik, and M. Čopič, "Ferromagnetism in suspensions of magnetic platelets in liquid crystal", *Nature*, vol. 504, no. 7479, pp. 237–241, 2013.

[92] M. Latikka, M. Backholm, J. V. I. Timonen, and R. H. A. Ras, "Us Cr", *Current Opinion in Colloid & Interface Science*, vol. 36, no. January, p. #pagerange#, 2018.

[93] N. Pamme, "Magnetism and microfluidics", *Lab Chip*, vol. 6, no. 1, pp. 24–38, 2006.

[94] H. C. Hamaker, "The London-van der Waals attraction between spherical particles", *Physica*, vol. 4, no. 10, pp. 1058–1072, 1937.

[95] C. P. Bean and J. D. Livingston, "Superparamagnetism", *Journal of Applied Physics*, vol. 30, no. 4, pp. S120–S129, 1959.

[96] B. D. Cullity and C. D. Graham, *Introduction to magnetic materials*. John Wiley & Sons., 2011.

[97] D. Jiles, *Introduction to Magnetism and Magnetic Materials*, 1991, vol. 1.

[98] R. M. Bozorth, *Ferromagnetism*, 1951.

[99] O. E. Séro-Guillaume, D. Zouaoui, D. Bernardin, and J. P. Brancher, "The shape of a magnetic liquid drop", *Journal of Fluid Mechanics*, 1992.

[100] V. I. Arkhipenko, Y. D. Barkov, and V. G. Bashtovoi, "Shape of a drop of magnetized fluid in a homogeneous magnetic field", *Magnetohydrodynamics*, vol. 14, no. 3, pp. 373–375, 1979.

[101] R. E. Rosensweig, M. Zahn, and R. Shumovich, "Labyrinthine instability in magnetic and dielectric fluids", *Journal of Magnetism and Magnetic Materials*, vol. 39, no. 1-2, pp. 127–132, 1983.

[102] R. E. Zelazo and J. R. Melcher, "Dynamics and stability of ferrofluids: surface interactions", *Journal of Fluid Mechanics*, vol. 39, no. 01, p. 1, 1969.

[103] J. P. McTague, "Magnetoviscosity of Magnetic Colloids", *The Journal of Chemical Physics*, vol. 51, no. 1, pp. 133–136, 1969.

[104] A. G. Olabi and A. Grunwald, "Design and application of magneto-rheological fluid", *Materials and Design*, vol. 28, no. 10, pp. 2658–2664, 2007.

[105] B. F. Spencer Jr, S. J. Dyke, M. K. Sain, and J. D. Carlson, "Phenomenological model for magnetorheological dampers", *Engineering Mechanics*, vol. 123, no. 3, pp. 230–238, 1997.

[106] L. M. Pop and S. Odenbach, "Investigation of the microscopic reason for the magnetoviscous effect in ferrofluids studied by small angle neutron scattering", *Journal of Physics: Condensed Matter*, vol. 18, no. 38, pp. S2785–S2802, 2006.

[107] E. Ghasemi, A. Mirhabibi, and M. Edrissi, "Magnetoviscous effect in a maghemite ferrofluid." *Journal of Nanoscience and Nanotechnology*, vol. 11, no. 6, pp. 5285–5291, 2011.

[108] R. Massart, "Preparation of aqueous magnetic liquids in alkaline and acidic media", *IEEE Transactions on Magnetics*, vol. 17, no. 2, pp. 1247–1248, 1981.

[109] S. Lefebure, E. Dubois, V. Cabuil, S. Neveu, and R. Massart, "Monodisperse magnetic nanoparticles: Preparation and dispersion in water and oils", *Journal of Materials Research*, vol. 13, no. 10, pp. 2975–2981, 1998.

[110] S. Foner, "Versatile and sensitive vibrating-sample magnetometer", *Review of Scientific Instruments*, vol. 30, no. 7, pp. 548–557, 1959.

[111] D. B. Williams and C. B. Carter, "The Transmission Electron Microscope", in *Transmission Electron Microscopy*, 1996, pp. 3–17.

[112] S. Khaleduzzaman, I. Mahbubul, I. Shahrul, and R. Saidur, "Effect of particle concentration, temperature and surfactant on surface tension of nanofluids", *International Communications in Heat and Mass Transfer*, vol. 49, pp. 110–114, 2013.

[113] J. M. Camacho and V. Sosa, "Alternative method to calculate the magnetic field of permanent magnets with azimuthal symmetry", *Revista Mexicana de Fisica E*, vol. 59, no. 1, pp. 8–17, 2013.

[114] M. Carnieri, "Moto di gocce di ferrofluido su piano inclinato soggette a un campo magnetico esterno", 2018.

[115] S. Afkhami, A. Tyler, Y. Renardy, M. Renardy, T. St. Pierre, R. Woodward, and J. Riffle, "Deformation of a hydrophobic ferrofluid droplet suspended in a viscous medium under uniform magnetic fields", *Journal of Fluid Mechanics*, vol. 663, pp. 358–384, 2010.

[116] K. Piroird, C. Clanet, and D. Quéré, "Magnetic control of Leidenfrost drops", *Physical Review E - Statistical, Nonlinear, and Soft Matter Physics*, vol. 85, no. 5, pp. 10–13, 2012.

[117] C. Rigoni, D. Ferraro, M. Carlassara, D. Filippi, S. Varagnolo, M. Pierno, D. Talbot, A. Abou-Hassan, and G. Mistura, "Dynamics of Ferrofluid Drops on Magnetically Patterned Surfaces", *Langmuir*, vol. 34, no. 30, pp. 8917–8922, 2018.

[118] M. Morita, T. Koga, H. Otsuka, and A. Takahara, "Macroscopic-wetting anisotropy on the line-patterned surface of fluoroalkylsilane monolayers", *Langmuir*, 2005.

[119] S. Suzuki, A. Nakajima, K. Tanaka, M. Sakai, A. Hashimoto, N. Yoshida, Y. Kameshima, and K. Okada, "Sliding behavior of water droplets on line-patterned hydrophobic surfaces", *Applied Surface Science*, 2008.

[120] S. Varagnolo, D. Ferraro, P. Fantinel, M. Pierno, G. Mistura, G. Amati, L. Biferale, and M. Sbragaglia, "Stick-slip sliding of water drops on chemically heterogeneous surfaces", *Physical Review Letters*, 2013.

[121] Q. Li, P. Zhou, and H. J. Yan, "Pinning-Depinning Mechanism of the Contact Line during Evaporation on Chemically Patterned Surfaces: A Lattice Boltzmann Study", *Langmuir*, 2016.

[122] J. Zhao, S. Chen, and Y. Liu, "Droplets motion on chemically/topographically heterogeneous surfaces", *Molecular Simulation*, 2016.

[123] M. Liu and X. P. Chen, "Numerical study on the stick-slip motion of contact line moving on heterogeneous surfaces", *Physics of Fluids*, 2017.

[124] J. Zhao, S. Chen, and Y. Liu, "Dynamical behaviors of droplet impingement and spreading on chemically heterogeneous surfaces", *Applied Surface Science*, 2017.

[125] F. Schellenberger, J. Xie, N. Encinas, A. Hardy, M. Klapper, P. Papadopoulos, H. J. Butt, and D. Vollmer, "Direct observation of drops on slippery lubricant-infused surfaces", *Soft Matter*, 2015.

[126] C. Rigoni, S. Bertoldo, M. Pierno, D. Talbot, A. Abou-Hassan, and G. Mistura, "Division of Ferrofluid Drops Induced by a Magnetic Field", *Langmuir*, 2018.

[127] I. Seric, S. Afkhami, and L. Kondic, "Interfacial instability of thin ferrofluid films under a magnetic field", *Journal of Fluid Mechanics*, 2014.